

Modeling and simulation of thermo-electro hydrodynamics

Von der Fakultät für Maschinenbau, Elektro- und Energiesysteme der
Brandenburgischen Technischen Universität Cottbus–Senftenberg zur
Erlangung des akademischen Grades eines
Dr.-Ing. habil.

genehmigte Habilitationsschrift

vorgelegt von
Dr. rer. nat. Mag.
Florian Zaussinger

geboren am 24. März 1978 in Wien, Österreich

Vorsitzender: Prof. Dr.-Ing. Heiko Schmidt
Gutachter: Prof. Dr. Ing Christoph Egbers
Gutachter: Univ. Prof. Dipl.-Phys. Dr. rer. nat. habil. Hendrik Kuhlmann
Gutachter: Prof. Dr. Rainer Hollerbach
Weiteres Mitglied: Prof. Dr.rer.nat. Andreas Schröder

Eröffnung des Habilitationsverfahrens: 26. August 2020
Tag des Habilitationskolloquiums: 12. März 2021
Zuerkennung der Lehrbefähigung: 19. Mai 2021

Abstract

The GeoFlow (Geophysical Flow) experiment on the International Space Station (ISS) and the AtmoFlow (Atmospherical Flow) experiment are designed to study convective processes under microgravity conditions in the spherical gap geometry. By applying a high voltage field between two concentric spherical shells and utilizing a dielectric working fluid it is possible to maintain an artificial radial force field that is comparable to a planetary gravitational field. This makes it possible to study convection such as known from the Earth's outer core, the Earth's mantle, or planetary atmospheres. The radial force field is based on the dielectrophoretic effect and is described by thermo-electro hydrodynamics (TEHD). This habilitation thesis presents a comprehensive view on modeling TEHD and the numerical simulation of the governing equations with a focus on GeoFlow and AtmoFlow.

The GeoFlow experiment investigated thermal convection with and without dielectric (internal) heating under long-time micro-gravity conditions on the ISS. This unique experimental setup consisted of a bottom heated and top cooled spherical gap, filled with the silicon oil M5 or 1-Nonanol. Rotation, varying voltage, and temperature differences across the gap could be applied, to spread the experimental parameter space. The main focus of GeoFlow was the investigation of flow properties such as the convective onset, the transition from laminar to turbulent flows, and the influence of rotation on convection. Experimental outcomes were compared with theoretical and numerical results via advanced post-processing techniques. This includes pattern recognition algorithms and statistical evaluation of the numerical simulations. The TEHD model was validated on the onset of convection through linear stability analysis, on properties of columnar cells and global convective structures such as regular laminar flows. It is shown that TEHD based convection is comparable with Rayleigh-Benard convection and that it can be described by the quasi-normal approximation. For rotating cases and low super-criticalities the Proudman-Taylor theorem dominated the fluid flow which resulted in global columnar cells. For strong internal heating, the mean temperature had its maximum in the middle of the gap. The existence of columnar cells was not ensured anymore due to a change of sign in the electric gravity. This also influenced the entire fluid flow. Needling down-welling plumes and broad upwelling-regions were present. In summary, the presented TEHD model is able to explain certain aspects of convective flows observed in GeoFlow. It is the first validation for such a model at all stages.

The AtmoFlow experiment is based on GeoFlow but is designed to investigate global cells and planetary waves which are known from planetary atmospheres. Its unique feature are the atmospheric-like boundary conditions. Understanding the interaction between atmospheric circulation and a planet's climate, be it Earth, Mars, Jupiter, or a distant exoplanet, contributes to various fields of research such as astrophysics, geophysics, fluid physics, and climatology. Varying rotational rates and temperature boundary conditions represent different types of planets. This is a very basic approach, but various open questions regarding local pattern formation or global planetary cells can be investigated with that setup. AtmoFlow is currently under construction and is planned for operation on the ISS in 2024. In the following the main idea, the design, the experimental setup, the measurement techniques, and numerical simulations of AtmoFlow are presented.

This habilitation thesis is cumulative. It is split into a summary and six representative peer-reviewed papers that are attached at the end of this manuscript.

Erklärung

Ich erkläre hiermit an Eides statt, dass ich die vorliegende Arbeit selbständig verfasst und keine anderen als die angegebenen Quellen und Hilfsmittel benutzt habe. Alle Ergebnisse der vorliegenden Habilitationsschrift, insbesondere die Texte und Abbildungen der Zusammenfassung, wurden in folgenden wissenschaftlichen Abhandlungen publiziert:

F. Zaussinger, A. Krebs, V. Travnikov, and C. Egbers. Recognition and tracking of convective flow patterns using Wollaston shearing interferometry. Advances in Space Research, 60(6):1327 – 1344, 2017. ISSN 0273-1177. doi: <https://doi.org/10.1016/j.asr.2017.06.028>. URL <http://www.sciencedirect.com/science/article/pii/S0273117717304544>

V. Travnikov, F. Zaussinger, P. Beltrame, and C. Egbers. Influence of the temperature-dependent viscosity on convective flow in the radial force field. Phys. Rev. E, 96:023108, Aug 2017. doi: 10.1103/PhysRevE.96.023108. URL <https://link.aps.org/doi/10.1103/PhysRevE.96.023108>

F. Zaussinger, P. Haun, M. Neben, T. Seelig, V. Travnikov, C. Egbers, H. Yoshikawa, and I. Mutabazi. Dielectrically driven convection in spherical gap geometry. Phys. Rev. Fluids, 3:093501, Sep 2018. doi: 10.1103/PhysRevFluids.3.093501. URL <https://link.aps.org/doi/10.1103/PhysRevFluids.3.093501>

F. Zaussinger, P. Canfield, A. Froitzheim, V. Travnikov, P. Haun, M. Meier, A. Meyer, P. Heintzmann, T. Driebe, and C. Egbers. AtmoFlow - Investigation of atmospheric-like fluid flows under microgravity conditions. Microgravity Science and Technology, Jul 2019. doi: 10.1007/s12217-019-09717-7. URL <https://doi.org/10.1007/s12217-019-09717-7>

V. Travnikov, F. Zaussinger, P. Haun, and C. Egbers. Influence of dielectrical heating on convective flow in a radial force field. Phys. Rev. E, 101:053106, May 2020. doi: 10.1103/PhysRevE.101.053106. URL <https://link.aps.org/doi/10.1103/PhysRevE.101.053106>

F. Zaussinger, P. Haun, P. Szabo, V. Travnikov, M. Al Kawwas, and C. Egbers. Rotating spherical gap convection in the GeoFlow International Space Station (ISS) experiment. Phys. Rev. Fluids, 5:063502, Jun 2020. doi: 10.1103/PhysRevFluids.5.063502. URL <https://link.aps.org/doi/10.1103/PhysRevFluids.5.063502>

Originalunterschrift Florian Zaussinger

Mahdel, 20. Mai 2021

Unterschrift

Contents

1	Introduction	1
1.1	EHD in the plane and cylindric geometry	1
1.2	Convection and EHD in the spherical gap	2
1.3	The GeoFlow experiment	3
1.4	Research objectives	5
2	Model formulation	7
2.1	Governing equations	7
3	Numerical methods and post-processing	12
3.1	Interferometry and flow visualization	12
3.2	Artificial interferograms	14
3.3	Recognition	16
3.4	Tracking	19
3.5	Identification of reference points	19
3.6	Numerical simulations	22
3.7	Statistical evaluation	24
4	Non-rotating convection	27
4.1	Onset of convection	27
4.2	Thermal profile in the convective case	30
4.3	The velocity field	30
5	Rotating convection	33
5.1	Classification	33
5.2	Onset of convection and base flow	33
5.3	Weakly nonlinear regime	35
5.4	Transitional regime for $\lambda \leq 1$	36
5.4.1	Thermal profile	36
5.4.2	Stability and Brunt-Väisälä frequency	37
5.5	Transitional regime for $\lambda > 1$	37
5.5.1	Thermal profile	38
5.5.2	Stability and N^2	38
6	Influence of viscosity contrast	42
6.1	Equations	42
6.2	Comparison of numerical and experimental results	42
6.3	Non-uniqueness in the GeoFlow experiment	43
7	AtmoFlow	46
7.1	Introduction	46
7.2	Objectives and scientific program	46
7.3	Geometry and thermal boundary conditions	47
7.4	Numerical results	48
8	Concluding remarks	53
9	Publications as full-text	65

1 Introduction

Applying an electric field to a dielectric fluid is a common method to manipulate fluids without using moving parts, [11, 69, 38]. This reduces the probability of failures and therefore maintenance work. This scientific field is called *electro-hydrodynamics (EHD)* and has been investigated intensely in the last five decades, [90, 44, 84, 85]. Many industrial applications benefit from EHD methods. EHD technology can be precisely controlled, even on micro and nano scales. For example, micro-dripping is used on nano-scales [32] and in commercial applications in many inkjet devices [67, 63]. Surface coating with electro-sprays is used, e.g., for printing thin film transistors, [47]. Natural coating of surfaces, e.g., by rain, plays an important role in industrial power transmission. Here, EHD is used to predict the damage caused by the interaction of fluids with electric fields on cables or power transformers, [83]. Thrusters [70], pumps [2], micro-mixing devices [20] and the separation of particles [33] on micro- and nano scales are direct applications from EHD research. Many of these applications are implemented in lab-on-a-chip devices.

All applications mentioned so far are based on the *dielectrophoretic force (DEP)* $\mathbf{F}_{\text{DEP}} = -\frac{1}{2}\mathbf{E}^2\nabla\epsilon$, which is utilized as directional force field. Here, ϵ is the electric permittivity and \mathbf{E} the electric field. This force results from a polarization of the fluid in the presence of a high frequency AC current. For confined, incompressible fluid layers without free charges, the DEP force dominates over all other induced electric forces. Hence, it can be used as a driving force to separate, e.g., particles or as a buoyancy-like force to mimic gravity. The force and direction of the DEP force depend on the electric field and the gradient of the electric permittivity, respectively. However, the electric permittivity needs to depend on, e.g., space, temperature or density to ensure a non-vanishing DEP force gradient. The thermal dependency of the permittivity defines the scientific field of thermo-electro hydrodynamics (TEHD) which is the focus of this work. In summary, the DEP force can be utilized as an electro-hydrodynamic buoyancy force whenever a fluid layer is confined in an internally or externally thermalized capacitor, [74]. In particular, the dielectrophoretic force can be used to enhance heat transfer in fluids [44, 1, 51] simply by increasing the voltage. EHD provides a reliable technology to reduce the weight and volume of thermal systems, [62]. EHD research is therefore of great importance for the aviation and especially, the space industry, where heat exchangers, heat pipes or mixing reactors are used, [39]. Applications include the thermal control system on the International Space Station (ISS), future permanent space stations on the Moon and Mars [81, 68] and all fluid-mechanical laboratory experiments under micro-gravity conditions. In summary, EHD research can lower transport costs through reducing the weight of components.

1.1 EHD in the plane and cylindric geometry

EHD is investigated mainly in three different geometries. The plane capacitor represents the most simple geometry, see Fig. 1 (left). Convection in a rectangular cavity induced by the DEP force and under the influence of the Earth's gravity is comparable to Rayleigh-Benard (RB) convection. Assuming constant fluid properties at reference locations allows scaling with respect to the Rayleigh and Prandtl numbers. Pioneering work on EHD in rectangular cavities has been done by Roberts [74] and Turnbull [90] in the late 1960s. They investigated the stability of the conductive state even in the absence of Earth's gravity, which is an important limiting case for space applications. This theoretical work has been extended and validated by laboratory experiments by Stiles [84], Stiles et al. [85], Smorodin [82]. Recently, TEHD-induced heat transfer under micro-gravity conditions has been studied numerically by, e.g., Fogaing et al. [25]. They compared the heat flux of RB convection with that of EHD convection for a large range in the Prandtl number and derived a power law for the heat flux in the EHD case. A detailed stability analysis was performed by Yoshikawa et al. [98, 97]. In particular, the role of dielectric heating was studied in [99]. The experimental investigation of RB-like convection in a plane capacitor is planned for 2020 and 2021 during parabolic flight campaigns (PFC) conducted by the department for aerodynamics and fluid dynamics (LAS) of the Brandenburg University of Technology Cottbus-Senftenberg.

The cylindrical gap is another important geometry, see Fig. 1 (middle). Experiments in a cylindrical capacitor dedicated to PFC have been developed and performed at the LAS, see [30, 58, 60, 61, 79]. Between 2016 and

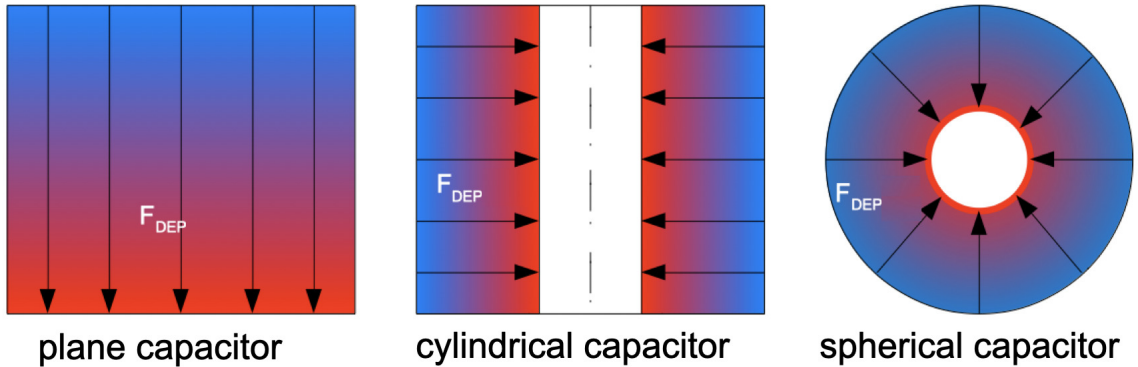


Figure 1: Sketches of plane-, cylindrical- and spherical capacitors used for EHD studies. The colors indicate the thermal stratification for a convective case. Arrows show the direction of the dielectrophoretic force field (DEP).

2019, five campaigns successfully observed the occurrence of convective instabilities caused by the DEP force during low gravity phases (22 sec of $10^{-2}g_0$) for different fluids, aspect ratios and control parameters. Research on thermo-electric convection in a cylindrical gap also has direct industrial applications such as cylindrical heat exchangers for electronic devices, see, e.g., [21] or for the plane capacitor [54].

The focus of this work is on the spherical gap geometry (Fig. 1 (right)), presented in the following sections.

1.2 Convection and EHD in the spherical gap

In a first approximation, the planetary interior and planetary atmospheres are confined fluid layers situated between two spherical shells. Hence, the fluid flow is determined by the boundaries of the system, which are the inner and outer shell. The inner shell represents the planetary inner core or the deep, blocking-pattern atmospheric layers of e.g. gas giants. The outer shell represents the crust, the upper boundary of the climate-relevant atmosphere or, in the case of a gas giant, a region where the gas concentration decreases significantly. This simplified viewpoint makes it possible to test models with laboratory experiments and numerical simulations. The main advantage of such experiments is the reproducibility and the ability to measure properties of the fluid flow, which are e.g. parameterized by semi-empirical closure models, see, e.g., [78].

However, such laboratory experiments are difficult to establish. Earth's gravitational field would dominate or at least significantly contribute to any radial force field in a spherical experiment, which makes it very difficult to deduce meaningful results. The centrifugal force can be used as a radial force field to mimic buoyancy. However, this works only for fast rotating cases, see, e.g., [6], and requires an inverted thermal gradient (outer shell heated, inner shell cooled) to establish an unstable convection system. This setup cannot be used to investigate non-rotating cases and fluid flows with complex boundary conditions. The projection of a hemisphere onto a cylinder is one way to overcome some of these challenges, e.g., by making use of a baroclinic wave tank ([4], [92]), although various phenomena, such as equatorial waves cannot be investigated with this setup. The most promising solution is to set up a spherical gap experiment with a DEP force-based radial force field in a microgravity environment. By applying temperature boundary conditions along with rotation, it is possible to simulate core convection, mantle convection or atmospheres, wherein convective features can be studied.

Convection in the spherical gap geometry is of great interest for astrophysical and geophysical applications. For example, fluid flow based on convective transport is witnessed by observing granules forming a dense network over the entire surface of the Sun and other stars [64]. Convection is the most important transport process in the Earth's mantle and core, in terrestrial planets, the Moon and the Galilean satellites of Jupiter [77, 65, 76]. However, understanding convective flows requires physical models, accompanying numerical simulations and observation data along with laboratory experiments. In the past decades, various experiments were conducted to test and validate convection models. However, the axial gravity on Earth makes it difficult to investigate

large scale flows in the spherical gap geometry. Busse and Carrigan [6] used the centrifugal force to overcome gravitational acceleration. In the rotating spherical gap, they observed convective columns ('columnar cells') aligned nearly parallel to the rotation axis. Another possibility to mimic a radial gravity field is by using thermomagnetic convection exhibited by magnetic fluids trapped between magnets. The use of magnetic fluids for geophysical applications was first described by Ohlsen and Rhines [66] and first simulated by Fröh [26]. The central force field in thermomagnetic systems differs from gravitational fields in its radial dependency. However, basic aspects of spherical gap convection were captured with this approach. The main disadvantage of thermomagnetic driven convection is the inhomogeneous magnetic field.

The controllability of the DEP force is much better than the magnetic field in the case of thermomagnetic convection. The strength of the electric field in the radial direction scales with $\sim |\mathbf{E}|^2 \nabla \epsilon$, see Eq. 7. Thus, the resulting electric acceleration decreases with $\sim |\mathbf{E}|^2 \nabla \epsilon \sim (r^{-2})^2 r^{-1} = r^{-5}$ in radial direction, see Eq. 13. Low voltages applied on a small gap width reduce the non-linear radial dependency but limit the scope of applications. Wide gaps and high voltages provide a compromise between geophysical applications with radial dependencies of the gravity of $\sim r^{-1}$ or $\sim r^{-2}$ and technical realization. Best results are obtained under microgravity conditions, where the influence of the Earth's gravity is minimized. In the past forty years, several TEHD experiments have been conducted under microgravity conditions. For example, Hart et al. [39] investigated TEHD driven convection in the half-dome Geophysical Fluid Flow Cell (GFFC) experiment at SpaceLab3. They observed columnar convection for high rotation rates and roll-like cells for differentially heated boundaries. The entire experimental time was 110h, wherein 50.000 photographs were produced. Several experiments investigating convective flows in microgravity conditions have been performed: Liu et al. [53] conducted short-time experiments on a parabolic flight campaign in 1991. Microgravity conditions of several minutes were obtained on the TCM Volna ballistic rocket by Egbers et al. [17] and Kuhl et al. [48]. Correct, Kuhl was administrator. However, this manuscript presents an overview of experiments performed in sounding rockets.

This thesis reviews the GeoFlow experiment which was conducted on the (ISS) between 2008 and 2017. The GeoFlow experiment was a spherical gap experiment designed to investigate convection driven by a temperature difference between the shells and also convection driven by internal heating, for three rotation rates. The GeoFlow/AtmoFlow research was funded by ESA Grant No. AO-99-049; by DLR Grants No. 50WM0122, No. 50WM0822, and No. 50WM1841, by the SOKRATES/ERASMUS-program LIA-ISTROF (CNRS-cooperation), and DFG No. TR986/6-1. The 'GeoFlow Topical Team' (ESA 18950/05/NL/VJ) is a group of scientists located all over Europe. They devoted their research to the field of GeoFlow and AtmoFlow as it is summarized in Fig. 2. The Topical Team is under the special direction of Prof. Dr.-Ing. Christoph Egbers (head of department for aerodynamics and fluid dynamics (LAS) of the Brandenburg University of Technology Cottbus-Senftenberg).

Additionally, the AtmoFlow experiment is introduced, which is planned for launch to the ISS in 2024. The experimental setup of GeoFlow is presented in Sec. 1.3. The physical model and the governing equations are derived in Sec. 2. Numerical methods to solve the governing equations and post-processing techniques are described in Sec. 3. The focus of this thesis will be the analysis of the fluid flow in the non-rotating case in Sec. 4 and the rotating case in Sec. 5. A short discussion of fluid flows with high viscosity contrasts is presented in Sec. 6. The new AtmoFlow experiment is presented in Sec. 7. A discussion and concluding remarks are given in Sec. 8.

I hereby declare that all results of the presented work have been published in peer-reviews journals and presented at conferences. A detailed list of all references is given at the end of each section.

1.3 The GeoFlow experiment

The GeoFlow experiment on the ISS (see Fig. 3 (left)) featured a concentric spherical gap capacitor and was used for the investigation of thermal convection. The experimental system had a gap width of 0.0135m, with an outer radius of $R_{out} = 0.027$ m and an inner radius of $R_{in} = 0.0135$ m, which yielded an aspect ratio

Topical Team GEOFLOW ESA 18950/05/NL/VJ	Tasks
<u>Team co-ordination:</u> <i>Christoph Egbers</i> BTU Cottbus-Senftenberg Germany	Preparatory studies: <ul style="list-style-type: none"> • laboratory experiments on spherical gap flow model • design, parameterization and operation of ISS experiment • linear stability analysis and 3D numerical simulation of convective flow • imaging analysis and comparison of numerical and experimental data
<i>Rainer Hollerbach</i> University of Leeds United Kingdom	Development of 3D numerical codes: <ul style="list-style-type: none"> • thermal convection with and without rotation, differential rotation, viscosity contrast, internal heating. • implementation of magneto-hydrodynamics in the 3D-model
<i>P. Chossat & Ph. Beltrame*</i> CIRM Marseille, France * Univ. Avignon, France	Development of bifurcation analysis: <ul style="list-style-type: none"> • bifurcation analysis with and without rotation, mode interactions • analysis of preferred regimes, patterns, frequencies & bifurcations
<i>Laurette Tuckerman</i> ESPCI, Paris, France	Non-linear stability analysis: <ul style="list-style-type: none"> • bifurcation of time-dependent states • path following methods
<i>Innocent Mutabazi</i> University of LeHavre	Couette-Taylor instabilities <ul style="list-style-type: none"> • Thermal convection and nonlinear dynamics
<i>Fred Feudel</i> University of Potsdam Germany	Non-linear stability analysis: <ul style="list-style-type: none"> • path following methods • non-linear dynamic analysis methods
Associated partners:	<i>Tilman Spohn, Doris Breuer</i> DLR, Planetary Sciences, Berlin-Adlershof, Germany

Figure 2: Members of the 'GeoFlow Topical Team' (ESA 18950/05/NL/VJ) and their tasks related to GeoFlow research.

of $\eta = R_{in}/R_{out} = 0.5$. Fig. 4 depicts a vertical slice through the setup featuring a temperature distribution calculated via numerical simulation. Two external thermalized fluid circuits established a temperature difference of $0.4\text{ K} \leq \Delta T \leq 9.5\text{ K}$ between the two shells. To induce a dielectrophoretic force and hence a radial buoyancy force, a high frequency, alternating electric field was applied. The strength of the force was controlled via the applied thermal boundary conditions and the amplitude of the electric field. To study a variety of convection phenomena, the electric field was adjusted between 1800 V and 6500 V. To account for the rotational force, the sphere was able to rotate with three different angular velocities $\Omega = 2\pi f$, with $f = 0.008, 0.8$ or 1.6 Hz. The dielectric loss of the working fluid, 1-Nonanol, was controlled by the high frequency changing of the electric field, which caused internal heating which was investigated within the system. Fig. 3 (middle) shows the GeoFlow core facility with the fluid-filled spherical gap. The whole experimental container is depicted in Fig. 3 (middle). It was integrated in the Fluid Science Lab of the Columbus module of the ISS.

The GeoFlow experiment could simulate three rotation rates f , five voltages $V_{rms} = V_0/\sqrt{2}$ and eight temperature differences ΔT , where two reference temperatures T_0 were measured at the outer shell. These input properties defined 240 experimental points (EP), where 160 EPs were rotation cases ($f = 0.8\text{ Hz}$ and $f = 1.6\text{ Hz}$) and 80 EPs were weakly rotating (in the following denoted as 'non-rotating' with $f = 0.008\text{ Hz}$). All rotating cases are summarized in Fig. 16, which also presents the full parameter range (in electric Rayleigh number) of the non-rotating cases.

All numerical results presented are based on EPs defined in the GeoFlow *Experimental Scientific Requirements (ESR)* document. A set of eight temperature differences is called a 'run' and can be set to have a sequential increase of voltages and rotation rates.

The visualization of the fluid flow was performed by utilizing a Wollaston Shearing Interferometry (WSI) system which measures the gradient of the refractive index [16, 111]. While the refractive index gradient varies with the thermal distribution within the spherical gap, certain fringe patterns can be observed where the thermal gradient changes the (temperature-dependent) refractive index of the fluid. For example, single convective cells



Figure 3: (left) International Space Station (ISS) (source: ESA), (middle) GeoFlow core facility (source: LAS/BTU), (right) GeoFlow container (source: LAS/BTU).

appear as butterfly patterns and sheet-like flows appear as parallel lines (see Fig. 20c). Unfortunately, more complicated visualizations of the convective flow could not be performed for ISS safety reasons. The recording plane of the camera of the WSI was mounted at a meridional angle of $\theta = 30^\circ$ with the North Pole located at $\theta = 0^\circ$. Thus, the recorded interferograms covered a range of 88° , ranging from $\theta = -14^\circ$ to $\theta = 74^\circ$, see Fig. 4. From a series of images it was possible to reconstruct the radially averaged temperature field of the entire northern hemisphere. While the resolution of the images enabled a satisfactory analysis for the laminar flow regime, it caused imprecise reconstructions in the transient and turbulent regimes. To overcome these restrictions, only single interferograms were analyzed for the transient and turbulent regimes.

Experimental specifications for the AtmoFlow experiment are presented in Sec. 7.

1.4 Research objectives

The GeoFlow and AtmoFlow experiments make it possible to investigate fluid flows which are driven by internal heating, a boundary temperature difference, rotation or complex boundary conditions. They will enable deep insights into EHD driven fluid flows, which can be used for validating convection models of planetary interior shells or atmospheres. The main goal is the elucidation of EHD driven convection in the rotating and non-rotating spherical shell geometry. This will allow the testing of linear stability analysis regarding base flows driven by the centrifugal force (see [87]), convective onsets and bifurcation scenarios. The objectives focus on the following topics:

- The validity of established *models for EHD* driven flows is to be evaluated for such experiments. In particular, this will allow one to address the consequences of simplifications such as the $\sim r^{-5}$ -scaling of the central force.
- The role of *mixed heating* (internal heating and temperature difference across the gap) is not well understood in the spherical gap geometry. The construction of optimized heat exchangers, EHD-based pumps and nozzles will benefit from this research. Furthermore, the enhancement of convective heat transfer in the absence of gravity (e.g. on space stations or spacecrafts) can be controlled more efficiently when electric fields are used to induce thermal buoyancy.
- The *influence of rotation* on the onset of convection, transitions and the turbulent regime are in the focus of both experiments. Models of rotating convection shall be tested with regard to the analogy between EHD driven flows and RB convection.
- Fluid flows with strong *viscosity contrasts* are found, e.g., in the Earth's mantle. The influence of such contrasts on the fluid flow shall be studied with suitable fluids. It is expected that the use of working fluids with temperature-dependent viscosities enables the occurrence of new fluid structures which can have important geophysical implications.

- Advanced *post-processing methods* are needed to compare experimental outcomes and numerical results. These include machine learning algorithms, statistical evaluation and visualization.

2 Model formulation

A spherical capacitor with gap width $d = R_{out} - R_{in}$, having the same physical specifications as in the GeoFlow experiment is filled with a dielectric fluid.

The temperature field is imposed a) with a temperature difference between the inner (denoted with index 1) and outer shell (denoted with index 0) with $\Delta T = T_1 - T_0 > 0$ and b) by an internal heat source based on dielectric heating. A cross-section schematic of the experiment is shown in Fig. 4 along with the thermal boundary conditions. All reference fluidic and electric properties are considered constant and are taken at the outer shell. An electrically-linear quasi-electrostatic field acting on an incompressible dielectric fluid is assumed such that the net force on each dipole is given by the *Kelvin polarization force density* $\mathbf{F} = \mathbf{P} \cdot \nabla \mathbf{E}$, where $\mathbf{P} = \epsilon_0(1 - \epsilon_r)\mathbf{E}$ is the polarization vector, ϵ_0 the vacuum permittivity, ϵ_r the relative permittivity and \mathbf{E} the electric field. The electrical linearity is defined with $\mathbf{E} = \mathbf{E}(\rho, \epsilon, \mathbf{D})$ where ρ is the density, $\epsilon = \epsilon_0\epsilon_r$ is the permittivity, ϵ_0 is the vacuum permittivity, ϵ_r is the relative permittivity and \mathbf{D} is the displacement field.

Thus, the electric *Korteweg-Helmholtz force density* describes the force acting on the fluid and is valid for the given assumptions according to [9, 101, 62, 114] and is given by

$$\mathbf{F}_{KH} = \rho_f \mathbf{E} - \frac{1}{2} |\mathbf{E}|^2 \nabla \epsilon + \nabla \left(\frac{1}{2} \rho \frac{\partial \epsilon}{\partial \rho} |\mathbf{E}|^2 \right). \quad (1)$$

The first term on the right hand side of the equation represents the Coulomb force, the second term the dielectrophoretic force \mathbf{F}_{DEP} , and the last term the electro-strictive force defining the electro-strictive pressure. The electro-strictive term is a gradient force that can be lumped with the pressure term p in the dynamical equations of fluid motion.

A detailed description of the derivation of \mathbf{F}_{KH} is given in Melcher [59].

The fluid is considered to not carry free charges such that $\rho_f = 0$. An alternating electric field with potential $\Phi(t) = \sqrt{2}V_0 \cos(\omega t)$ is applied at one electrode with $\omega = 2\pi f$, where f is the AC frequency and $V_0 = \sqrt{2}V_{rms}$ the capacitor voltage. The model of the electrostatic equilibrium is justified for $\tau_e^{-1} \ll f \ll c/d$ where τ_e , is the charge relaxation time and c is the speed of light [74].

The electro-static potential field is solved for $\nabla \Phi = -\mathbf{E}$ where $\Phi(R_{out}) = 0$ and $\Phi(R_{in}) = V_0/\sqrt{2}$. The dielectric loss is given by the power dissipation per unit volume, written as

$$Q = \omega \epsilon'' \epsilon_0 |\mathbf{E}|^2 = 2\pi f \epsilon_0 \epsilon' \tan \delta |\mathbf{E}|^2 \quad (2)$$

where ϵ' is the real part of the relative permittivity, ϵ'' the imaginary part of the permittivity and $\tan \delta = \epsilon''/\epsilon'$ the dielectric loss factor [31].

2.1 Governing equations

The equations describing the fluid flow are based on the Oberbeck-Boussinesq approximation (OBA) being applied to a dielectric fluid, confined in a rotating spherical shell capacitor with a fixed applied voltage V_{rms} . The OBA assumes low expansion rates with temperature $\alpha \Delta T \ll 1$ where α is the thermal expansion coefficient with a low thermoelectric parameter $e \Delta T \ll 1$ where

$$e = -\frac{1}{\epsilon_r} \frac{\partial \epsilon_r}{\partial T}$$

is the coefficient of the thermal permittivity decrease [62]. Density and relative permittivity depend approximately linearly from temperature in the GeoFlow parameter range for $293K \leq T \leq 313K$, (ADS, Report on Nonanol electric properties). Under these conditions, the OBA is valid for density $\rho = \rho_0(1 - \alpha(T - T_0))$ and permittivity $\epsilon = \epsilon_0 \epsilon_r(T_0)(1 - e(T - T_0))$ with $\epsilon_r(T_0)$ is the relative permittivity at reference temperature T_0 .

The electro-strictive pressure force $\mathbf{F}_{ES} = \nabla p_{ES}$ is in this case jointly treated with the hydrodynamic pressure

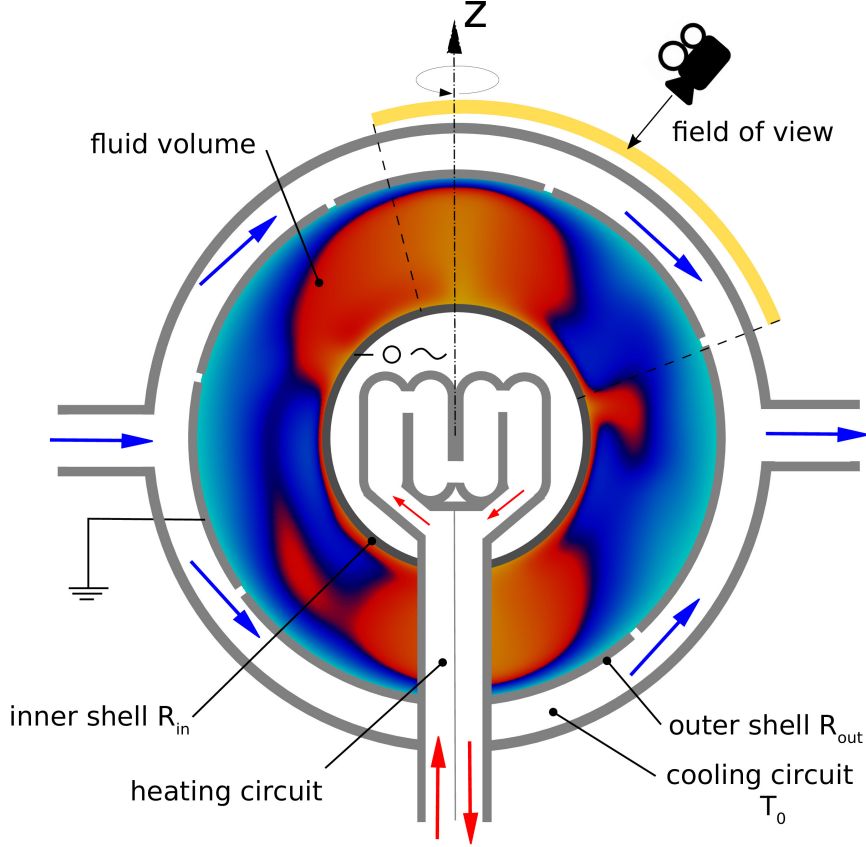


Figure 4: Schematic cross section of the GeoFlow experimental setup. A numerical simulation visualizes the fluid flow in the gap.

in the incompressibility formulation. The problem can now be described with the Navier-Stokes equation by considering the above formulations as

$$\frac{\partial \mathbf{u}}{\partial t} + (\mathbf{u} \cdot \nabla) \mathbf{u} = -\frac{1}{\rho_0} \nabla p - \frac{1}{2\rho_0} |\mathbf{E}|^2 \nabla \epsilon - 2\boldsymbol{\Omega} \times \mathbf{u} - \frac{\rho}{\rho_0} \boldsymbol{\Omega} \times (\boldsymbol{\Omega} \times \mathbf{r}) + \nu \nabla^2 \mathbf{u}, \quad (3)$$

where \mathbf{u} is the velocity, p the combined pressure (to be more precise, this is the Bernoulli energy function), $\boldsymbol{\Omega}$ the rotation vector, \mathbf{r} the position vector and ν is the kinematic viscosity. The temperature equation is defined as

$$\frac{\partial T}{\partial t} + (\mathbf{u} \cdot \nabla) T = \kappa_T \nabla^2 T + H \quad (4)$$

where T is the temperature, κ_T the thermal diffusivity and H the dielectric heat source which equals to $Q/(\rho c_P)$ where c_P is the specific heat capacity. Mass conservation is given by the continuity equation

$$\nabla \cdot \mathbf{u} = 0. \quad (5)$$

The non-uniformity of the electric field and the thermo-electric feedback is calculated via the Gauss equation, [98],

$$\nabla \cdot (\epsilon \mathbf{E}) = 0. \quad (6)$$

Following Eqs. 1-6 above, the direction of the \mathbf{F}_{DEP} is towards the permittivity gradient and is therefore collinear with the gradient of the electrostatic energy stored in the fluid [62]. The dielectrophoretic force has non-vanishing components in the azimuthal and poloidal direction, respectively. By using the OBA to give a temperature dependence to the permittivity with the identity $\nabla(\epsilon |\mathbf{E}|^2) = \epsilon \nabla |\mathbf{E}|^2 + |\mathbf{E}|^2 \nabla \epsilon$, one can write the

\mathbf{F}_{DEP} force as

$$\mathbf{F}_{\text{DEP}} = -\frac{1}{2}|\mathbf{E}|^2\nabla\epsilon = \frac{1}{2}\nabla(|\mathbf{E}|^2\epsilon_r\epsilon_0e\Theta) - \frac{1}{2}\epsilon_r\epsilon_0e\Theta\nabla|\mathbf{E}|^2 \quad (7)$$

where Θ is temperature difference written as $T - T_0$. The first term on the far-right hand side is a gradient force and is included in the pressure gradient. The remaining term can be rewritten equivalently as a thermal buoyancy force, $\mathbf{F} = -\rho_0\alpha\Theta\mathbf{g}_e$ with

$$\mathbf{g}_e = \frac{e}{\rho_0\alpha}\nabla\left(\frac{\epsilon_0\epsilon_r(T_0)|\mathbf{E}|^2}{2}\right). \quad (8)$$

This term is known as the *electric gravity* which represents a mean acceleration. Hence, \mathbf{g}_e alone is not suitable for the analysis of buoyancy related phenomena. In the following, the corresponding *dielectrophoretic acceleration* $\mathbf{a}_e = \mathbf{F}_{\text{DEP}}/\rho_0$ is instead used which accounts for all spatial variations of the permittivity and the temperature. This is not a scaling! Scaling is always performed with a dim-less scaling parameter and ρ_0 is not dim-less. This includes the consideration of the sign change of the dielectrophoretic acceleration under certain conditions which will also change the sign of the buoyancy term. A comparable approach is used by Mutabazi et al. [62] where the electric gravity is split into a base state and a fluctuating part.

The dimensionless governing equations are obtained by applying the scaling length $r = r^*d$, velocity $\mathbf{u} = \mathbf{u}^*\kappa_T/d$, time $t = t^*d^2/\kappa_T$, electric field $\mathbf{E} = \mathbf{E}^*V_{rms}/d$, temperature difference $T = T^*\Delta T + T_0$ and pressure $p = p^*\rho_0\kappa_T/d^2$. Henceforth, variables with asterisks refer to dimensionless quantities. The dimensionless dielectrophoretic acceleration \mathbf{a}_e^* is,

$$\mathbf{a}_e^* = -\frac{1}{2}|\mathbf{E}|^2\nabla\epsilon(T)/(d^3/(V_{rms}^2\epsilon_0\epsilon_r(R_{out}))). \quad (9)$$

For the convenience of the calculations the electric field \mathbf{E}^* is split into two parts,

$$\mathbf{E}^* = \mathbf{E}_0^*(r^*) + \mathbf{E}_1^*(r^*, \theta, \phi), \quad (10)$$

$$\mathbf{E}_0^*(r^*) = -\nabla\Phi_0^*(r^*), \quad \mathbf{E}_1^*(r^*, \theta, \phi) = -\nabla\Phi_1^*(r^*, \theta, \phi). \quad (11)$$

where poloidal and toroidal angles are denoted by θ and ϕ , respectively. Thus, the field $\mathbf{E}_0^*(r^*)$ satisfies $\nabla \cdot \mathbf{E}_0^*(r^*) = 0$ which can be calculated analytically

$$\mathbf{E}_0^*(r^*) = \frac{1}{\sqrt{\Gamma}}\frac{1}{r^{*2}}\mathbf{e}_{r^*} \quad (12)$$

where $\Gamma = (1 - \eta)^4/\eta^2$ is a geometrical correction factor for the spherical shell and $\eta = R_{in}/R_{out}$ is the radius ratio. Using Eq. 12 and the limiting case of $|\mathbf{E}_1^*| \ll |\mathbf{E}_0^*|$ for the electric field, the averaged radial component of the electric gravity with fluid properties defined at radius $r = R_{out}$ is,

$$g_e(r) = -V_0^2\frac{\epsilon_0\epsilon_r}{\rho_0}\frac{R_{in}R_{out}}{(R_{out} - R_{in})^2}\frac{1}{r^5}. \quad (13)$$

Omitting the asterisk the dimensionless Navier-Stokes equation is obtained,

$$\text{Pr}^{-1}\left(\frac{\partial\mathbf{u}}{\partial t} + (\mathbf{u} \cdot \nabla)\mathbf{u}\right) = -\text{Pr}^{-1}\nabla p + \nabla^2\mathbf{u} - \frac{1}{4}\text{B} \cdot \Gamma \cdot \text{L} \cdot T \cdot \nabla|\mathbf{E}|^2 - \text{Ek}^{-1}\mathbf{e}_z \times \mathbf{u} + \text{L} \cdot \text{Fr} \cdot T r \sin\Theta \mathbf{e}_{eq} \quad (14)$$

where $\text{Pr} = \nu/\kappa_T$ is the Prandtl number, $\text{B} = e/\alpha$ the ratio of expansion coefficients,

$$\text{L} = \frac{\alpha\Delta T|g_{e,R_{out}}|d^3}{\nu\kappa_T}$$

the electric Rayleigh number, $\text{Ek} = \nu/(2\Omega d^2)$ the Ekman number, r the radial distance, \mathbf{e}_{eq} the unit vector in equatorial plane and $\text{Fr} = \Omega^2 d/|g_{e,R_{out}}|$ is the Froude number measuring the relative strength of the centrifugal

and the (electric) buoyancy force [13]. All defined dimensionless parameters for the GeoFlow experiment are summarized in Tab. 1.

The dimensionless equation for temperature is

$$\frac{\partial T}{\partial t} + (\mathbf{u} \cdot \nabla)T = \nabla^2 T + \frac{C_T}{B\Gamma L} |\mathbf{E}|^2. \quad (15)$$

The electric field is calculated via the Gauss equation and Eqs. 10-11,

$$\nabla^2 \Phi_1 = \frac{C_E \Gamma L}{1 - C_E \Gamma L T} \nabla T \cdot (\nabla \Phi_0(r) + \nabla \Phi_1(r, \theta, \phi)) \quad (16)$$

with the dielectric loss parameter $C_T = 4\pi f e \epsilon_0^2 \epsilon_r^2 \tan \delta V_{rms}^4 / (c_p \rho^2 \nu \kappa)$ and the convective parameter $C_E = \rho \nu \kappa / (2\epsilon_0 \epsilon_r V_{rms}^2)$.

For $|\mathbf{E}_1| \ll |\mathbf{E}_0|$ the Navier-Stokes equation and the temperature equation read,

$$\text{Pr}^{-1} \left(\frac{\partial \mathbf{u}}{\partial t} + (\mathbf{u} \cdot \nabla) \mathbf{u} \right) = -\text{Pr}^{-1} \nabla p + \nabla^2 \mathbf{u} + \text{B} \cdot \text{L} \cdot T \cdot \frac{1}{r^5} \mathbf{e}_r - \text{Ek}^{-1} \mathbf{e}_z \times \mathbf{u} + \text{L} \cdot \text{Fr} \cdot T r \sin \theta \mathbf{e}_{e\phi} \quad (17)$$

and

$$\frac{\partial T}{\partial t} + (\mathbf{u} \cdot \nabla)T = \nabla^2 T + \frac{C_T}{B\Gamma^2 L} \frac{1}{r^4}, \quad (18)$$

respectively. Apart from the internal heating term and the geometrical aspects, this set of equations is identical with the governing equations presented in Feudel et al. [22] (Eq. 1a-1c) and for the rotating case shown by Curbelo et al. [13] (Eq. 1-2). This model is not suitable for describing pure internal heating ($T_1 = T_0$). In that case the Rayleigh number $L = 0$ resulting in an undefined source term in the temperature equation Eq. 18. For completeness, see Travnikov et al. [89] for this special case.

The heating parameter, λ , defined as

$$\lambda = \frac{1}{2} \frac{C_T}{B\Gamma L} \quad (19)$$

is used to quantify the heating source in the system. The heating parameter is in fact a result of the energy balance in terms of Nusselt numbers,

$$\text{Nu}_{\text{in}} = \int_{S_{\text{in}}} \frac{dT_{0I}(r)}{dr} dS_{\text{in}}$$

and

$$\text{Nu}_{\text{out}} = \int_{S_{\text{out}}} \frac{dT_{0I}(r)}{dr} dS_{\text{out}}$$

, evaluated at the inner and outer shell, respectively. Here, $T_{0I}(r)$ is the temperature field for vanishing velocity field $\mathbf{u} = \mathbf{0}$, see Eq. 36.

Their relationship is written as

$$\text{Nu}_{\text{in}} - \text{Nu}_{\text{out}} + 2\lambda \int_V \mathbf{E}_0^2 dV = 0 \text{ for } \lambda < 1 \quad (20)$$

$$-\text{Nu}_{\text{in}} - \text{Nu}_{\text{out}} + 2\lambda \int_V \mathbf{E}_0^2 dV = 0 \text{ for } \lambda > 1. \quad (21)$$

The strength of the internal heating is measured by λ , where $\lambda > 1$ indicates strong internal heating and $\lambda < 1$ indicates weak internal heating. For $\lambda = 1$ internal heating increases the fluid's temperature inside the spherical gap geometry until the heat flux through the surfaces is balanced with the internal heating rate. When $\lambda > 1$, the temperature difference across the gap does not contribute significantly to the global energy transport and results in a parabolic mean temperature profile.

dimensionless parameter	value
Ekman number (Ek)	$2.64 \times 10^{-3} - 7.62 \times 10^{-3}$
Froude number (Fr)	$5.1 \times 10^{-2} - 2.66$
Prandtl number (Pr)	$1.24 \times 10^2 - 1.75 \times 10^2$
electric Rayleigh number (L)	$3.73 \times 10^2 - 1.59 \times 10^5$
dielectric loss parameter (C_T)	$9.06 \times 10^3 - 2.27 \times 10^6$
convective parameter (C_E)	$2.02 \times 10^{-7} - 3.54 \times 10^{-6}$
expansion ratio (B)	11.20 – 12.40
heating parameter (λ)	0.16 – 60

Table 1: Dimensionless parameter range of the GeoFlow experiment.

Published and presented in:

F. Zaussinger, P. Haun, M. Neben, T. Seelig, V. Travnikov, C. Egbers, H. Yoshikawa, and I. Mutabazi. Dielectrically driven convection in spherical gap geometry. *Phys. Rev. Fluids*, 3:093501, Sep 2018. doi: 10.1103/PhysRevFluids.3.093501. URL <https://link.aps.org/doi/10.1103/PhysRevFluids.3.093501>

C. Egbers, F. Zaussinger, P. Haun, P. Canfield, V. Travnikov, and A. Froitzheim. Convection in the spherical gap under micro-gravity conditions: From Earths mantle to atmospheric flows. In *20th Int. Couette-Taylor Workshop*. Aix Marseille universite, 2018. URL <https://ictw20.sciencesconf.org/data/pages/FinalProgramIV.pdf>

F. Zaussinger, P. Haun, I. Mutabazi, and C. Egbers. Dielectrically driven convection in spherical gap geometry. In *Scientific programm EFMC12*, volume 1 of *Scientific programm EFMC*, page 46, September 2018. http://info.tuwien.ac.at/efmc12/EFMC12_program_v3.2.pdf

F. Zaussinger. GeoFlow I and GeoFlow II: A Review. In *Book of abstracts, School ISTROF 2019, Instabilities and Turbulence in Strato-Rotational Flows, Cottbus*. BTU Cottbus-Senftenberg, 2019

F. Zaussinger. Influence of internal heating on convection in the rotating spherical gap. In *Book of Abstracts - ETC 2019*, 2019. URL <http://www.symposium.it/files/eventi/84/etc-2019-561.pdf>

V. Travnikov, F. Zaussinger, P. Haun, and C. Egbers. Influence of dielectrical heating on convective flow in a radial force field. *Phys. Rev. E*, 101:053106, May 2020. doi: 10.1103/PhysRevE.101.053106. URL <https://link.aps.org/doi/10.1103/PhysRevE.101.053106>

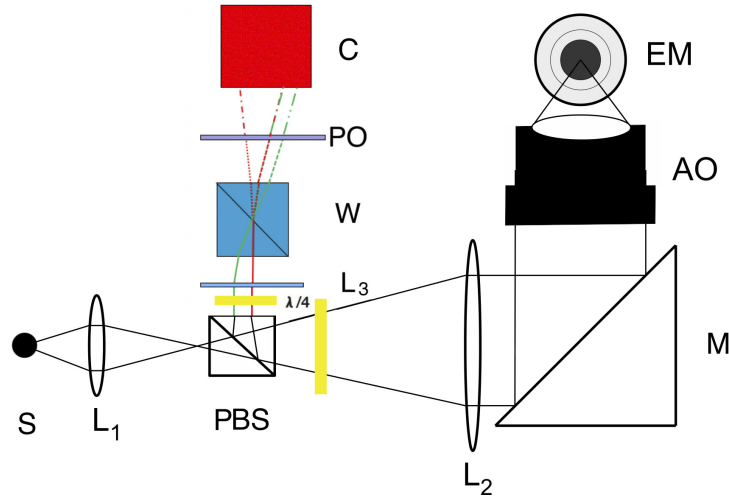
3 Numerical methods and post-processing

3.1 Interferometry and flow visualization

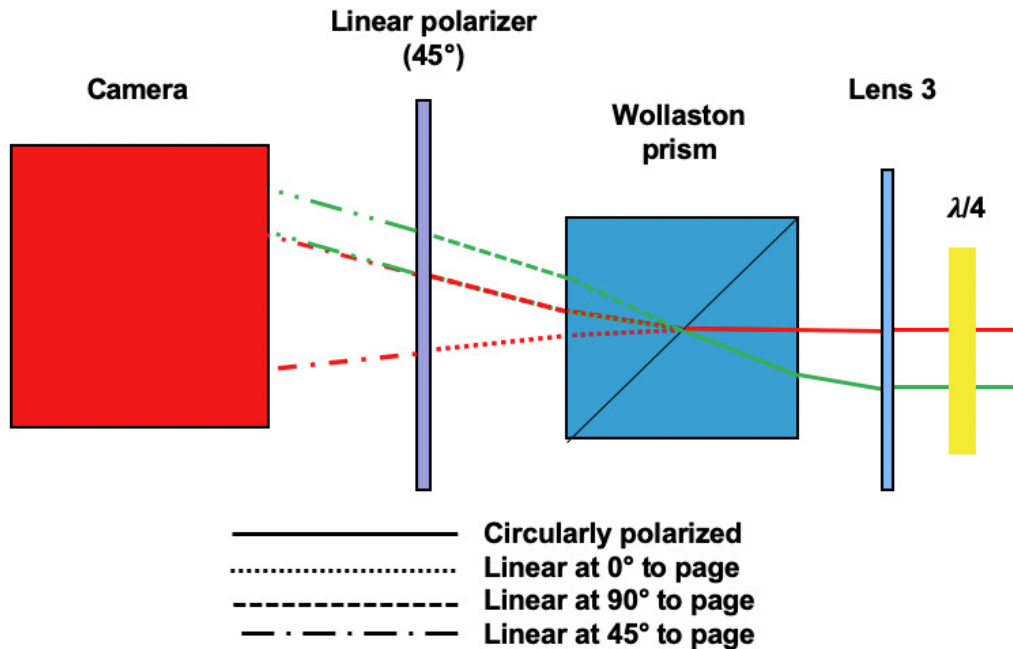
The Optical Diagnostics Module (ODM) (cf. Dupont et al. [16]) of the Fluid Science Laboratory (FSL) is utilized for the visualization of the fluid flow of the GeoFlow experiment. A main diagnostic component of the optical diagnostics module is the Wollaston shearing interferometry (WSI) unit which measures first derivatives of the fluid's refractive index (Fig. 5). The refractive index of the GeoFlow II working fluid 1-Nonanol is $n=1.4338$ at 20°C (source: Merck index) and decreases linearly with the temperature for $293\text{K} \leq T \leq 313\text{K}$. Due to this dependency a thermal gradient yields phase shifts of adjacent beams of laser light which result in a interferometry fringe pattern. Interferometry is a technique that generates interference of electromagnetic waves. A common interferometry technique is the Wollaston shearing interferometry. The interference of light rays is generated by a birefringence material, the Wollaston prism shown in sketch Fig. 5. Here, Fig. 5a depicts a global view on the setting and Fig. 5b shows a detailed view on the section around the Wollaston prism.

1. Linearly (plane) polarized light is emitted from source (S). This is typically a laser emitting a collimated beam.
2. A linearly beam goes through a polarized beam splitter (PBS).
3. Between beam splitter and lens L_2 a $\lambda/4$ plate is placed to convert linearly polarized light into circular polarised light.
4. The beam goes via a mirror (M) through an adaption optics (AO) into the experiential medium (EM, GeoFlow) and passes the focal point in the middle of the sphere. Hence, the curvature does not deflect the beam. Then the beam is reflected at the inner sphere and passed back the same beam path. The polarisation state is again changed at the $\lambda/4$ plate to linear polarized light but orthogonal to the emitted light by the laser. This is caused by the rotation of the $\lambda/4$ plate with a 45° angle. Thus, the beam can now be reflected at the polarized beam splitter and passed into the interference section of the system.
5. Fig. 5b shows now a detailed view: A second $\lambda/4$ plate is used to convert the linear polarized light into circular polarized light that is focused via a lens 3 into the Wollaston prism of the interference section. This is called *infinite fringe*. In case the prism is in the plane of the laser beam a *finite fringe* alignment is achieved.
6. The Wollaston prism splits each circular polarized ray into two rays which are orthogonal linearly polarized to each other. The interference is generated by two adjacent rays (see Fig. 5b, green and red line) that are split into four rays where one of each ray is overlapped with other (green and red). Both overlapped rays are orthogonal to each other and linear polarized and passed through a 45° tilted polarizer to interfere both rays on the camera's detector.
7. If the laser beam is correctly focused into the Wollaston prism no fringes are observed. However, any misaligned optical elements including the Wollaston prism or the test section can cause fringe patterns as shown e.g. in Fig. 12a where bended fringes are caused by the misalignment of the Wollaston prism.

Six interferograms per lowest revolution of the annulus ($f = 0.08\text{ Hz}$) are recorded for longtime experiments which yields an imaging frame rate of 0.048 Hz . This frame rate is sufficient to capture quasi-stationary convective processes accurately. The size of the images is limited by the ODM to 992×992 pixels (GeoFlow I,II,Ib) and 640×480 pixels (GeoFlow IIc). Short time experimental runs with an imaging frame rate of 10 Hz are performed, too. These are more difficult to handle, since the size of the video stream is large compared to the available storage capacity of the hard drive in the Video Monitoring Unit (VMU). The frame rate of 10 Hz



(a) Wollaston shearing interferometry of the FSL as used to visualize refractive index variations: C the camera, $L_{1,2,3}$ the lenses, PO the linear polarizer, W the Wollaston prism, PBS the polarized beam splitter, S the collimated laser beam, M the mirror, AO the adaption optics and EM the GeoFlow experiment.



(b) Detailed view on Wollaston prism section. See text for explanation. source: priv. comm. O. Erdogan and P. Szabo (BTU).

Figure 5

makes it possible to follow unsteady, turbulent convective flows precisely, albeit a full rotation at 0.008 Hz results in 1250 images. Lower frame rates, as available in GeoFlow I,II,Ib, are not suited to track turbulent flows. However, only two turns can be recorded at the maximum frame rate until the storage capacity is exhausted.

During the GeoFlow II campaign 1.641.975 images have been recorded. This amount of images calls for an automatization of post-processing. The files are listed in a SQL data base and can be sorted by telemetry data which are available for each image, too. The images are stored as single PNG files or as S-Video streams. The interferograms cover an area of 88° , ranging from $\theta = -14^\circ$ to $\theta = 74^\circ$. At medium rotation frequency of 0.8 Hz there are 25 images recorded in two turns. Hence, in a series of 25 consecutive images the flow field of the entire northern hemisphere can be visualized with patches of $360^\circ/25 = 14.4^\circ$. In case of rotation rate 1.6 Hz four revolution of the annulus are needed to cover all areas by interferograms. The series of images

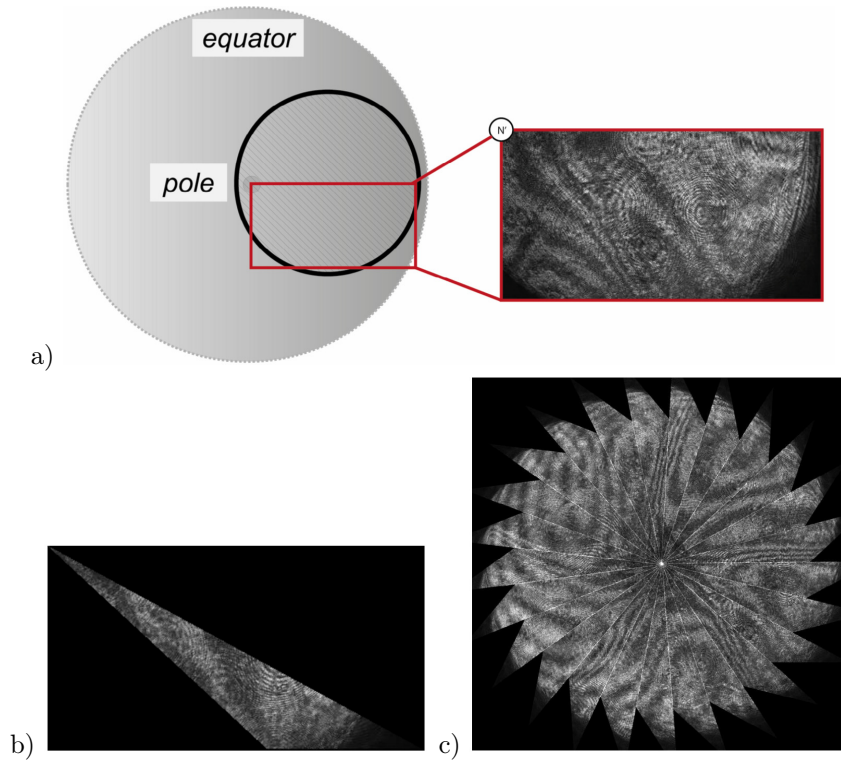


Figure 6: Visualization of the fluid flow in the entire northern hemisphere by glueing sections of the interferograms. a) field of view with partial interferogram in red, b) triangular polygon ('patch') with North Pole in the left upper corner, c) northern hemisphere reconstructed by 25 glued patches. (priv. comm.: Bachelor thesis, O. Erdogdu)

is merged alternately by two or four turns. Highly time dependent flows cannot be reconstruction with this method. However, laminar and transient cases are captured quite good, see Fig. 6. In a row of 25 consecutive images labeled from 1 to 25 with increasing time stamp of 100 ms, the following sorting is used to glue segments ('patches') of 14.4° to a global map: 13,1,14,2,...,24,12,25. Hereby, each patch is a triangle with one vertex the North Pole, one vertex the intersection of the zero meridian with the equator and the intersection of the projection of the 14.4° th longitude onto the interferogram with the equator. The interferometry unit offers two perpendicular settings for the the Wollaston prism. This leads to two different cases of base fringes, which result from distortions in the optical path. One alined with the latitudes, one aligned with the longitudes. The analysis of interferograms of the latter case is more complicated for the rotating case. The rotation axis through the poles favors columnar cells aligned with the longitudes. They are in the same orientation as the the base fringes and lead to recognition problems. Furthermore, the quality of the global reconstruction is enhanced by steep convective plumes, where fringes differ much from the base pattern.

3.2 Artificial interferograms

The experimental interferograms approximate an integral value of the radial component of the refractive index derivatives which are projected on the plane (black) circle shown in Fig. 6(a). Hence, it is not possible to reconstruct the full three dimensional flow field or the temperature distribution in the spherical gap directly with the two-dimensional interferograms. This is caused by two mechanisms. First, the mapping from 3D to 2D is surjective by definition. Therefore, it is impossible to calculate an unique reconstruction of the flow based on interferograms alone. Second, the direction of the refractive index derivative is unknown which makes it difficult to distinguish between cold down-wellings and hot up-wellings. The strategy to determine the temperature distribution in the spherical gap is based on the so called *backward reconstruction*. Three steps are necessary to perform this: a) a numerical simulation is calculated, b) an artificial interferometry is performed on the numerical temperature field, c) the experimental and the numerical interferograms are compared. The crucial

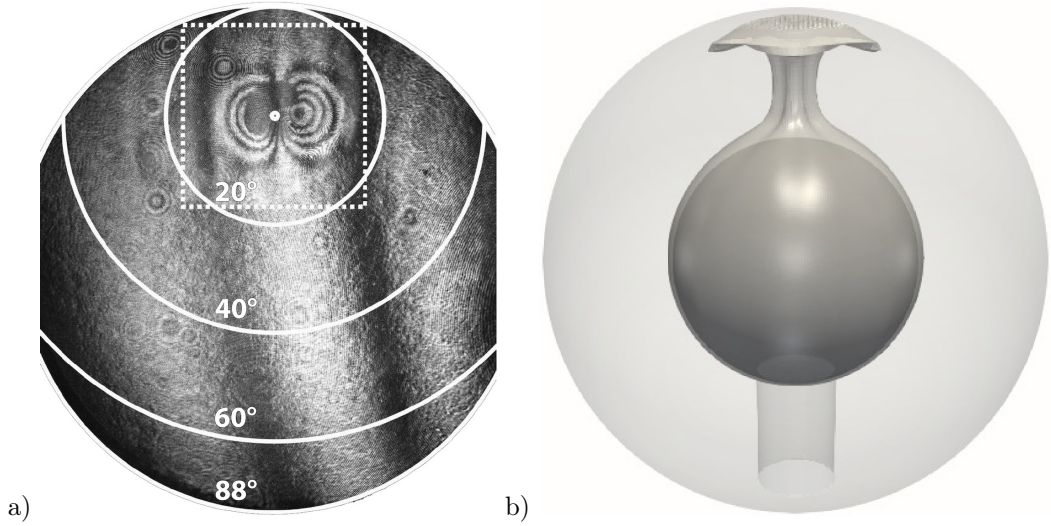


Figure 7: a) typical interferogram conducted under Earth's conditions (Sitte [80]). The image shows a 'double ring' structure at the North Pole for a thermal convection experiment at $L=3.5 \cdot 10^6$ and $Pr=35$. The degrees from $20^\circ - 88^\circ$ visualize various opening angles for the camera. b) in order to interpret the pattern, a numerical simulation at the same Rayleigh number was performed. The temperature iso-surface reveals a rising, convective plume. As presented in this section, this plume can be uniquely assigned to the ring structure in the interferogram. The cylindric structure in the South Pole is the shaft surrounding the rotation spindle and the thermal circuits.

point of this reconstruction is the comparison. Generic interferograms of thermal plumes or laminar sheets have to be known. However, they are achieved with e.g. ground based experiments, numerical simulations or generic analytic functions. Experimental investigations have been carried out by Sitte [80], Egbers et al. [18] and Larcher et al. [52]. These experiments were conducted under the influence of the gravitational force field of the Earth. The results of these experiments are very useful, since they show comparable thermal structures as in the μg case. However, the Earth' gravitational field limits the number of different convective structures. A typical interferogram performed by a ground based experiment is depicted in Fig. 7a. The central plume at the North Pole exhibits in a concentric fringe structure which is found to be a thermal plume in the numerical simulations, (Fig. 7b). However, analytic functions are needed to verify the assumption, that plumes exhibit as interferometric double ring structures.

Generic convective structures and their interferograms

As shown in Immohr [43], interferograms of convective flows show two typical structures: a) plume-like up- and down-welling regions are characterized by double ring structures, b) sheet-like up- and down-welling regions exhibit in stripes. Both generic structures can be generated using a one dimensional temperature profile given by the spline $h : \mathbb{R}_{\geq 0} \rightarrow \mathbb{R}_{\geq 0}$ with

$$h(u) := \frac{1}{4} \begin{cases} (2-u)^3 - 4(1-u)^3 & \text{for } u \leq 1, \\ (2-u)^3 & \text{for } 1 < u \leq 2, \\ 0 & \text{for } 2 < u. \end{cases}$$

The two-dimensional plume-like temperature field H_P is obtained by rotating this cubic spline around the vertical coordinate axis, i.e.,

$$H_P(x, y) := h(x^2 + y^2),$$

and the corresponding sheet-like temperature field H_S by shifting the profile orthogonal to the x-axis, i.e.,

$$H_S(x, y) := h(|x|).$$

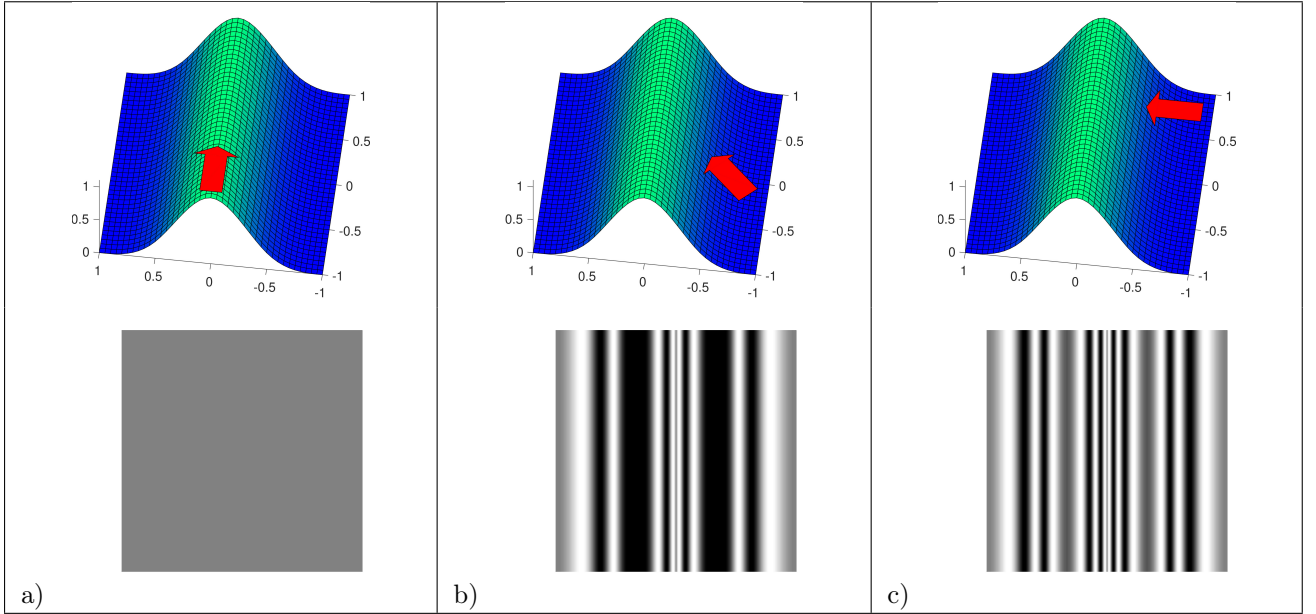


Table 2: a) generic sheet-like temperature field H_S (upper row) and corresponding artificial interferogram (lower row). The polarization direction is depicted by the red arrow. Constant regions along the polarization direction generate constant intensities. b)-c) rotating the polarization plane exhibits characteristic stripes where the finest stripes are found, when the polarization direction is orthogonal with respect to the maximum of the gradient.

Both temperature profiles are depicted in Table 2 and Table 3, respectively.

The calculation of artificial interferograms can be carried out by using oscillating functions where steep gradients result in high frequencies and flat gradients in low frequencies. Trigonometric functions are suitable for this task, as the density can be adjusted by a multiplication factor α_{fringe} with the frequency. The cosine was tested, as this function is smooth and simple to handle. The ability of generating fringes is given by the following example: $\cos(2x)$ with $\alpha_{\text{fringe}} = 2$ is higher frequent and hence produces more fringes as $\cos(x)$ with $\alpha_{\text{fringe}} = 1$. The artificial interferogram $I(\mathbf{x}) \in [-1, 1]$, with $\mathbf{x} = (x, y)$, is finally obtained by the directional derivative of the radially averaged temperature field T_{mean} along the polarization vector \mathbf{s} ,

$$I(\mathbf{x}) = \cos \left(a_{\text{fringe}} \cdot \frac{\partial T_{\text{mean}}(\mathbf{x})}{\partial \mathbf{s}} \right). \quad (22)$$

In practice, this derivative is approximated by a finite difference. The multiplication factor ranges between $1 < a_{\text{fringe}} < 50$ and has to be determined individually for the given numerical temperature field. The choice of taking the cos-function is a compromise on the comparability to the experimental interferograms and the sensibility due to derivatives. The vector \mathbf{s} is defined by the plane of polarization, the optical path and the surface shape. This has to be set individually, too. The calculation of artificial interferograms in spherical geometry follows basically the same approach and is demonstrated in Table 4. First, the temperature field (Table 4a) is integrated and weighted radially. It is recommended to interpolate the simulation data onto a finer grid, as the numerical derivative gets smoother, (Table 4b). Afterwards, the resulting planar function is derived in direction of \mathbf{s} (Table 4c). Finally, the cosine is applied which yields the interferogram (Table 4d). The density of stripes is adjusted by varying the pre-factor which is set to $a_{\text{fringe}} = 12$ in most calculations.

3.3 Recognition

It was shown in Section 3.2 that sheet-like temperature fields correspond to stripes in the interferogram and plume-like temperature fields to double ring structures. The question arises how these two structures are automatically recognized in images. This section presents the mathematical background to answer this. For ease of presentation the image processing pipeline (Fig. 8) will guide the reader from the input image and input

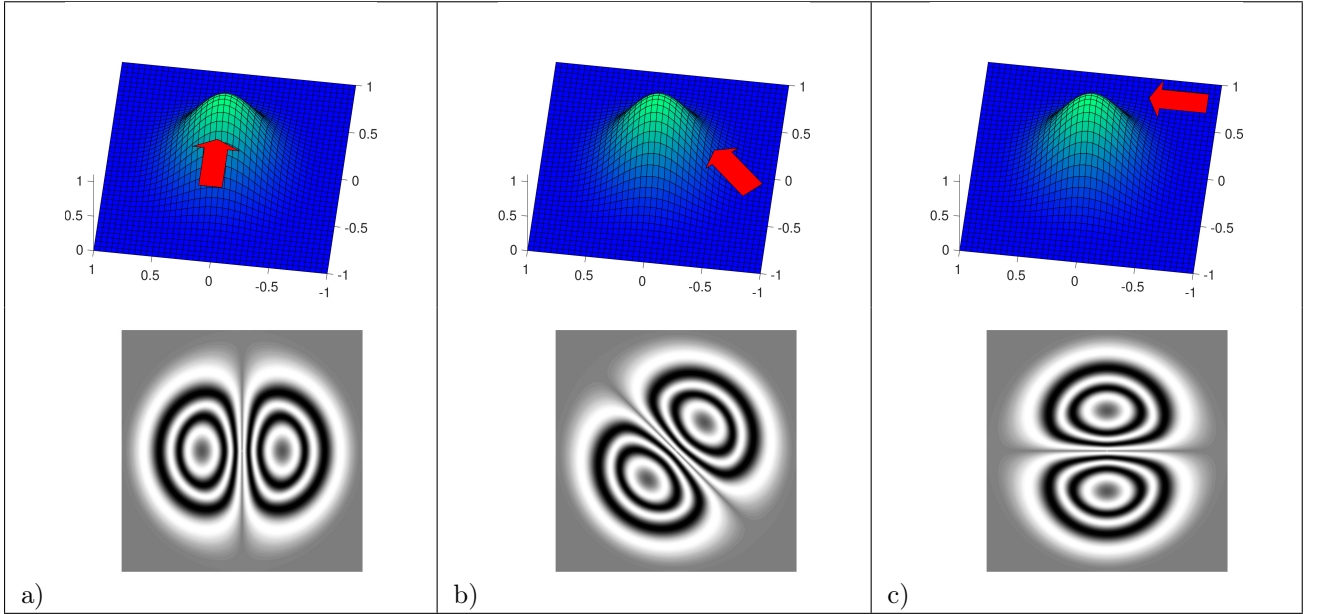


Table 3: a) generic plume-like temperature field H_P (upper row) and corresponding artificial interferogram (lower row). The polarization direction is depicted by the red arrow. b)-c) the rotation of the polarization plane by 45° and 90° changes the orientation of the interferogram accordingly.

parameters to the output.

Image pipeline

Image primitives such as corners, edges or texture elements may be detected by convolving the image $I(\mathbf{x})$ with $\mathbf{x} = (x_1, x_2)$ and appropriate filter masks. A related low-level vision representation which is closer to our stripes and double ring structures is expanded by Bigun [3]. In image processing it is good practice to start the image processing pipeline with 2D convolutions which modify the spatial frequency characteristics by weighting each pixel within a well defined window. Such convolutions are commonly used to sharpen or blur the image, or – as in our case – to prepare the image for detecting stripes. However, one looks for small filter masks (e.g. smaller than 15×15 pixels), so that the convolution can be efficiently computed in the local space. As a linear operation a convolution secures stability in terms of “Small changes of the filter do not lead to large changes in the output image”. A binary threshold is an example for a nonlinear filter introducing instability — a small change of the threshold can yield a drastic change of the output image. For this reason binary operations are applied at the end of image processing pipelines after corners, edges, or textures have been identified using the gray value and neighborhood respecting convolutions.

The following recognition process is described by means of the image processing pipeline as depicted in Fig. 8. Roman numerals in the text refer to processes which are labeled with a diamond symbol. The pipeline is used to abstract the stripe regions of image Table 5c and the double ring regions of image Table 5d. However, the same pipeline is applied on both structures. The ‘magic’ for the feature detection (stripes versus double rings) lies in the second 2D convolution M_W , and M_I , (I). Here, M_W denotes the structure adapted filter mask for double eye structures which is defined in [111] Eq. (7). M_I denotes the structure adapted filter mask for stripes which is defined in [111] Eq. (11). This gives the complex valued image $I_{20}(\mathbf{x})$ quantifying the occurrence of stripes or double rings, (II). I_{20} can be interpreted via the polar form, where the angle gives a direction and the magnitude the brightness of a pattern. Table 5e and Table 5f display the original interferogram overlaid with the color-coded feature indicator I_{20} , (III). The representation of I_{20} may be used for a first inspection of the feature detection, the tuning of the Gaussian interpolation with σ_I and of the window size with σ_W . The stripes light up in blue (Table 5e) whereas the centers of the double rings light up in magenta (Table 5f).

As the color corresponds to the argument $\arg(I_{20})$, the colored regions can be dissected by projecting the complex number I_{20} onto the unit vector $(\cos \alpha, \sin \alpha)^T$, $-\pi \leq \alpha \leq \pi$, where α denotes the color or angle of

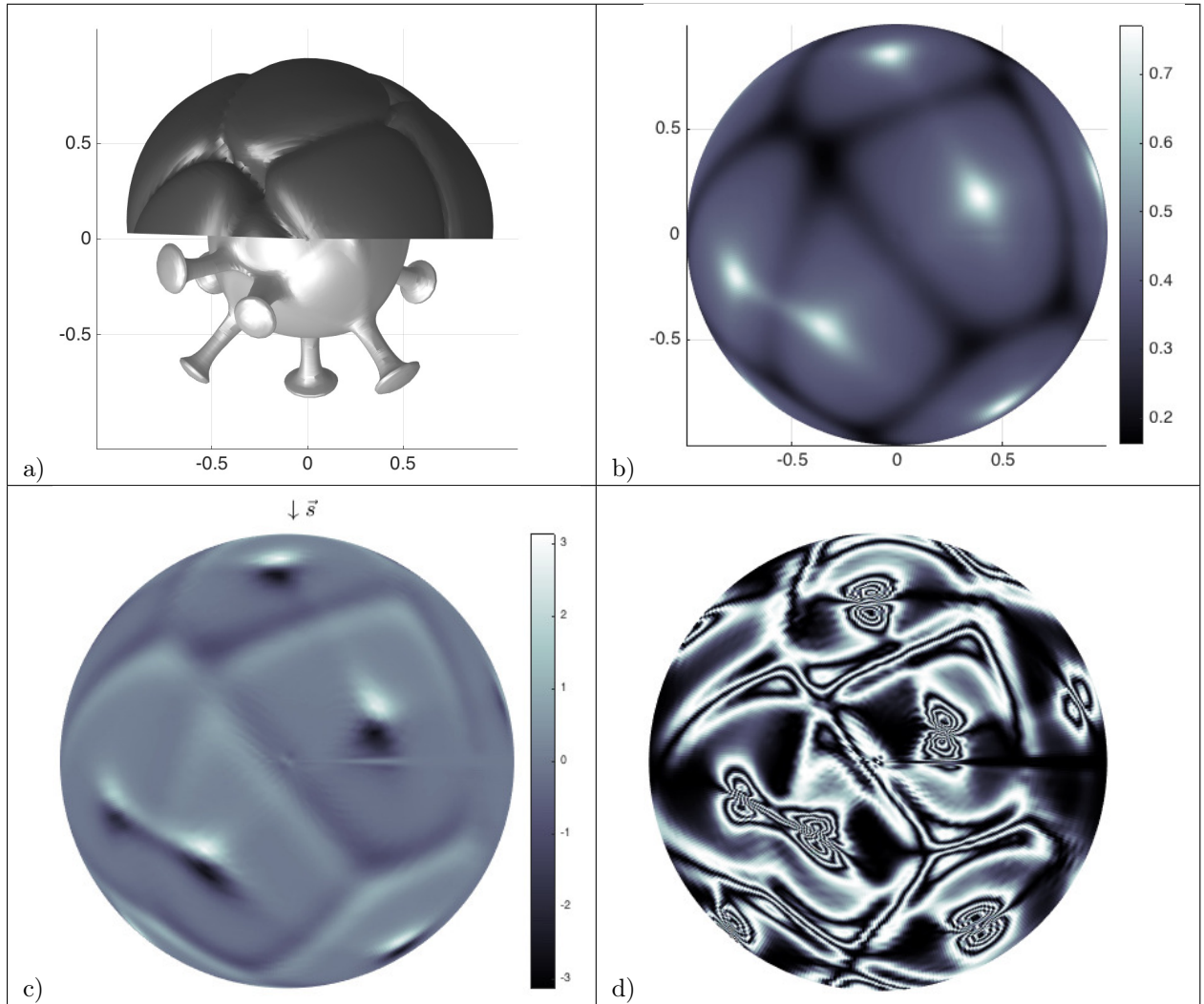


Table 4: a) numerical simulation of an unsteady convective flow in the spherical shell with $Pr=125$, $L=3 \cdot 10^4$ and a viscosity contrast of $\gamma = 32$. The upper hemisphere shows cold down-wellings, colored dark gray. Hot rising plumes are visible in the lower hemisphere as light gray spikes. b) radially averaged temperature field T_{mean} . Hot plumes appear as bright spots, cold down-wellings as black lines. c) the first derivative of the averaged temperature field in direction \mathbf{s} of the polarization plane. d) artificial interferogram. The frequency of the black-white alterations correspond to the first derivative of the mean temperature field. Plumes correspond to double-ring structures, sheets to stripes.

interest, (IV). The white regions of Table 5g and Table 5h are obtained by a binary threshold of the result with using the value t . So, the visual inspection of the color-coded representation of I_{20} allows for the tuning of the input parameters α and t to reach a binarized highlighting of the structures of interest, (V). In summary, the color gives the direction of the structure and the brightness the intensity of the pattern. This binarization may be processed further, (VI). In case of the double rings, the centroids of the whitely presented foreground regions correspond well with the centers of the rings, (VII,VIII).

Double ring structures and stripes are often found in interferograms of the GeoFlow experiment. To identify them successfully with the presented algorithm an analytic expression of the patterns is needed. Harmonic function can be used for this purpose. The iso-curves of $f(z) = z^{-1}$ (see Table 5b) show strong similarities with ring structures found in interferograms. Stripes are found with the harmonic function $f(z) = z$, see Table 5a.

3.4 Tracking

Besides recognition, the tracking of the convective structures is one of the aims of this study. This allows the calculation of drift velocities or the identification of the local coordinate system. This task can be carried out with little effort, if a) the acquisition frame rate is high with respect to the fluid velocity, and if b) the convective structures are stable in their shape. The frame rate of the experiment is fixed to two values, namely 0.048 Hz (long term runs) and 10 Hz (short term runs), but only the latter case is suitable for tracking. The plume tracking algorithm starts with the pre-calculated centers $(x(t), y(t))$ of convective plumes which are saved for each image and each time step in an external array. Based on this sequence the paths of convective structures can be extracted. However, this is somewhat superficial, since convective processes underlie merging, vanishing or formation. The plumes are captured and labeled individually, but it is difficult to identify segregated paths. To overcome this problem the neighborhood of each plume was analyzed and a probability radius R was defined, where the plume will most likely appear in the next image. This radius depends on the rotation rate, on the imaging frame rate and on the velocity of the convective structure. For testing purposes stationary cells with an angle velocity of $\omega=1.4$ mm/s were used. The radius is set to a maximum of $R=6$ px, keeping in mind that the slow rotation moves a stationary plume with about 1 px per frame. The curvature of the sphere does not play a significant role here, since the laser beam enters the fluid filled test section of GeoFlow orthogonally with respect to the surface of the shells. This value is obtained from a full rotation with 1250 images and a resolution of 992×992 pixels. The unique tracking of each plume is ensured by introducing the Euclidean norm of the transport vector $\mathbf{v}_t = (x_{i+1} - x_i, y_{i+1} - y_i)$ and fulfilling the inequality,

$$\|\mathbf{v}_t\|_2 < R. \quad (23)$$

The transport vector v_t measures the spatial change of the plume location over two images. This method calculates connected paths for segregated plumes as shown in Fig. 9 (left). The tracking has been applied on the low resolution images of the GeoFlow IIc, too, where connected path could be extracted by adjusting the radius R . This is mentioned here because the successful low resolution test was mandatory for the start of the campaign. Several applications can be deduced from this type of recognition and tracking, e.g. the calculation of fluid velocities, the measurement of merging time scales or the determination of invariants such as the unknown coordinates of the North Pole.

3.5 Identification of reference points

The calibration of the camera is used to quantify the geometrical and optical properties which affect the imaging process. This is essential for the reconstruction of the world model, in our case the flow velocities. Commonly, well defined checkerboard patterns are used to auto-calibrate a camera. This option is not available at the ODM. However, the camera properties can be reconstructed with reference points, too. The GeoFlow experiment rotates slowly which reduces the number of markers required. Only the North Pole is a fixed point in the experiment and the interferogram. The pole is the piercing point of the rotational axis which intersects

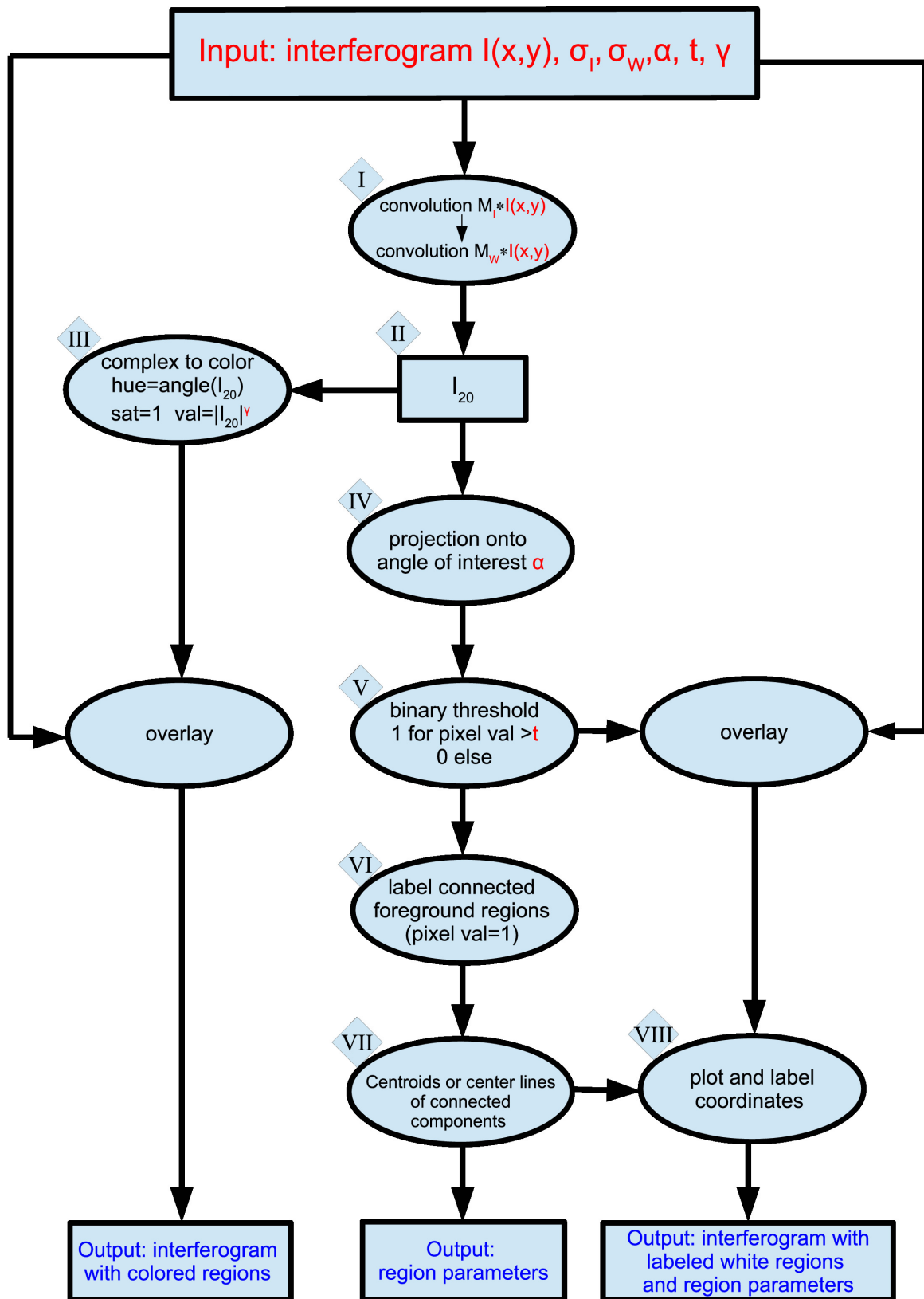


Figure 8: Image processing pipeline for stripe and double ring detection.

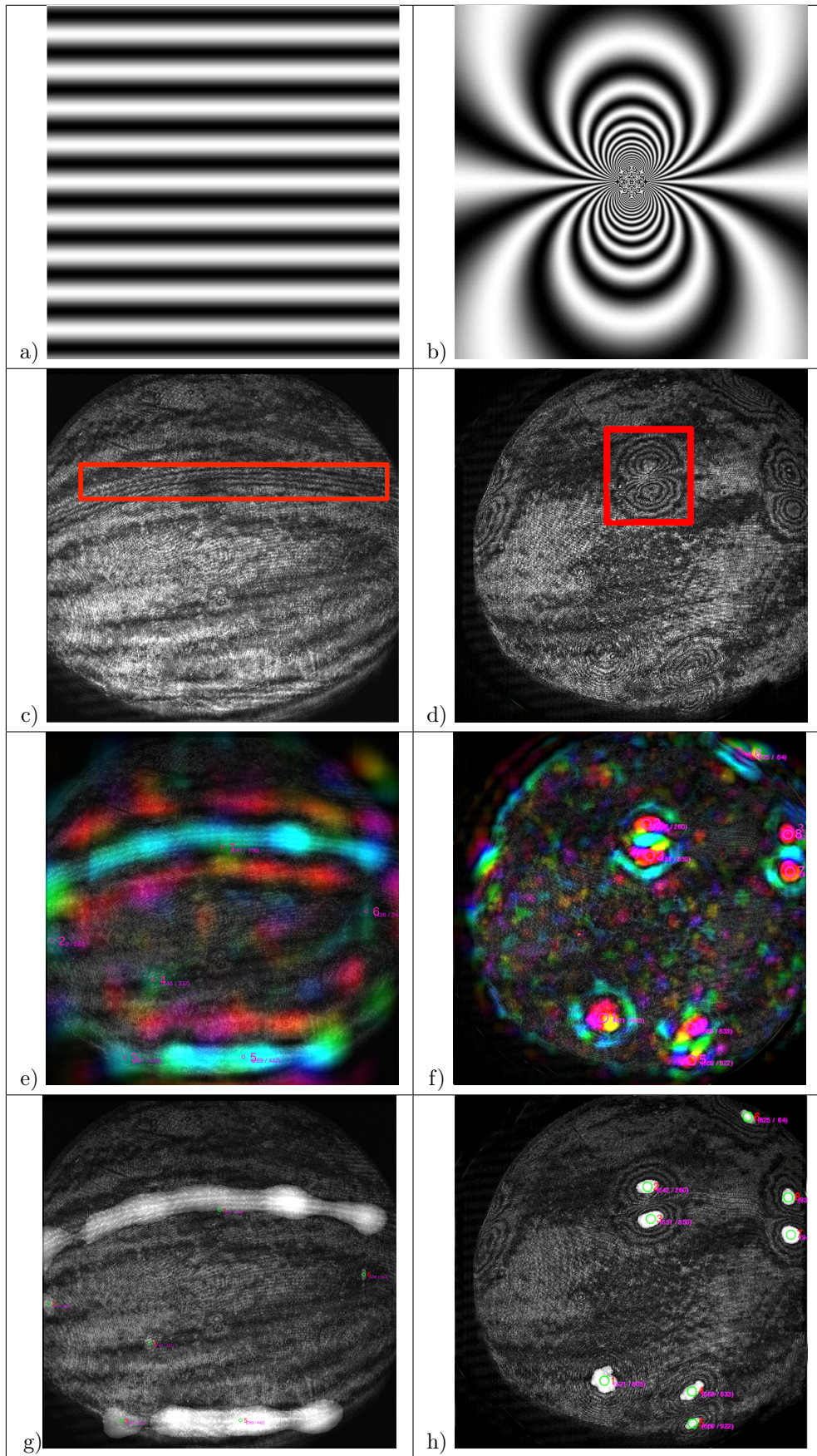


Table 5: Recognition algorithm to detect patterns in interferograms. The first row shows the target patterns of (a) stripes and (b) double ring structures. These generic patterns are found in interferograms as (c) sheet-like and (d) plume-like flows. The complex valued tensor entry I_{20} marks best fits (blue) between the original function and the image, as shown in (e) and (f). Local maxima of I_{20} (colored in white) correspond to (g) regions of laminar flows and (h) thermal plume centers.

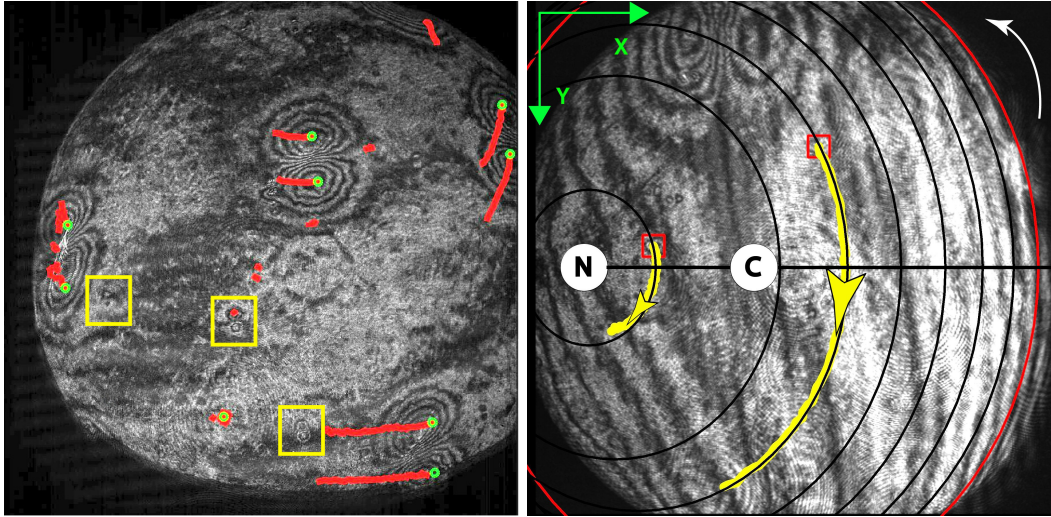


Figure 9: (left) tracked paths of automatically identified stationary plumes with a rotation rate of 0.008 Hz. Green dots mark the centers of plumes and the red dots show the covered distance. Yellow squares show stationary dust particles. (right) co-linearity between actual paths of different located dust particles and the corresponding latitudinal lines. (N): location of the North Pole. (C): location of the center point.

with the optical axis. As already mentioned, the visualization of the GeoFlow experiment is limited to the northern hemisphere. Therefore, the South Pole cannot be captured and does not contribute to the calibration process. The coordinates of the North Pole are deduced from closed elliptical tracks. Each plume creates two ellipse-shaped curves which comes from the fact that one single plume appears as double-ring structure with two centers. The tracks form shifted, overlaying curves, where the common center of the structures gives the desired coordinates of the North Pole. Two pole-surrounding ellipses as well as the calculated coordinates (colored in yellow) are shown in Fig. 10a. A second way of locating the north pole is utilizing stationary equatorial plumes. These plumes appear as elliptical curves too, but these are not closed (Fig. 9 (left) and Fig. 10b). The area bounded by the perpendicular bisectors (yellow lines) approximates the coordinates of the North Pole and are within the uncertainty margin of the coordinates found by the tracking method.

Other markers may be obtained by fixed dust particles in the experimental gap (see yellow squares in Fig. 9 (left)). Some of them stick at the shell and move with the rotational velocity. They become noticeable as tiny double ring patterns, which lie on perfect ellipses. However, they have to be tracked manually, as they are too tiny to be recognized automatically by our algorithm. The optical distortion of the interferograms is another source of coordinates. By comparing the bond seam of the outer sphere with the image of the seam in the interferograms, it is possible to obtain enough coordinates for the exact calibration of the camera. This task is planned for future work. Paths of numerous dust particles are used to identify the North Pole, the center point, the radius and the local coordinate system. Fig. 9 (right) shows a GeoFlow interferogram with reconstructed latitudinal lines.

3.6 Numerical simulations

The governing equations (Eqs. 3-6) are studied using two methods: a) a linear stability analysis which provides the critical electric Rayleigh numbers L_c and threshold values of the convective onset and b) three-dimensional large eddy simulations (LES) and interferograms calculated with the software package OpenFoam. The numerical simulations provide the temperature and electric field for the statistical evaluation which are compared with interferograms.

Pseudo-spectral code

For the linear stability analysis, a spectral numerical method is used to solve the dimensionless governing equations. This method is based in the pseudo-spectral code presented in [41]. Here, the velocity field is

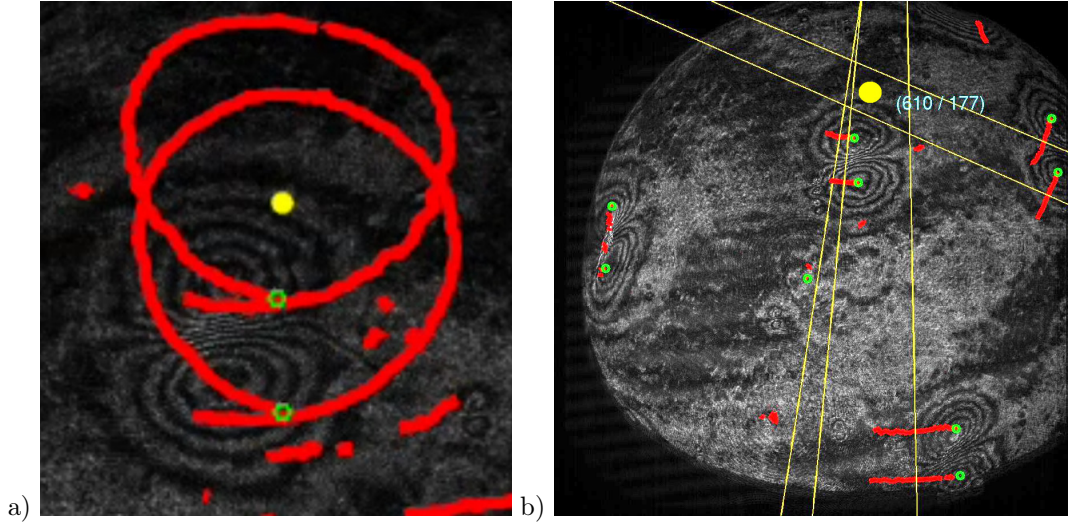


Figure 10: a) elliptical track of a stationary plume in the northern polar region. The piercing point of the rotation axis (yellow point) is found by weighting the centers of the ellipses. b) localization of the North Pole via the secant method where equatorial plumes are tracked. Both methods yield the same result.

decomposed into poloidal and toroidal potentials ψ_1 and ψ_2 ,

$$\mathbf{u} = \nabla \times \nabla \times (\psi_1 \mathbf{e}_r) + \nabla \times (\psi_2 \mathbf{e}_r), \quad (24)$$

obeying the continuity equation. By using the pseudo-spectral method and applying $\nabla \times \nabla \times$ and $\nabla \times$ to Eq. 14 (which separates the potentials), one can solve the hydrodynamic equations with a high accuracy in the spherical geometry. This results in a fourth-order equation for the potential ψ_1 and a second-order equation for the potential ψ_2 . The critical electric Rayleigh numbers, L_c , are calculated using linearized equations [87]. The corresponding eigenvalue problem is solved by direct numerical integration, where the spectrum is analyzed for growth rates $\sigma = 0$.

OpenFoam

For the three-dimensional numerical simulations an incompressible, 2nd order finite volume, transient buoyancy solver of OpenFoam 4.1 is used which is expanded to include the non-uniform electric field. The governing equations are solved in the rotating reference frame. In addition, the solver includes the source terms for the dielectric heating, H , in the temperature equations and the volumetric body force, F_{DEP} , in momentum equation.

The boundary condition for velocity is no-slip and Dirichlet for temperature. To mimic the GeoFlow experiment in all aspects, the experimental time scales are set consistent with Zaussinger et al. [114]. This included the heating-up periods and the idle periods between each EP. The electric field is defined as a negative gradient of the electric potential and is calculated via the Gauss equation, $\nabla \cdot (\epsilon \nabla \Phi) = 0$, by taking the electrical fluctuations and thermo-electric feedback effect into account. The boundary condition of the electric potential is set at the outer shell with $\Phi = V_{rms}$ and $\Phi = 0 V$ at the inner shell.

The mesh of the spherical gap is generated by radially extruding a spherical 2D surface grid to honeycomb shaped cells in 3D. The OpenFoam 'Pimple' algorithm solves subsequently the LES model with top-hat filtered versions of the governing equations. The filter width is the cube root volume of each cell. VanDriest damping in distance to the boundary layer ensures that the 'dynamic k' turbulence model is applied only in the bulk flow.

Antares

The ANTARES (A Numerical Tool for Astrophysical RESearch) code is designed to numerically solve the fluid dynamical equations as presented in Sec. 2.1. Among several options it can do so on an equidistant, three dimensional rectangular grid. It can perform compressible and incompressible hydrodynamic simulations with EHD in all three spacial dimensions. The source code is written in Fortran90 and parallelized in a hybrid way with MPI and openMP, [49, 50, 106, 105]. The governing equations are treated by the finite volume and conservative finite difference method, where order of spatial and temporal discretization can be chosen arbitrarily. However, a 5th order weighted essentially non-oscillatory scheme (WENO5) is favored for the mentioned type of simulations. For the compressible formulation, this scheme calculates the boundary fluxes for each time step of the characteristic variables in their eigenspace and hence guarantees stable up-winding. In the incompressible formulation, such as presented in this manuscript, the scheme calculates the boundary fluxes in real space.

The dielectrophoretic force as well as the dissipation rate term are treated explicitly. This is valid, as both terms are ‘slow’ compared to other components of the equations. Furthermore, the electric field is set constant. Preliminary numerical simulations prove the concept. Fig. 11 depicts a convective flow in a the plane capacitor with height of 1cm, a temperature difference of $\Delta T = 3 K$ and voltage $V_0 = 2800 V$ for 1-Nonanol. Potential lines of the electric field are highlighted in white. The simulation represents a case under micro-gravity conditions. The investigation of EHD in the plane capacitor has recently started and will be the focus of near future work.

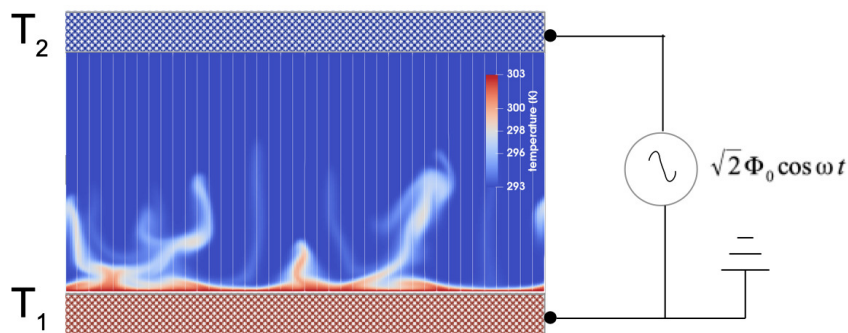


Figure 11: Sketch of the EHD convection cell for the plane capacitor with periodic vertical boundary conditions. Depicted value is the temperature, vertical lines are potential lines of the electric field. The simulation is based on the Boussinesq approximation for $L = 1.9 \times 10^4$ without dielectric heating.

3.7 Statistical evaluation

The fluid flow is statistically evaluated by using the properties of the probability distribution function of the random real-valued temperature variable T . The temperature field is averaged over shells (θ, ϕ) of equidistant radii for 30 snapshots providing 300 seconds of simulation time of the fully developed flow. Hence, the calculated profiles of the first four statistical moments are functions of the radius.

Turbulence and intermittency lead to rare, but intense peaks in the temperature field. As a result, in such intermittent systems especially the higher order moments depart significantly from the Gaussian distribution. In particular, the evaluation of the third and the fourth statistical moments provide information of rarely occurring events. For convective processes these events are commonly related to thermal plumes. In the following, the spatial mean is calculated for each shell at radius r and for all angles θ and ϕ . The time mean covers 30 consecutive numerical snapshots between $t = [t_1, t_2]$, where the kinetic energy converges towards a constant value or is oscillating. The spatial shell mean of a variable $X(r, \theta, \phi, t)$ is defined through,

$$\langle X \rangle_h := \sum_{\theta, \phi} \frac{1}{N} X(r, \theta, \phi, t)$$

with N being the number of data points in the spherical shell for radius r and for fixed time t . The temporal mean is defined through,

$$\langle X \rangle_t := \sum_{t=t_1}^{t_2} \frac{1}{30} X(r, \theta, \phi, t).$$

for varying r , θ and ϕ . The first statistical moment used in this manuscript is the convolution of the shell and time averaged mean value defined as,

$$\langle X \rangle := \langle X \rangle_{h,t} = \sum_{t=t_1}^{t_2} \frac{1}{30} \left(\frac{1}{N} \sum_{\theta, \phi} X(r, \theta, \phi, t) \right),$$

The mean $\langle X \rangle$ defined here is consequently a function of the radius r alone. Higher statistical moments are defined through,

$$\langle X'^n \rangle := \langle (X - \langle X \rangle_h(r))^n \rangle_t.$$

The second statistical moment is the variance defined as $\langle X'^2 \rangle$, which describes fluctuations. A thermal asymmetry of the temperature distribution around the mean value $\langle T \rangle$ is parametrized by the skewness $\langle S \rangle = \langle T'^3 \rangle / (\langle T'^2 \rangle)^{3/2}$. Large positive values of S characterize locally higher values of T which cover a smaller surface area. Hence, the values deviate further from the mean value than locally lower values. The same holds for large negative values of S for cold areas embedded in a hot surrounding, [50]. In particular, for $S > 0$ the fluid flow is dominated by strong uprising thermals and for $S < 0$ by strong downdrafts, respectively. Intermittency is evaluated by the thermal kurtosis (flatness) $\langle K \rangle = \langle T'^4 \rangle / (\langle T'^2 \rangle)^2$. The kurtosis provides a scale of a certain 'tailedness' and describes rarely occurring and very spiky events in intermittent systems, [75]. For the present study, high values of the kurtosis indicate localized regions with plumes of large magnitude, and large areas with slow ascending and descending flow. However, the direction of the fluid flow in the plumes is given by the sign of the skewness. The higher statistical moments are very sensitive to rare events and consequently of a high interest.

Published and presented in:

- F. Zaussinger and H. C. Spruit. Semiconvection: numerical simulations. *Astronomy and Astrophysics*, 554: A119, 2013. doi: 10.1051/0004-6361/201220573. URL <http://dx.doi.org/10.1051/0004-6361/201220573>
- B. Futterer, A. Krebs, A.-C. Plesa, F. Zaussinger, R. Hollerbach, D. Breuer, and C. Egbers. Sheet-like and plume-like thermal flow in a spherical convection experiment performed under microgravity. *Journal of Fluid Mechanics*, 735:647–683, 2013. doi: 10.1017/jfm.2013.507
- F. Kupka, M. Losch, F. Zaussinger, and T. Zweigle. Semi-convection in the ocean and in stars: A multi-scale analysis. *Meteorologische Zeitschrift*, 24(3):343–358, 2015. doi: 10.1127/metz/2015/0643
- F. Kupka, F. Zaussinger, and M. H. Montgomery. Mixing and overshooting in surface convection zones of DA white dwarfs: First results from ANTARES. *Monthly Notices of the Royal Astronomical Society*, 474(4): 4660–4671, 2018. doi: 10.1093/mnras/stx3119
- F. Zaussinger, A. Krebs, V. Travnikov, and C. Egbers. Recognition and tracking of convective flow patterns using Wollaston shearing interferometry. *Advances in Space Research*, 60(6):1327 – 1344, 2017. ISSN 0273-1177. doi: <https://doi.org/10.1016/j.asr.2017.06.028>. URL <http://www.sciencedirect.com/science/article/pii/S0273117717304544>
- F. Zaussinger, C. Egbers, A. Krebs, and V. Travnikov. New results of the spherical convection experiment Geoflow IIc. In *EGU General Assembly Conference Abstracts*, volume 19 of *EGU General Assembly Conference Abstracts*, page 7801, Apr. 2017. URL <https://meetingorganizer.copernicus.org/EGU2017/EGU2017-7801.pdf>
- V. Travnikov, F. Zaussinger, P. Beltrame, and C. Egbers. Influence of the temperature-dependent viscosity on convective flow in the radial force field. *Phys. Rev. E*, 96:023108, Aug 2017. doi: 10.1103/PhysRevE.96.023108. URL <https://link.aps.org/doi/10.1103/PhysRevE.96.023108>
- F. Zaussinger, P. Haun, M. Neben, T. Seelig, V. Travnikov, C. Egbers, H. Yoshikawa, and I. Mutabazi. Dielectrically driven convection in spherical gap geometry. *Phys. Rev. Fluids*, 3:093501, Sep 2018. doi: 10.1103/PhysRevFluids.3.093501. URL <https://link.aps.org/doi/10.1103/PhysRevFluids.3.093501>
- F. Zaussinger and F. Kupka. Layer formation in double-diffusive convection over resting and moving heated plates. *Theoretical and Computational Fluid Dynamics*, 33(3):383–409, 2019. doi: 10.1007/s00162-019-00499-7. URL <https://doi.org/10.1007/s00162-019-00499-7>
- F. Zaussinger, P. Haun, P. Szabo, V. Travnikov, M. Al Kawwas, and C. Egbers. Rotating spherical gap convection in the GeoFlow International Space Station (ISS) experiment. *Phys. Rev. Fluids*, 5:063502, Jun 2020. doi: 10.1103/PhysRevFluids.5.063502. URL <https://link.aps.org/doi/10.1103/PhysRevFluids.5.063502>

4 Non-rotating convection

The non-rotating case of convection in the spherical shell represents a generic type of fluid flow and has no geophysical or astrophysical counterpart. However, it is of great importance to test numerical models and stability analysis. Hereby, the basic flow states will be analyzed in detail and the influence of the electric field on the dielectric working fluid can be investigated under varying gravity conditions. In the following, theoretical values of the onset of convection are compared with experimental data.

4.1 Onset of convection

Fig. 12 shows interferograms of the non-rotating case with $\Delta T = 0$ K, $\Delta T = 0.4$ K and increasing voltages. The corresponding Rayleigh-Roberts number is used here for cases with $\Delta T = 0$ K (see [89] and comments after Eq. 18)

$$Ra_H = \frac{2\epsilon_0\epsilon_r e T_0 V_{rms}^2}{\rho\nu\kappa} \quad (25)$$

Fig. 12 (top row) shows interferograms with $Ra_H = 8.4 \times 10^5$ for $V_{rms} = 1272$, $Ra_H = 2.3 \times 10^6$ for $V_{rms} = 2121$ and $Ra_H = 4.6 \times 10^5$ for $V_{rms} = 2969$. The critical value of $Ra_{H,cL} = 1.6 \times 10^6$ corresponds to $V_{rms} = 1754$ V. hence, the onset is found in between Fig. 12 a) and b). Fig. 12 b) shows a clear distortion from the base pattern, which changes to a convective plume for higher voltage, cf Fig. 12 (c). Accompanying numerical simulations [114] confirm convective cells for $V_{rms} = 2121$ V. The presented voltages are chosen according the GeoFlow experiment.

For cases with $\Delta T > 0$ K the electric Rayleigh number L is used again. In case of $\Delta T = 0.4$ K the onset is predicted at $L_c = 1511$, which corresponds to $V_{rms} = 1456$ V. The transition from the conductive state to the convective regime is depicted in Fig. 12 d) and e), which captures the onset by experimental points with $L = 1155$ and $L = 3208$, respectively. As in case of pure internal heating a convective plume is found for higher voltages. The theoretical onset of convection in case of $\Delta T = 3.0$ K at $V_{rms,crit} = 671$ V cannot be verified since the lowest voltage available in the experiment is $V_{rms} = 1272$ V. The interferograms shown in Fig. 12a and 12b depict slightly distorted yellow lines in the conductive state. These distortions are found in all conductive cases and may result from the optical diagnostics module or from the outer cooling loop.

Thermal profile of the conductive case for $\Delta T > 0$

It is assumed that the toroidal and poloidal components of $\mathbf{E}_1(r, \theta, \phi)$ in the conductive case have only small contributions to the initial electric field $\mathbf{E}_0(r)$. This justifies the assumption of a one-dimensional electric field $\mathbf{E}(r)$. The temperature equation Eq. 18 is solved analytically for a constant permittivity with the electric field presented in Eq. 12 and reads,

$$T(r) = -\frac{\eta}{1-\eta} + \frac{\eta}{(1-\eta)^2} \frac{1}{r} - \lambda \left(\frac{\eta}{(1-\eta)^2} - \frac{\eta(1+\eta)}{(1-\eta)^3} \frac{1}{r} + \frac{\eta^2}{(1-\eta)^4} \frac{1}{r^2} \right). \quad (26)$$

for $1 \leq r \leq 2$. This solution is the sum of the temperature profile in the absence of internal heating, $-\frac{\eta}{1-\eta} + \frac{\eta}{(1-\eta)^2} \frac{1}{r}$, and includes the dielectric heating parameter λ .

To investigate the base state of the experiment the conductive reference case of run 'C20' ($\lambda = 11$) of the GeoFlow experiment is studied. This includes a range of values for the heating parameter, λ , to study the transition state ($\lambda = 1$) where internal and external heating is balanced, where internal heating is absent ($\lambda = 0$), and the smallest achievable value of the GeoFlow experiment ($\lambda = 0.16$). The analytical solutions of the temperature fields are shown in Fig. 13a together with the 3D numerical simulation for $\lambda = 11$ indicated by red crosses which present good agreement with the corresponding analytic solution. In the case where $\lambda < 1$, the internal heating is negligible and convection is triggered by ΔT . However, for $\lambda > 1$, the temperature field reaches a maximum at the inner shell at $r_{max} = 4\lambda/(1+3\lambda)$. In this case, the stability of the system depends on the interaction of the signs of the dielectrophoretic acceleration that is influenced by the temperature gradient.

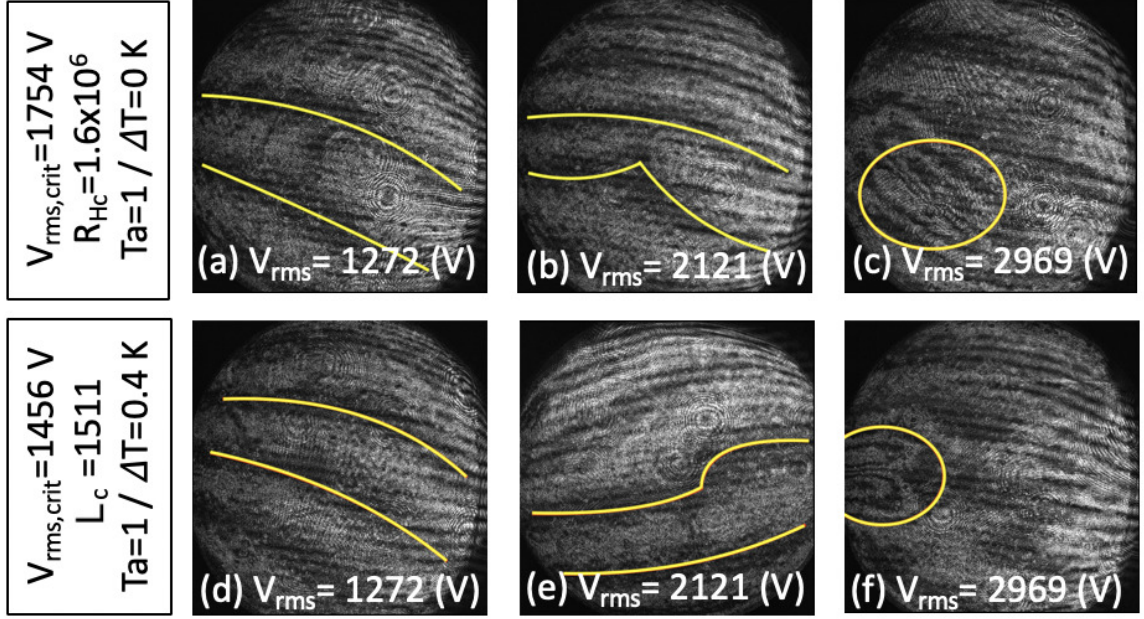


Figure 12: Experimental interferograms for the non-rotating case for $\Delta T = 0$ K (top row) and $\Delta T = 0.4$ K (bottom row). The onset of convection is found between a)-b) and d)-e), respectively. While conductive cases show only a base fringe pattern (a,b) the convectively unstable flows appear as butterfly patterns (c,f) for $V_{\text{rms}} = 2969$ V and as distorted fringe lines (b,e) for $V_{\text{rms}} = 2121$ V. Structures are highlighted in yellow to emphasize the thermal structure. Bended fringes in the conductive cases result from slightly misaligned optical elements in the Wollaston sharing interferometry unit of GeoFlow.

In the limiting case of $\lambda \gg 1$, the temperature converged to the maximum at approximately $r_{\text{max}} = 4/3$. Nonetheless, for $\lambda \leq 1$, the maximum is always found at the inner shell with $r_{\text{max}} = 1$ and radius ratio $\eta = 0.5$. In the absence of the centrifugal force ($\text{Fr} = 0$) the isothermal surfaces take the form of concentric spheroids with radially dependent temperature distributions.

Dielectrophoretic acceleration and buoyancy for $\Delta T > 0$

In the conductive case the electric field follows the solution of $\mathbf{E}_0 \sim r^{-2}$ (see Eq. 12) where \mathbf{E}_0 is independent of λ . However, the dielectrophoretic acceleration \mathbf{a}_e (obtained from Eq. 8) depends on λ and is strictly negative for $\lambda \leq 1$ (see Fig. 13b). The dielectrophoretic acceleration can be calculated by the analytic solution of the temperature by using the Oberbeck-Boussinesq approximation for the permittivity and the scaling relation $\beta = e \Delta T \epsilon_r$, the radial component of the dielectrophoretic acceleration is written as

$$a_e(r) = -\frac{1}{2} |\mathbf{E}_0|^2 \frac{d\epsilon}{dr} = -\frac{1}{2} \left(\frac{1}{\Gamma} \frac{1}{r^2} \right)^2 \beta \left(\frac{2}{r^2} + \lambda \left(\frac{6}{r^2} - \frac{8}{r^3} \right) \right) \quad (27)$$

for the GeoFlow case of $\eta = 0.5$. Fig. 13b depicts the radial component of the dielectrophoretic acceleration $a_e(r)$ for four different values of λ . For $a_e(r) < 0$, the sign of dielectrophoretic acceleration is negative and points radially inwards towards the center of the spherical gap. This generates an induced force field comparable to the gravitational force field. However, for $\lambda > 1$, the dielectrophoretic acceleration changes its sign at r_{max} (see [117]) and can separate the spherical gap into two layers. A deeper insight into the stability of the thermal stratification is given by the Brunt-Väisälä (BV) frequency written as

$$N^2 = -\frac{a_e}{T} \frac{dT}{dr}. \quad (28)$$

For the convective case, $L > L_c$, the fluid gets convectively unstable for $\lambda > 1$ and $N^2 < 0$, except at a region around the temperature maximum where $N^2 = 0$ indicating two convectively unstable layers separated

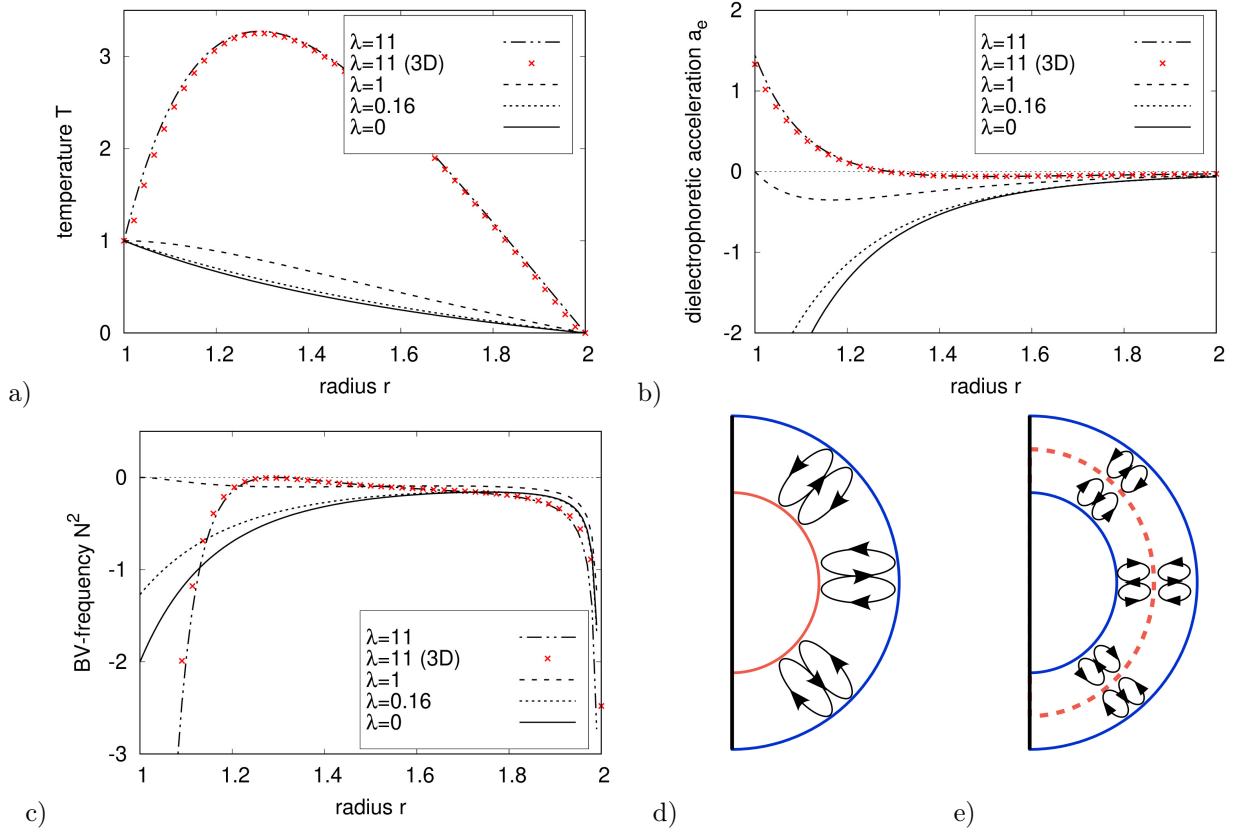


Figure 13: Analytic solutions for a) radial temperature distribution, b) dielectrophoretic acceleration and c) Brunt-Väisälä frequency for varying λ in conductive and non-rotating case for $\eta = 0.5$. Red crosses present solutions for a three-dimensional numerical simulation with $\lambda = 11$. Values for λ are chosen according the GeoFlow experiment. d) sketch of convection in the spherical gap geometry when $N^2 < 0$ in the complete gap and $\lambda < 1$). e) sketch of layered convection in the spherical gap geometry where $N^2 \geq 0$ at the middle of the gap and $N^2 < 0$ elsewhere with $\lambda > 1$.

by a stable conductive interface, see Fig. 13e. This theoretical separation has only been observed in numerical simulations in the plane capacitor (see [100]), but not in experiments. However, it could occur only as transient phenomenon. For $\lambda < 1$ the internal heating has only minor influence on the fluid flow and convection is similar to those observed in a RB cell, see Fig. 13d.

4.2 Thermal profile in the convective case

The comparison of experimental interferograms and the numerical results for different values of the voltage is shown in the Fig. 14. The first row depicts the experimental interferograms and the second row the numerical interferograms. The third and fourth rows show the temperature and velocity fields in a meridian plane.

The first column ($V_0 = 1800$ V) does not exhibit any convective structures for both reference temperatures. Three explanations would be possible: first, the interferometry is not sensitive enough to resolve weak temperature gradients; second, the experiment time scale is too short for convective flow to develop; third, the conduction state is stable at this voltage.

Convective plumes at $V_0 = 3000$ V show weak gradients and are hardly to identify in the interferograms. They are indicated by slightly distorted fringes. On the other hand, the plumes are visible in the numerical simulations and are organized in regular octahedral structures. These structures are also observed by Zaussinger et al. [111] and Feudel et al. [23]. For $V_0 \geq 4200$ V convective plumes are visible as double rings in the experiment and in the numerical simulations. The number of rings is positively correlated to the voltage and to the reference temperature. Due to the increased acceleration at higher voltages the thermal gradients steepen and the frequency of fringes in double-ring packages increases. This holds for both reference temperatures. It may be worth mentioning that sheet-like structures are never observed for equally thermalized boundaries $T_1 = T_2$. The mean diameter of convective plumes decreases with increasing the voltage. See, for instance, the results for $T_0 = 303.5$ K and $V_0 = 4200 - 6500$ V. The observed behavior of plumes is in good agreement with RB convection, where convective plumes are described as thermal boundary layers separated from walls. The boundary layers get thinner with increasing Rayleigh number. The thermal gradients then become steeper. In addition, the size of the plumes depends on the reference temperature. Plumes are larger for $T_0 = 293.0$ K. By comparing the temperature field (Fig. 14o) or the radial velocity field (Fig. 14t) observed at different temperatures, one finds steeper plumes at the higher temperature $T_0 = 303.5$ K, (presented in [114]).

The selected images are representative for the number of convective cells found in 3D simulations. They are obtained by manually counting. For both reference temperatures a positive correlation between plumes and voltage is found. Up to 20 plumes are found per hemisphere in case of $V_0 = 6500$ V. In the statistical mean there are 38% more convection cells in the numerical simulations than in the experiment.

The numerical simulations reveal that the convective plumes emerge irregularly in the spherical gap for $V_0 > 3000$ V. They are not stationary, but are moving and relocated within 10-20 minutes over the distance of the interferogram. As the experimental interferogram measurement lasts only three minutes, it is not possible to estimate the velocities of plumes for comparisons with the numerical results.

4.3 The velocity field

Interferograms do not deliver direct quantitative information about the velocity field. By careful confrontation of the experimental and numerical interferograms, however, it is possible to deduce some properties of the flow velocities. The simulations show that the convective flow is enhanced by the increase of the applied electric voltage, as expected from the analogy to the classical RB convection. Furthermore, the simulations show peak velocities at the locations of downdrafts, underneath double ring structures. The mean velocity in updraft regions is about halved. The last row in Fig. 14 shows this behavior. Blue regions, where the radial velocity points inwards, coincide with steep thermal plumes. This observation differs from earlier publications (eg. [28]) about GeoFlow II, where updrafts were predicted in the same situations.

The velocity field in such a downdraft region is shown in Fig. 15 in more details, where streamlines are superimposed on the velocity vectors. The colors of the vectors indicate the temperature values. One can see

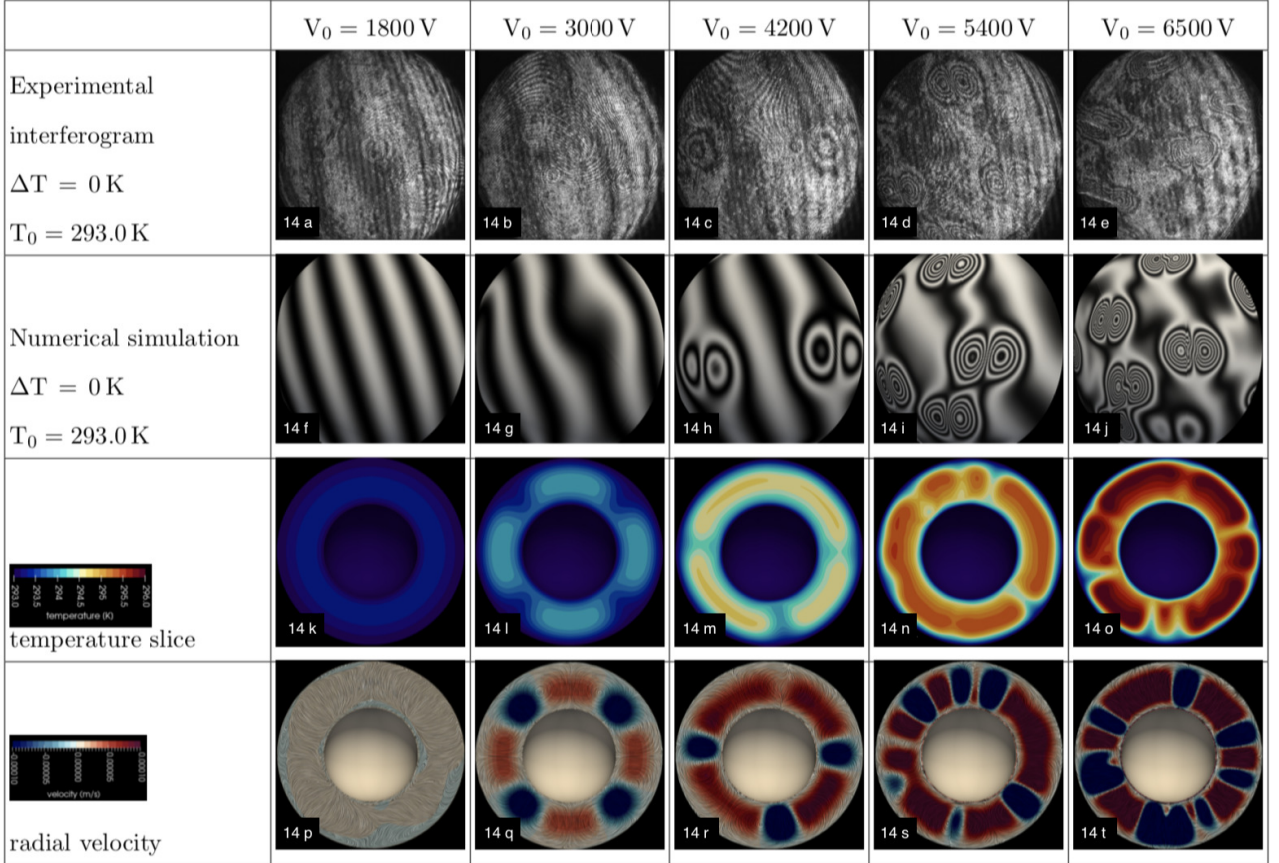


Figure 14: 14a-14e: experimental interferograms of the GeoFlow II experiment for $T_0 = 293.0 \text{ K}$ and $\Delta T = 0$. 14f-14j: numerically calculated interferograms based on 3D simulations. Both rows show interferograms recorded after $t = 2603 \text{ sec}$ which corresponds to the actual experimental time stamp. Dielectric heating is visible for $V_0 \geq 4200 \text{ V}$ as thermal plumes which exhibit in characteristic double-ring structures. Conductive cases (14a,f,k,p) show only the base fringe pattern. The third row depicts the temperature distribution in a vertical slice. The fourth row shows stream lines colored by the radial velocity field. Blue regions are downdrafts, red regions are updrafts.

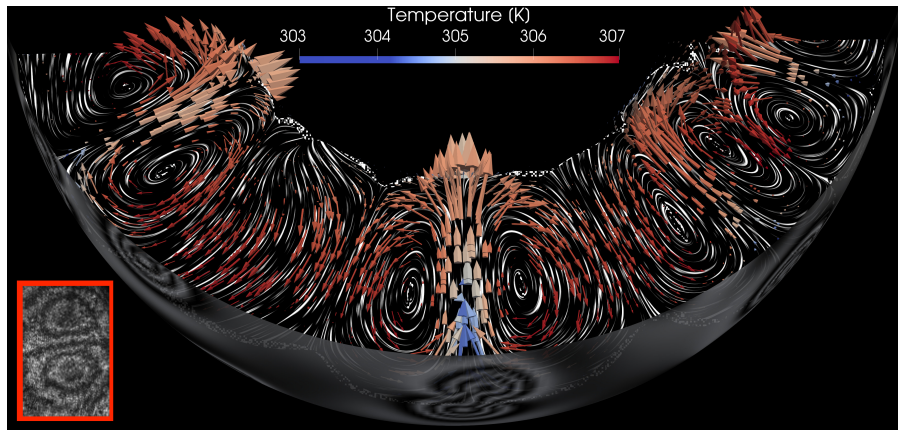


Figure 15: Velocity vectors and associated streamlines along a convective down-draft. The double-eye pattern occurs from a down-stream, where cold material is transported towards the inner shell. The red box shows an experimental interferogram.

that the velocities are larger in the inner half layer than in the outer half layer. This could be a consequence of (i) an increased radial acceleration due to the dielectrophoretic force field and (ii) from the spherical geometry. In addition, the fluid is heated by passing the middle of the gap and hence accelerated (small, deep red colored vectors).

Published and presented in:

F. Zaussinger, C. Egbers, A. Krebs, and V. Travnikov. New results of the spherical convection experiment Geoflow IIc. In *EGU General Assembly Conference Abstracts*, volume 19 of *EGU General Assembly Conference Abstracts*, page 7801, Apr. 2017. URL <https://meetingorganizer.copernicus.org/EGU2017/EGU2017-7801.pdf>

F. Zaussinger, P. Haun, M. Neben, T. Seelig, V. Travnikov, C. Egbers, H. Yoshikawa, and I. Mutabazi. Dielectrically driven convection in spherical gap geometry. *Phys. Rev. Fluids*, 3:093501, Sep 2018. doi: 10.1103/PhysRevFluids.3.093501. URL <https://link.aps.org/doi/10.1103/PhysRevFluids.3.093501>

F. Zaussinger, P. Haun, I. Mutabazi, and C. Egbers. Dielectrically driven convection in spherical gap geometry. In *Scientific programm EFMC12*, volume 1 of *Scientific programm EFMC*, page 46, September 2018. http://info.tuwien.ac.at/efmc12/EFMC12_program_v3.2.pdf

V. Travnikov, F. Zaussinger, P. Haun, and C. Egbers. Influence of dielectrical heating on convective flow in a radial force field. *Phys. Rev. E*, 101:053106, May 2020. doi: 10.1103/PhysRevE.101.053106. URL <https://link.aps.org/doi/10.1103/PhysRevE.101.053106>

F. Zaussinger, P. Haun, P. Szabo, V. Travnikov, M. Al Kawwas, and C. Egbers. Rotating spherical gap convection in the GeoFlow International Space Station (ISS) experiment. *Phys. Rev. Fluids*, 5:063502, Jun 2020. doi: 10.1103/PhysRevFluids.5.063502. URL <https://link.aps.org/doi/10.1103/PhysRevFluids.5.063502>

5 Rotating convection

Rayleigh-Benard convection in the rotating spherical gap is considered as simplified model for flows such as found in planets or stars. In particular, the mixed heating scenario of a temperature gradient across the gap and internal heating in the rotating frame is of great interest. Such investigations are performed within the GeoFlow experiments, too. In the following, results of convective onset calculations and a detailed statistical analysis of three-dimensional simulations are presented. The numerical results are compared with interferogram from the GeoFlow experiment.

5.1 Classification

Out of 240 analyzed experimental points (EP) 14% with $\lambda < 1$ and 86% with $\lambda \geq 1$ with a mean value of $\lambda = 5.6$ and median of $\lambda = 2.1$ are found. The minimum value is $\lambda = 0.16$ at $V_{rms} = 1273$ V with temperature difference of $\Delta T = 9.5$ K. The maximum value of $\lambda = 60$ is found for the highest available voltage $V_{rms} = 4596$ V and the lowest temperature difference $\Delta T = 0.4$ K. All cases with $\lambda < 1$ are found at low voltage ($V_{rms} = 1273$ V) in combination with high temperature differences $\Delta T > 3$ K. This distribution results from the previous definition of experimental points in the $\Delta T - V$ plane and not from the newly introduced $\lambda - L$ plane.

All 160 rotating EPs of the GeoFlow experiment are grouped into four clusters with respect to four Ekman numbers and two Prandtl numbers, ($Ek = 7.6 \times 10^{-3}, Pr = 176$), ($Ek = 5.2 \times 10^{-3}, Pr = 125$), ($Ek = 3.8 \times 10^{-3}, Pr = 176$) and ($Ek = 2.6 \times 10^{-3}, Pr = 125$). Figs. 16a-d visualize these clusters. To provide an adequate overview, the experimentally recorded interferograms are analyzed and categorized into several separate cases where the conductive states are colored in dark gray, Taylor columns in red, transitional cases with remnants of columnar cells in blue and turbulent cases in green. The black line with \square -symbols represents the result of linear stability analysis with the critical Rayleigh number L_c , whereas the black line with ∇ -symbols separates the weakly non-linear regime ($L < 6L_c$) from the transitional regime. The vertical dashed line represents the transition between convection where the temperature difference across the gap dominates the convective energy transport ($\lambda < 1$) and the internal heating dominated convection ($\lambda > 1$).

Non-rotating cases cover the same $\lambda - L$ plane such as the rotating cases and are not presented separately.

5.2 Onset of convection and base flow

Critical values for the Rayleigh number L have been calculated for all experimental points in the rotating case. The black line in Fig. 16 depicts critical Rayleigh numbers in the $\lambda - L$ plane. It is observed that for increasing internal heating parameter λ the critical values L_c decrease. In the rotating case the threshold of the convective onset is characterized by the destabilization of the base flow which is observed by the interferometry unit when the fringe pattern is distorted. The theoretical onset of convection in two rotating cases is validated experimentally by interferograms presented in Fig. 17 for $\Delta T = 0.4$ K, $\Delta T = 1.7$ K and $\Delta T = 3.0$ K. Fig. 12 depicts 12 cases, showing 11 interferograms. For the case $f = 0.8$ Hz, $\Delta T = 3.0$ no conductive experimental point is present. Here, the onset voltage is below the minimum voltage. Over the entire parameter range the onset of convection is located within the error given by the distance of points in the parameter space of L and λ . However, the coarse grid of experimental points of GeoFlow makes it difficult to make more accurate statements about the convective onset. This is based on voltage increments of 921 V and temperature increments of 1.3 K. Hence, the onset cannot be captured more precisely with this setup, but with a mean deviation of 177 V. This is based on the investigation of 42 interferograms, which have been used for this study.

In the presence of rotation a two-dimensional axisymmetric and equatorially-symmetric steady base flow appears ($u_r, u_\theta, 0$). Warm fluid is displaced radially outwards at the poles whereas cold fluid is transported inwards close to the equatorial plane. When the observed flow exhibits the axisymmetric flow the solution of the equations cannot be derived analytically and has to be calculated numerically. A meridional flow is observed in a two-cell structure at $Ek, Fr \sim 10^{-3}$ where the temperature maximum is found in the gap for internal heating. However, at the poles there is a radial shift of the temperature maxima towards the outer shell

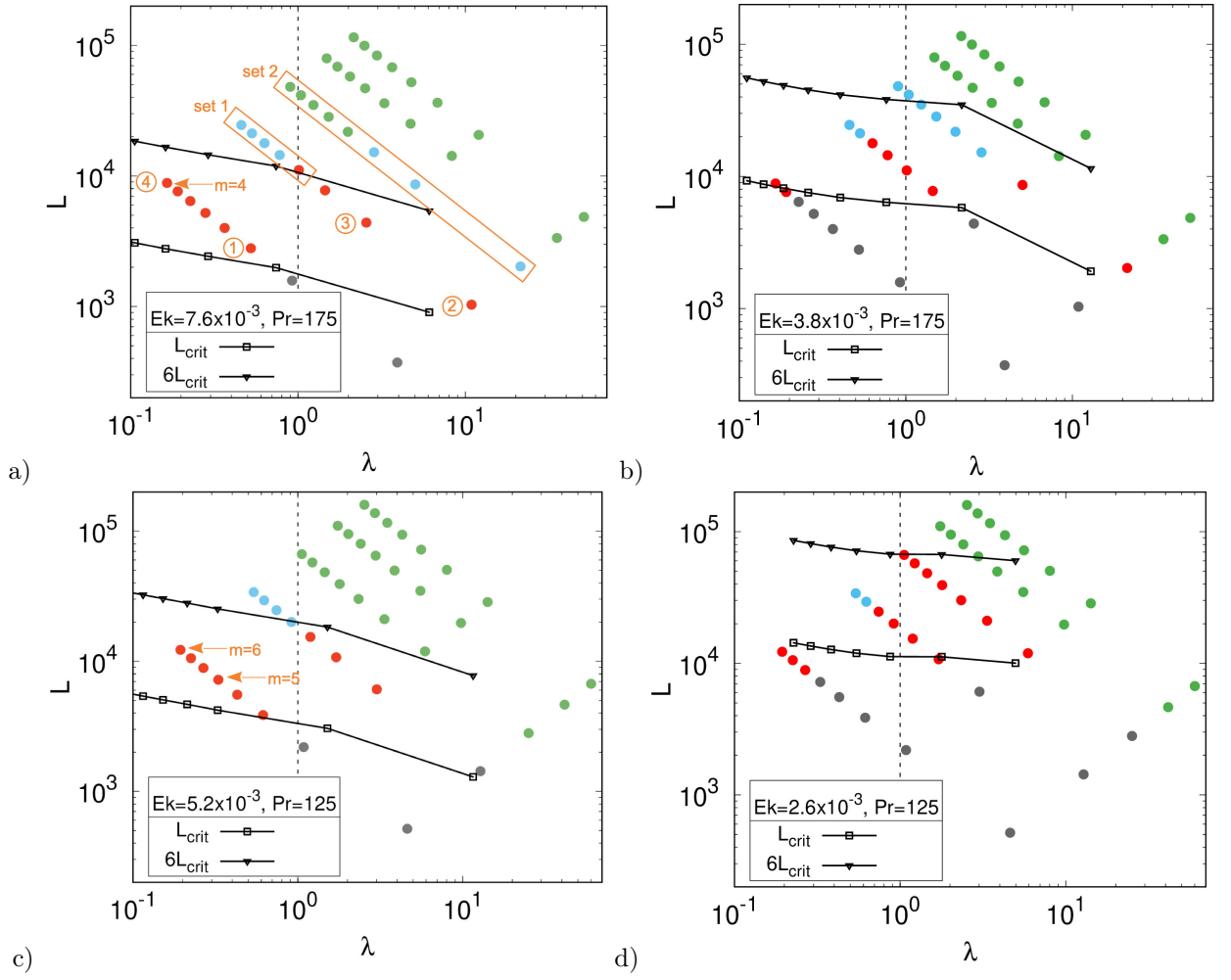


Figure 16: Experimental points (EP) of the GeoFlow experiment in the λ - L plane for a) $Ek = 7.6 \times 10^{-3}$, $Pr = 175$, b) $Ek = 3.8 \times 10^{-3}$, $Pr = 175$, c) $Ek = 5.2 \times 10^{-3}$, $Pr = 125$ and d) $Ek = 2.6 \times 10^{-3}$, $Pr = 125$. Dark gray dots represent the conductive cases, red dots the columnar flows, blue dots the transition and green dots the turbulent cases. Black lines with \square -symbols mark the onset of convection, and with ∇ -symbols the transition to the turbulent regime.

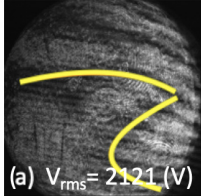
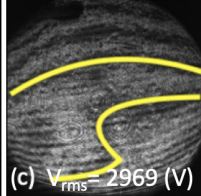
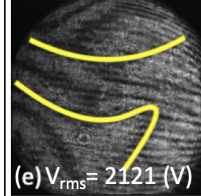
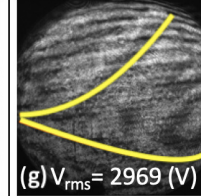
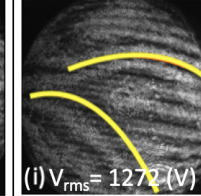
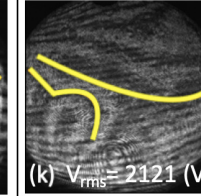
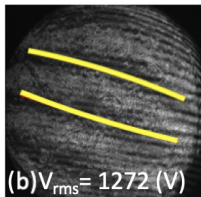
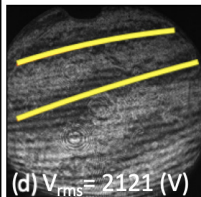
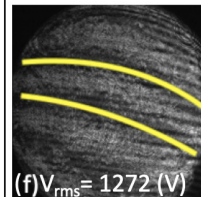
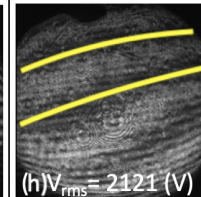
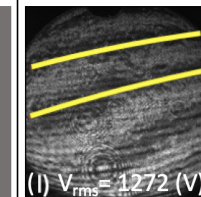
Ta=17200 / $\Delta T=0.4(K)$	Ta=68800 / $\Delta T=0.4(K)$	Ta=17200 / $\Delta T=1.7(K)$	Ta=68800 / $\Delta T=1.7(K)$	Ta=17200 / $\Delta T=3.0(K)$	Ta=68800 / $\Delta T=3.0(K)$
 (a) $V_{rms}=2121(V)$	 (c) $V_{rms}=2969(V)$	 (e) $V_{rms}=2121(V)$	 (g) $V_{rms}=2969(V)$	 (i) $V_{rms}=1272(V)$	 (k) $V_{rms}=2121(V)$
 (b) $V_{rms}=1272(V)$	 (d) $V_{rms}=2121(V)$	 (f) $V_{rms}=1272(V)$	 (h) $V_{rms}=2121(V)$	(j) No experimental data available	 (l) $V_{rms}=1272(V)$
$V_{rms,crit}=1982(V)$ $Ra_{Ec}=2800$	$V_{rms,crit}=2887(V)$ $Ra_{Ec}=5939$	$V_{rms,crit}=1424(V)$ $Ra_{Ec}=6148$	$V_{rms,crit}=2438(V)$ $Ra_{Ec}=18006$	$V_{rms,crit}=1185(V)$ $Ra_{Ec}=7513$	$V_{rms,crit}=1923(V)$ $Ra_{Ec}=19772$

Figure 17: Experimental interferograms for the rotating case for $\Delta T = 0.4K$, $\Delta T = 1.7K$, $\Delta T = 3.0K$, $f = 0.8Hz$ ($Ta = 17200$) and $f = 1.6Hz$ ($Ta = 68800$). The upper row depicts convectively unstable flows, the lower row depicts conductive cases. The onset of convection is located in between both rows. Different orientations of lines exhibit from different positions of the Wollaston prism.

(see Fig. 18c). The base flow of the rotating GeoFlow experiment shows a plume-like structure at the North Pole and wave distortions in the interferograms. These waves are projections of the radial, parabolic temperature profile resulting from centrifugal force. Fig. 18a shows these structures with yellow lines. Numerical simulations and the corresponding numerically evaluated interferograms agreed well with the experimental observation, see Fig. 18b and 18c. However, the numerical reconstruction of the interferograms shows a more pronounced fringe pattern in the polar region. This however is a result of the differently calibrated interferometry unit that is used for the calculation.

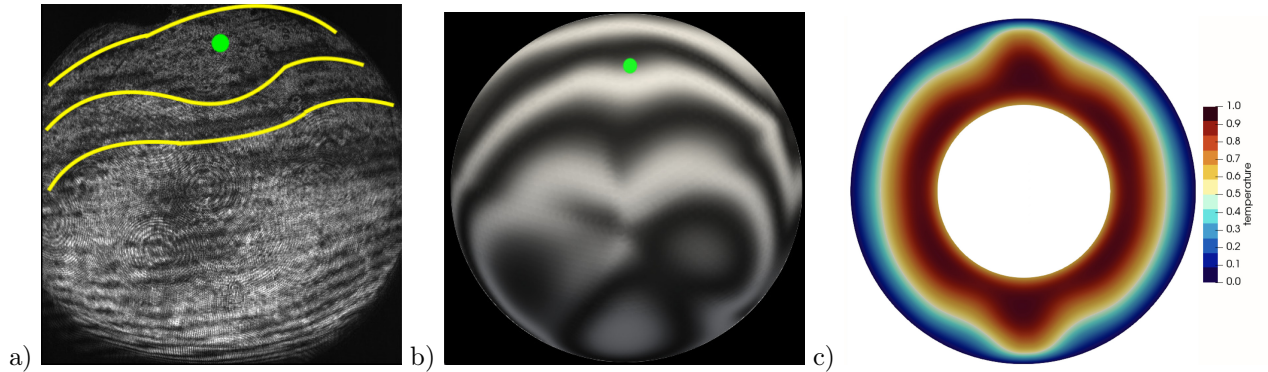


Figure 18: a) experimental interferogram for $Ek=5.2 \times 10^{-3}$ and $\lambda = 1$ for the conductive case. The base flow structures are outlined in yellow, with a sinusoidal distortion around the North Pole labeled with a green dot. The equator is found in the lower part of the interferogram. b) numerical interferogram of the same parameters evaluated by a three-dimensional simulation. c) vertical plane of the temperature distribution through both poles.

5.3 Weakly nonlinear regime

The weakly nonlinear regime is defined as the region where $L \lesssim 6L_c$ [37]. In this regime, the dynamics follow approximately the Proudman-Taylor (PT) theorem with $\frac{\partial \mathbf{u}}{\partial z} \approx \mathbf{0}$, where z denotes any line parallel to the z -axis of rotation. Within this regime, the pressure force is balanced by the Coriolis force and leads to the formation of columnar cells which are aligned with the rotation axis and confined by the tangent to the inner

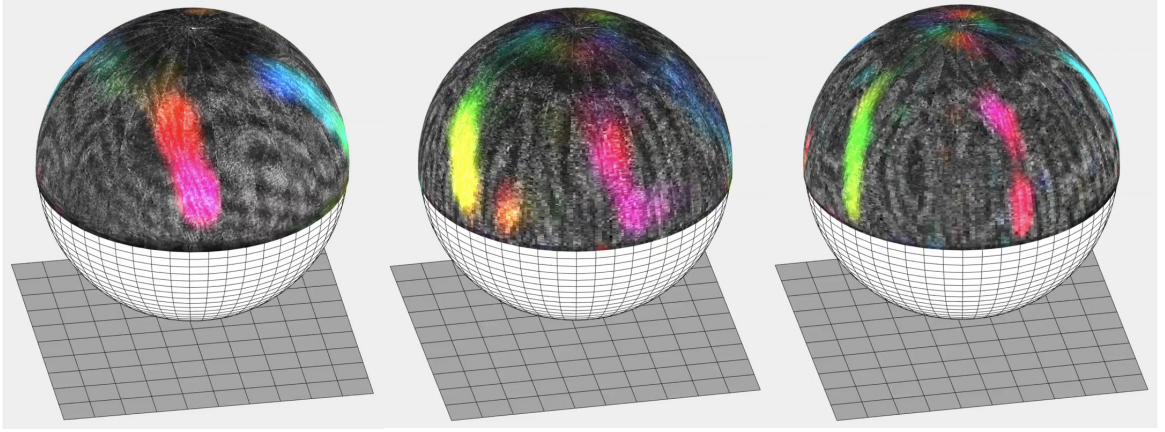


Figure 19: Columnar cells with wave number $m=4-6$ found in the rotating micro-gravity GeoFlow experiment. The convective structures are visualized by automatic pattern recognition and projected onto a spherical shell. The colors refer to angles of identified fringe lines.

sphere. Tilded convective Taylor columns (spirals) occur for impermeable boundaries that tilt the columnar cells. These spirals are well known to occur for moderate Prandtl numbers and are visible in equatorial cuts of the corresponding numerical simulations (see [118]). The azimuthal wave numbers of the Taylor columns are estimated using $m \sim Ek^{-1/3}$ [5, 37] which corresponds to $m \sim 5 - 7$ for the parameter range of the GeoFlow experiment. Deviations from the theoretical values by one wave number can be explained by the influence of the supply shaft at the South Pole of the experiment (Fig. 4) and by the non-uniform buoyancy force. The regime in which columnar cells occur is delimited by the $6L_c$ criterion, but does not depend on λ , Ek or Pr .

Fig. 20 shows columnar cells with a four-fold, five-fold and six-fold symmetry. The corresponding experimental points are labeled with wave numbers in Figs. 16a-d. The star-like structures show steep thermal upwelling and large down-welling regions. Columnar cells can be identified as butterfly patterns which are observed in the upper part of Fig. 20c. Spiral structures are found for cases as presented in Fig. 20a and 20b.

5.4 Transitional regime for $\lambda \leq 1$

For $L > 6L_c$ the regular columnar cells disperse and the flow becomes more turbulent. Fig. 25a shows a representative EP where the columnar cells are visible, but not regular any more. Consequently, Gastine et al. [36] denoted this parameter regime as the 'transitional regime'. A set of five representative EPs were analyzed for $L > 6L_c$ and $\lambda < 1$ and are shown in Fig. 16a as four blue dots and the red dots inside the region defined as 'set 1'.

5.4.1 Thermal profile

The electric Rayleigh number L is in the range of $1.1 \times 10^4 \leq L \leq 2.4 \times 10^4$ which corresponds to values slightly above the weakly non-linear regime with heating parameters between $0.16 \leq \lambda \leq 1.01$. The shell- and time averaged temperature field $\langle T \rangle$ and the corresponding variance $\langle T'^2 \rangle$ are shown in Figs. 21a-b. For the entire parameter range, the mean temperature shows a well mixed bulk between $r = 1.1$ and $r = 1.7$. The plateau in $\langle T \rangle$ between $r = 1.1$ and $r = 1.7$ indicates that in the mean there are no steep gradients.

Just as in the weakly non-linear regime, the centrifugal force and the spherical geometry lead to a non-Gaussian thermal distribution for $r > 1.5$. Polar plumes form a cell covering the entire gap. Columnar cells confined by the tangent cylinder are only weakly connected to the outer shell. This results in a broad boundary layer at the outer shell, but an increase in skewness $\langle S \rangle$ and kurtosis $\langle K \rangle$ due to polar plumes, see Fig. 21c and 21d. The skewness is bounded by $\sqrt{2}$ for $r < 1.75$ due to columnar cells and this leads to a sub-Gaussian ($K \sim 2$) distribution. In contrast to the weakly non-linear regime, this region is more strongly mixed due to higher convective fluxes.

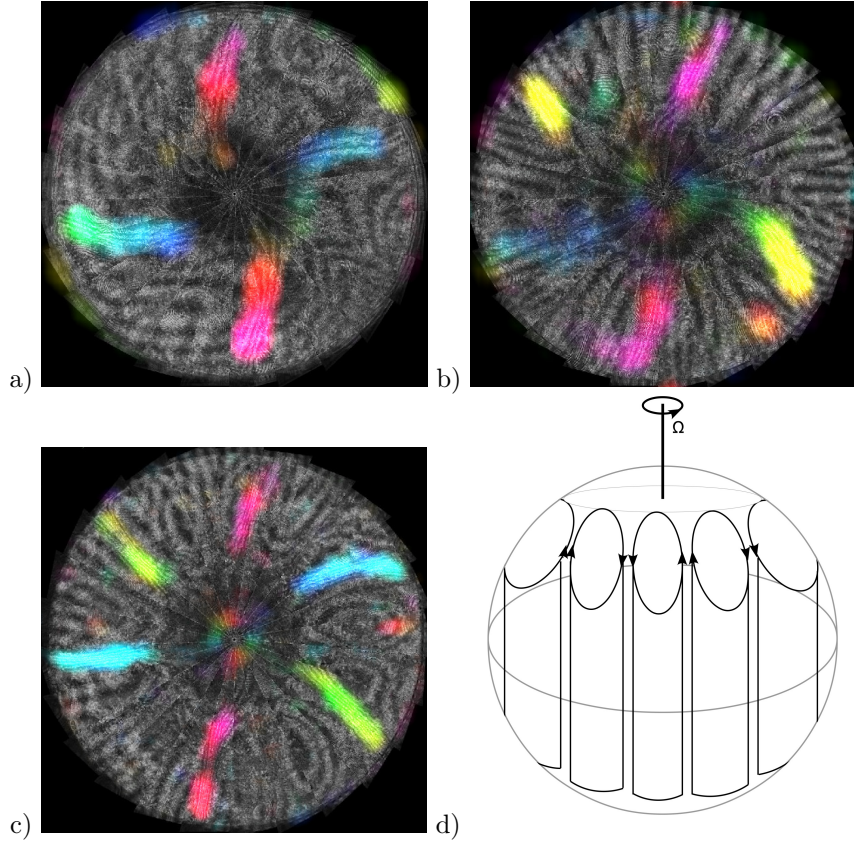


Figure 20: Coaxial view on the northern hemisphere. Columnar cells are visualized by automatic pattern recognition, Zaussinger et al. [111]. The North Pole is located in the center and the equator at the outline. The colors refer to angles of identified fringe lines. a) spiraling columnar cells with $m = 4$ for $L = 8849$, $Ek = 7.6 \times 10^{-3}$ and $\lambda = 0.16$, b) slightly spiraling columnar cells with $m = 5$ for $L = 7217$, $Ek = 5.2 \times 10^{-3}$ and $\lambda = 0.33$, c) almost straight cells with $m = 6$ for $L = 12243$, $Ek = 5.2 \times 10^{-3}$ and $\lambda = 0.19$. d) sketch of columnar cells aligned with the rotation axis in the spherical shell.

5.4.2 Stability and Brunt-Väisälä frequency

Fig. 22a shows an additional effect of the centrifugal force. A steep gradient exhibits in the dielectrophoretic acceleration, \mathbf{a}_e , at the equatorial region close to the inner shell with $r < 1.1$. The steep gradients at the inner shell are caused by the boundary layers formed by the columnar cells. As shown in Fig. 22a, the dielectrophoretic acceleration as well as the Brunt-Väisälä frequency nearly vanish for $r > 1.1$. The confinement of columnar cells by the tangent cylinder and the resulting stable stratification above $r = 1.6$ reduce the thermal gradients and hence the dielectrophoretic acceleration. In summary, the outer boundary regions of the mid-latitudes are nearly adiabatically stratified with $N^2 \sim 0$. In the polar regions, the dielectrophoretic acceleration and the BV frequency are non-zero at the outer shell which agree with the results shown in Fig. 13c. The mean dielectrophoretic acceleration shows a small peak around $r = 1.8$ which is due to the boundary layer. The horizontal components of \mathbf{a}_e does not contribute significant driving in the mean. (see Fig. 22b and 22c.) The absolute values are two to three orders of magnitudes smaller than the radial component which justifies the use of Eqs. 17-18 for the parameter range investigated.

5.5 Transitional regime for $\lambda > 1$

A set of seven representative EPs with $2.0 \times 10^3 < L < 3.5 \times 10^4$ are analyzed for the parameter regime $\lambda > 1$, $Pr = 175$ and $Ek = 3.8 \times 10^{-3}$. The heating parameters range between $1.2 < \lambda \leq 21$ and are shown in Fig. 16a as four green circles and three blue circles labeled as 'set 2'.

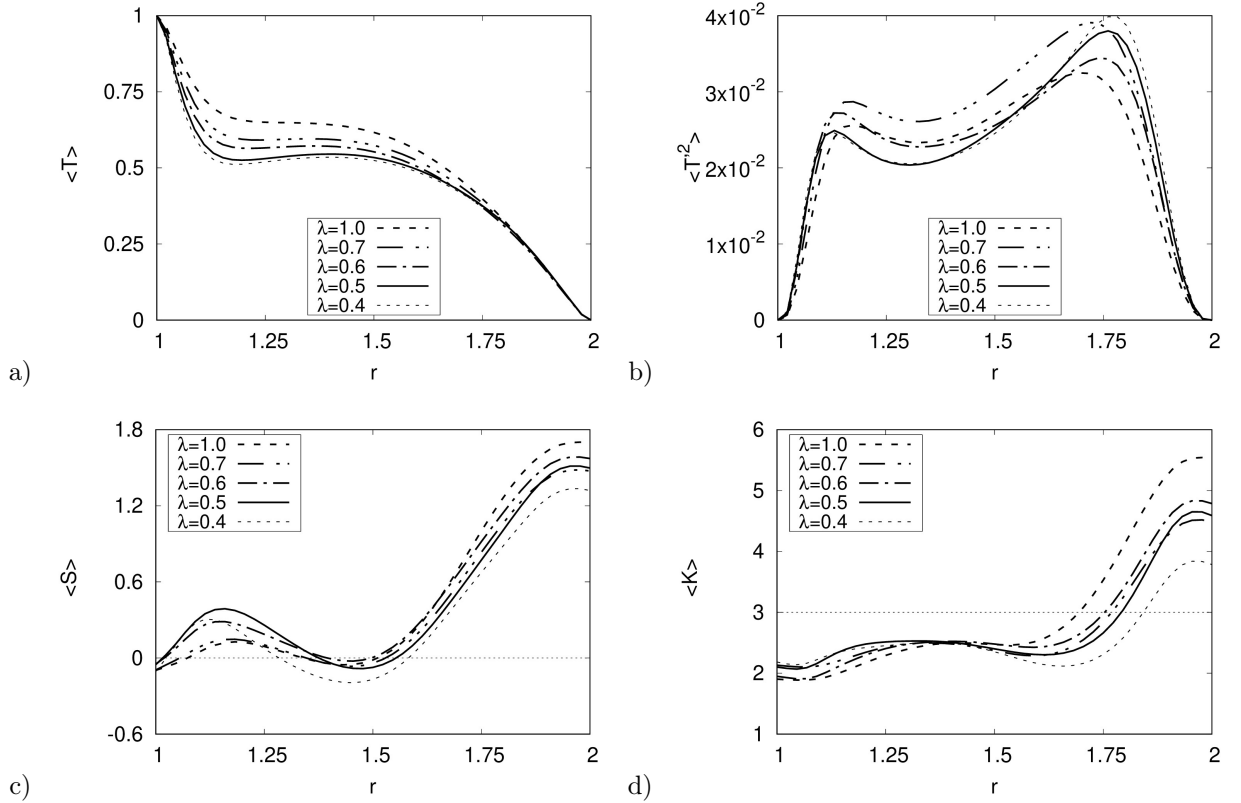


Figure 21: Averaged a) temperature, b) temperature variance, c) skewness of temperature, d) kurtosis of temperature for $\lambda \leq 1$ and $1.4 \times 10^4 < L < 2.4 \times 10^4$.

5.5.1 Thermal profile

The maximum of the mean temperature is found in the middle of the gap (see Fig. 23a) and shifted towards the outer shell located at $r = 1.5$ which represents a higher value than that of the conductive case $r_{max} = 4/3$. This shift was also observed in Zaussinger et al. [114] and can be explained by an 'eroding' convective flow.

The observed thermal fluctuations (see Fig. 23b) in the outer gap region are higher than in the case of $\lambda < 1$. This leads to statistical outliers and therefore high values in the kurtosis. This is well observed for the case where $-1 < S \lesssim 0$ and $2 < K \lesssim 3$ and is indicated in Fig. 23c and 23d. In contrast to the cases with low internal heating, the skewness is negative in the lower gap region, but showed a steeper ascent for $r < 1.75$. A closer look to the three-dimensional temperature field reveals the negative sign of S and shows strong down-welling plumes. Four distinct plumes are highlighted and occurred as double-eye structures as shown in Fig. 25b where white rectangles highlight these structures. However, columnar cells are not observed for $L > 5 \times 10^4$ which is a result of the internal heating process. The columnar cells vanish by the convective flux that reversed the sign of the dielectrophoretic acceleration.

5.5.2 Stability and N^2

For $\lambda \geq 5.0$ the dielectrophoretic acceleration is positive between $r = 1.1$ and $r = 1.4$ (see Fig. 24a). However, near the outer boundary, the dielectrophoretic acceleration is small or zero. The inversion of the sign of the dielectrophoretic acceleration would lead to a separation of the flow into two unstable layers separated by a stable, diffusive interface. However, layering is not observed in the numerical simulations. This can be explained by the buoyancy force in the gap. The dielectrophoretic acceleration is at least an order of magnitude higher at the inner shell than in the bulk or in the upper shell. This destabilized the diffusive interface where the dielectrophoretic acceleration changes sign and is able to form a convection cell which fills the entire gap. The negative sign of the BV frequency over the entire gap confirms this and is shown in Fig. 24. The horizontal

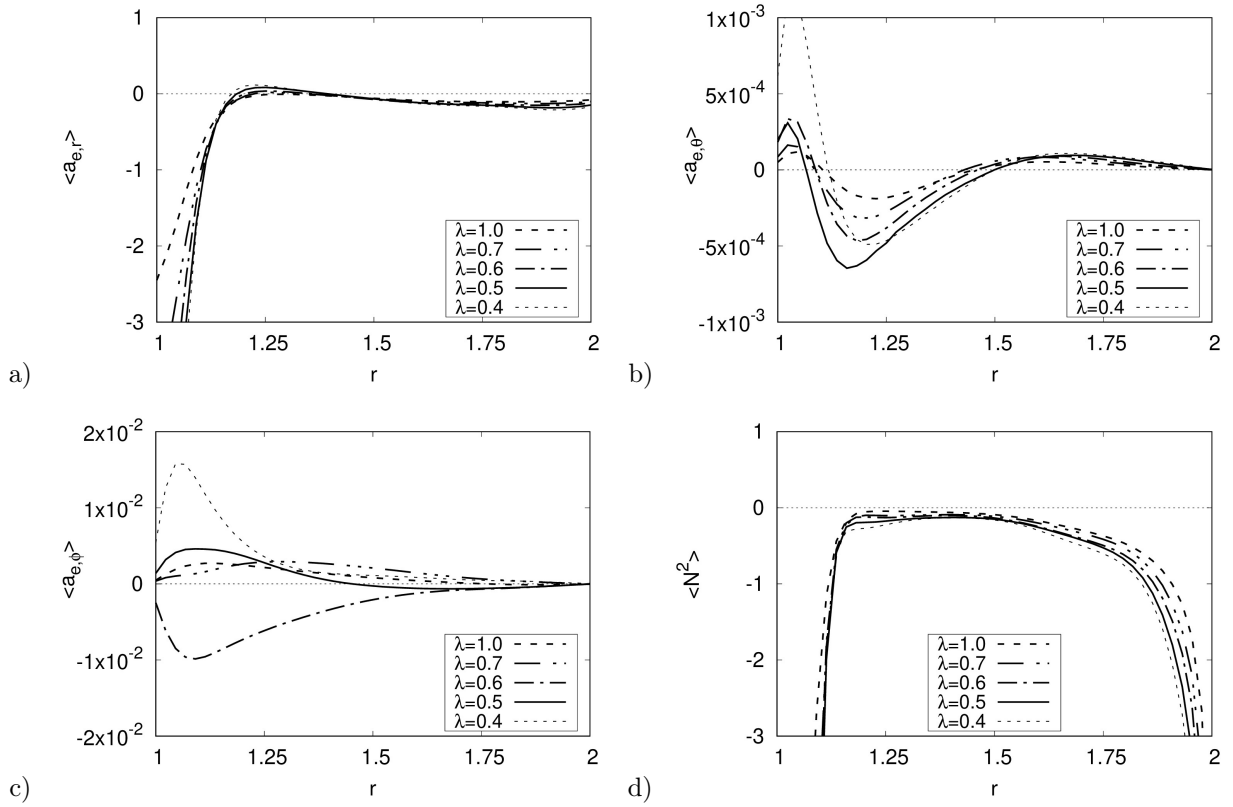


Figure 22: Averaged a) radial component of dielectrophoretic acceleration, b) meridional component of dielectrophoretic acceleration, c) azimuthal component of dielectrophoretic acceleration and d) Brunt-Väisälä frequency for $\lambda < 1$ and $1.4 \times 10^4 < L < 2.4 \times 10^4$.

components of the dielectrophoretic acceleration are of comparable magnitude to those in the case of $\lambda < 1$ and do not contribute to the flow.

Published and presented in:

F. Zaussinger. GeoFlow I and GeoFlow II: A Review. In Book of abstracts, School ISTROF 2019, Instabilities and Turbulence in Strato-Rotational Flows, Cottbus. BTU Cottbus-Senftenberg, 2019

F. Zaussinger. Influence of internal heating on convection in the rotating spherical gap. In Book of Abstracts - ETC 2019, 2019. URL <http://www.symposium.it/files/eventi/84/etc-2019-561.pdf>

F. Zaussinger, P. Haun, P. Szabo, V. Travnikov, M. Al Kawwas, and C. Egbers. Rotating spherical gap convection in the GeoFlow International Space Station (ISS) experiment. Phys. Rev. Fluids, 5:063502, Jun 2020. doi: 10.1103/PhysRevFluids.5.063502. URL <https://link.aps.org/doi/10.1103/PhysRevFluids.5.063502>

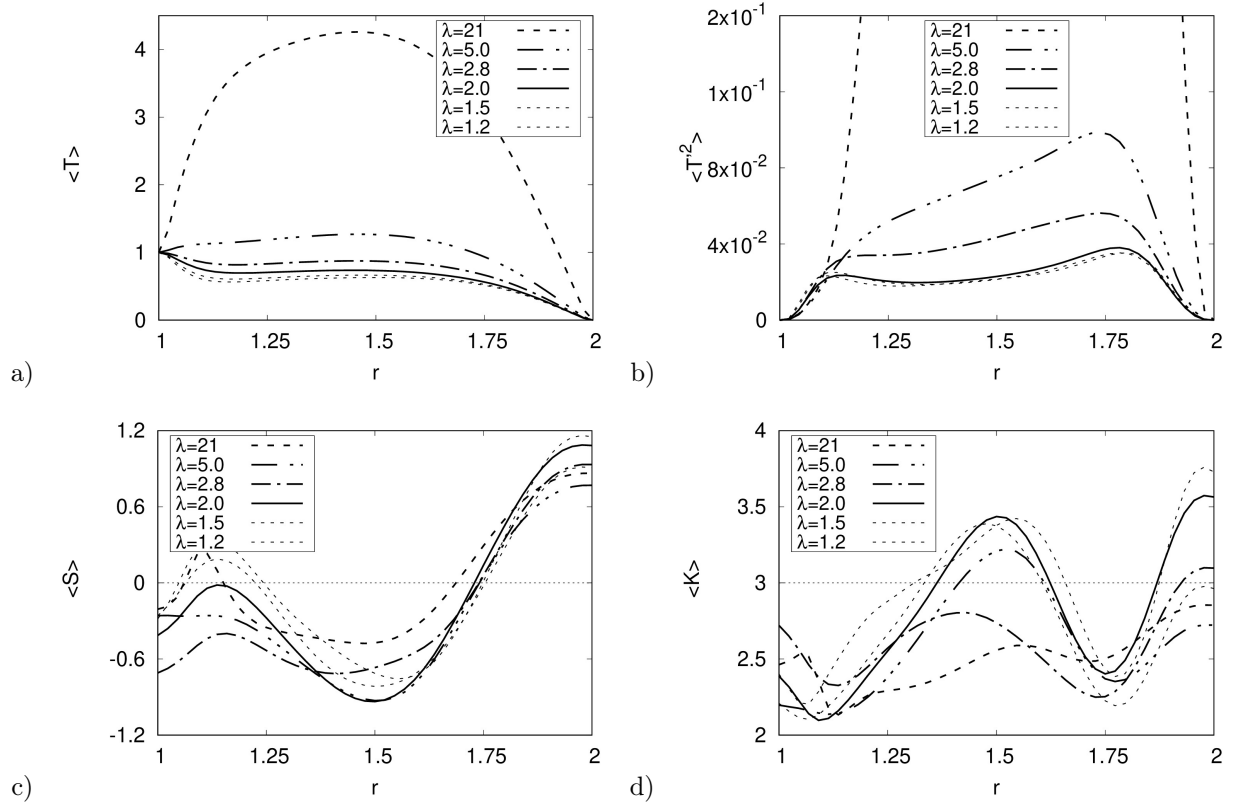


Figure 23: Averaged a) temperature, b) temperature variance, c) skewness of temperature, d) kurtosis of temperature for $\lambda \geq 1$ and $2.0 \times 10^3 < L < 3.5 \times 10^4$.

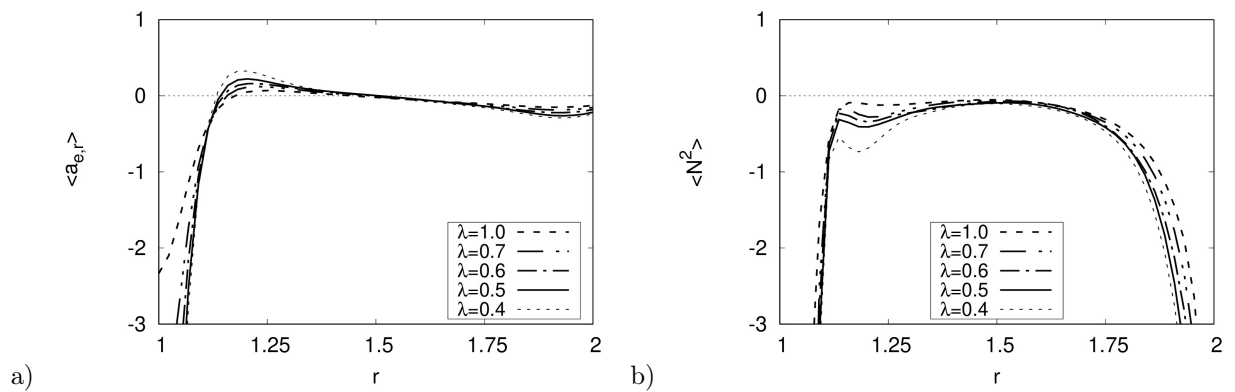


Figure 24: Averaged a) radial component of dielectrophoretic acceleration and b) Brunt-Väisälä frequency for $\lambda \geq 1$ and $2.0 \times 10^3 < L < 3.5 \times 10^4$.

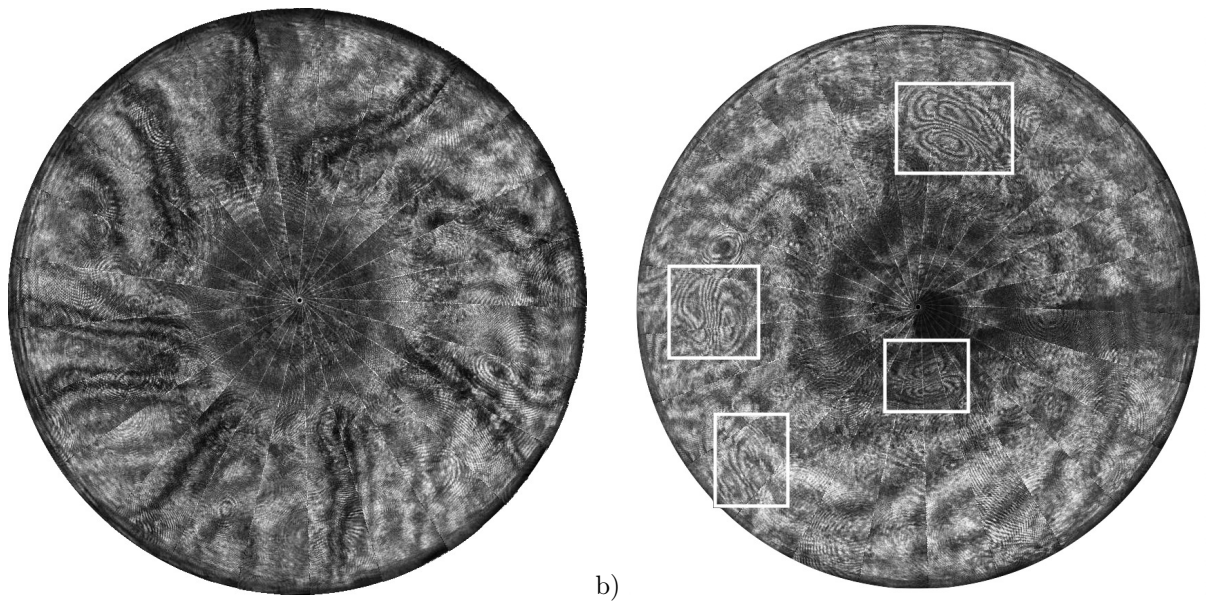


Figure 25: Interferograms of the GeoFlow experiment with the North Pole at the center of the circle: a) remnants of columnar cells for $L = 2.4 \times 10^4$ and $\lambda = 0.7$. b) equatorial plumes for $L = 6000$ and $\lambda = 60$ with highlighted structures after post-processing.

6 Influence of viscosity contrast

The existence of dielectric heating in 1-Nonanol was found in 2017. Prior to this finding the influence of the viscosity contrast was investigated in more detail to explain hysteresis effects in the GeoFlow experiment. The work on the viscosity contrast has led to several publications. The following section represents only a small selection of the scientific work. Hence, I refer to the publications listed at the end of this section.

6.1 Equations

An incompressible viscous dielectric fluid in the spherical gap of width $d = R_2 - R_1$ is considered. The inner surface is maintained at the warmer temperature than the outer one ($T_1 > T_2$). Introducing the following scaling $\Delta T = T_1 - T_2$ for the temperature, $\rho_0(\kappa_T/d)^2$ for the pressure, d for the length, κ_T/d for the velocity and $t_{\kappa_T} = d^2/\kappa_T$ for the time, and using the Boussinesq approximation, the Navier-Stokes equation, the energy equation and the continuity equation can be written in the dimensionless form as follows:

$$\begin{aligned} \text{Pr}^{-1} \left[\frac{\partial \mathbf{U}}{\partial t} + (\mathbf{U} \cdot \nabla) \mathbf{U} \right] &= -\text{Pr}^{-1} \nabla P + L \frac{\eta^2}{(1-\eta)^4} \frac{T}{r^5} \mathbf{e}_r \\ &+ \nabla \cdot \left[\frac{\nu(T)}{\nu_{\text{ref}}} (\nabla \mathbf{U} + (\nabla \mathbf{U})^T) \right], \end{aligned} \quad (29)$$

$$\frac{\partial T}{\partial t} + (\mathbf{U} \cdot \nabla) T = \nabla^2 T, \quad (30)$$

$$\nabla \cdot \mathbf{U} = 0. \quad (31)$$

The flow depends on the radius ratio $\eta = R_1/R_2$, the Prandtl number $\text{Pr} = \nu_{\text{ref}}/\kappa_T = 125$ (1-Nonanol, GeoFlow II) and the Rayleigh number

$$L = \frac{2\epsilon_0\epsilon_r e}{\rho_0\nu_{\text{ref}}\kappa_T} V_{\text{rms}}^2 \Delta T,$$

where ϵ_r is the relative permittivity, e is the electric expansion coefficient, $V_{\text{rms}}^2 = V_0^2/2$ is the voltage, ρ_0 is the reference density and ν_{ref} is the viscosity on the outer and colder surface. The velocity should obey the no-slip boundary conditions $\mathbf{u} = 0$ and $T = 1$, $T = 0$ for the temperature on the surfaces $r = \eta/(1-\eta)$ and $r = 1/(1-\eta)$, correspondingly. The influence of the temperature-dependent viscosity is the focus of the research presented. The kinematic viscosity varies according to the Arrhenius law

$$\nu(T) = \nu_{\text{ref}} e^{-(\ln\beta)T}, \quad (32)$$

where $\beta = \nu_{\text{ref}}/\nu_{\text{hot}} = \nu_{\text{cold}}/\nu_{\text{hot}}$ is the viscosity contrast that varies between $\beta = 1$ (constant viscosity) and $\beta = 50$ and must be taken into account by solving the Navier-Stokes equation. The equations (29)-(32) with the boundary conditions have to be solved numerically.

The radial component of the three-dimensional steady flow obtained just above L_c has an octahedral form as in case of constant viscosity $\beta = 1$ [22]. But, in case of the temperature-dependent viscosity, e.g. $\beta = 50$ the flow becomes unstable much earlier at $L_c = 409.96$. This pattern has two dominant modes, corresponding to $\ell = 4$, $m = 0$ and $\ell = 4$, $m = 4$ in qualitative agreement with analytical result obtained by Busse et al. [7] and Bercovici et al.[14]. Fig. 26 depicts the main outcome of this study. It shows the critical Rayleigh numbers as function of the aspect ratio for varying viscosity contrast. Clearly, the critical values decrease for increasing β .

6.2 Comparison of numerical and experimental results

In order to validate the theoretical results the numerical interferograms are compared with the experiment. In principle, only three-fold and four-fold symmetries of the m-mode in the interferograms are observed. These

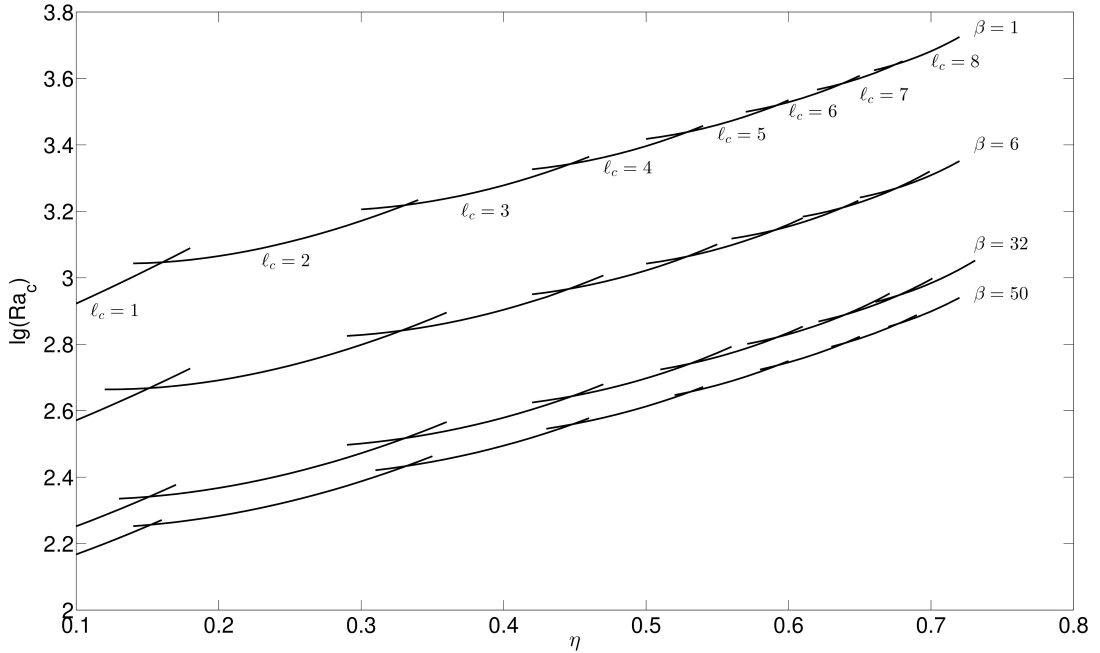


Figure 26: Critical Rayleigh numbers L_c as function of radius ratio η . source: [88]

structures exhibit in regular, star-shaped patterns. The detection of ℓ -mode is not unique, since the optical access does not allow to investigate the whole lateral elongation. However, symmetries in the angles between the sheet-like plumes can be used. The angles between the stripes measure theoretically 120° in the three-fold case and 90° in the four-fold case. This geometrical property can be used to identify the m -modes. Optical distortions lowers and rises the observed angles by 20-30%, depending on the interferometry direction. The angle between the rays are helpful, but not sufficient for the unique identification. As the experiment rotates very slowly (0.008 Hz, Ekman number $Ek \sim 1$), the fringe lines change their relative shape, too. Only by tracking the structures individually, it is possible to identify them. Fig. 28, first column, presents four experimental set points, namely $L = 3040$, $L = 4200$, $L = 5365$ and $L = 7689$. A false (in the sense of interferometry) convective state is observed: The experimental interferograms do not show significant fringe patterns for $L = 3040$ while according to the stability analysis a convective flow is expected. (This is a result of the missing internal heating source!) The case $L = 4200$ displays a four-fold mode ($m = 4$). As found in the numerical simulations, a transition from $m = 4$ to $m = 3$ is observed as the Rayleigh number is increased from $L = 4200$ to $L = 5365$. These patterns are dominant up to $L = 1.4 \cdot 10^4$. Higher values exhibit in transient, time-dependent flows. In summary, the $m = 3$ and the $m = 4$ modes are predominant the convective laminar regime for $\eta = 0.5$ and $\beta = 32$ in the GeoFlow IIc experiment.

6.3 Non-uniqueness in the GeoFlow experiment

The experiments show the existence of multiple patterns at the same Rayleigh number. At first, the experimental data seemed to be biased by preceding runs. Therefore, specific set points were repeated randomly which reinforced the suspicion that this parameter space exhibits in multiple stable laminar flows. The $m = 3$ and the $m = 4$ wave modes are found at the same Rayleigh number, but in different set points, see Fig. 28. The angles between the rays as well as the (not presented) time lapse are strong evidences, that both modes are stable. However, the flow with wave number $m = 4$ mode is less frequent than the flow with $m = 3$. It is assumed that the basin of attraction of the mode $m=4$ is smaller than for $m=3$. Now, in 2020, it is known that the internal heating is responsible for this 'non-uniqueness'. It was found that dielectric heating in 1-Nonanol has a great influence on the fluid flow. This was unknown in 2017. Interestingly, the cases of $\beta = 50$ without internal

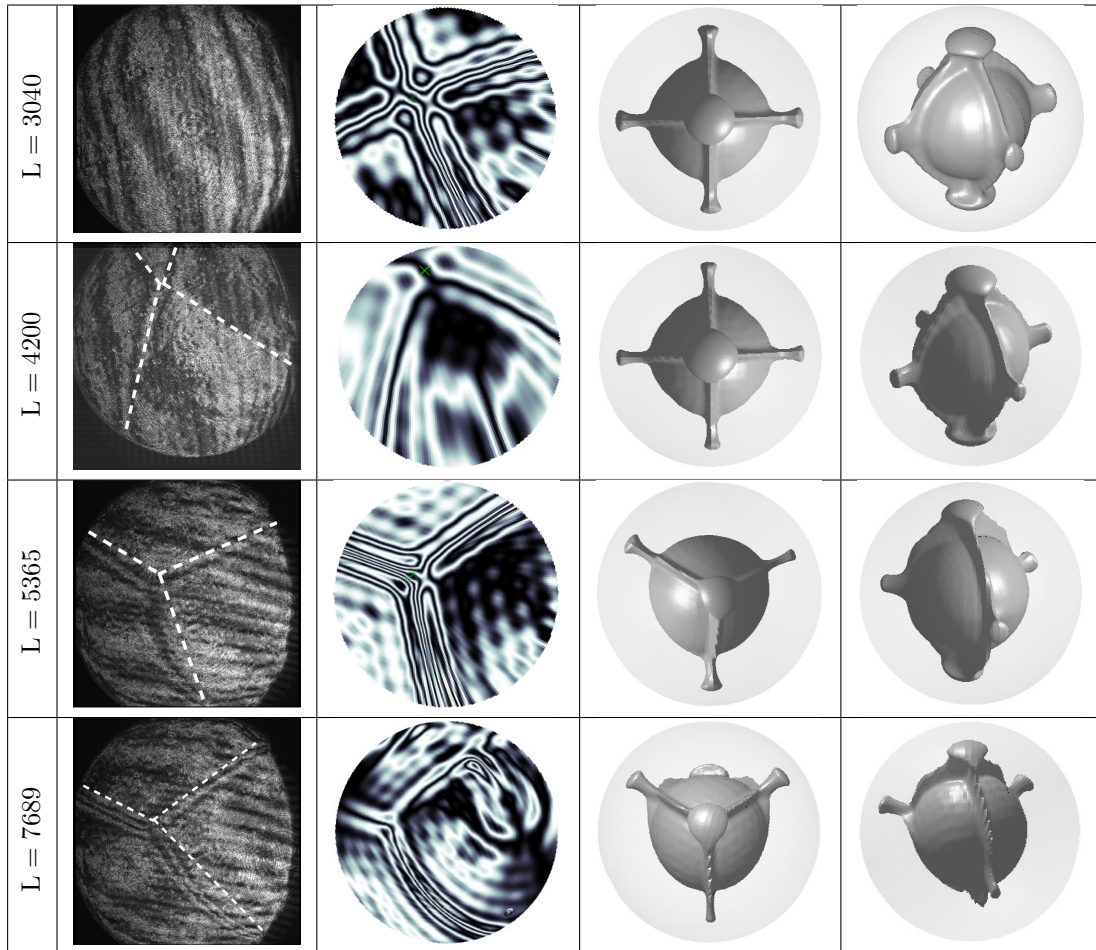


Figure 27: Comparison of experimental and numerical results for various Rayleigh numbers. From left to right: 1) experimental interferograms from the GeoFlow experiment on the ISS. 2) artificial interferograms calculated by numerical simulations 3) top view of numerical simulation 4) side view of numerical simulation. Temperature iso-surfaces are calculated at $T = 0.7$. The artificial interferograms show the same modes as the experiments. Even the transition from $m = 4$ at $L = 4200$ to $m = 3$ at $L = 5365$ is observed. Due to limitations of the interferometry unit, the case of $L = 3040$ shows a false conductive solution.

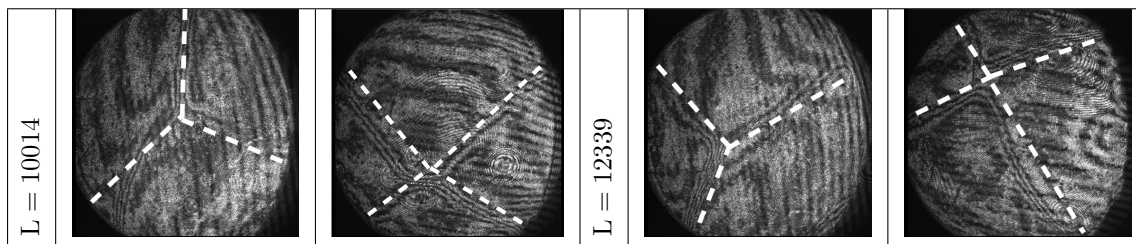


Figure 28: Hysteresis in the laminar experimental regime: Three-fold and four-fold symmetries are observed, however the unstable four-fold symmetry class is more likely in this experiment.

heating and the cases of $\beta = 1$ with internal heating showed nearly identical wave numbers.

Published and presented in:

B. Futterer, **Zaussinger, F.**, C. Egbers, and N. Scurtu. Variation of viscosity contrast for convection experiments in spherical shells as part of geophysical flow simulation experiment GeoFlow II. In EGU General Assembly Conference Abstracts, volume 13 of EGU General Assembly Conference Abstracts, page 5562, 2011

F. Zaussinger, A.-C. Plesa, C. Egbers, and D. Breuer. Mantle Convection in a Spherical Shell: Comparison of Numerical Simulations with the GeoFlow Experiment on the ISS. In A. Abbasi and N. Giesen, editors, EGU General Assembly Conference Abstracts, volume 14 of EGU General Assembly Conference Abstracts, page 9939, Apr. 2012

B. Futterer, A. Krebs, A.-C. Plesa, F. Zaussinger, R. Hollerbach, D. Breuer, and C. Egbers. Sheet-like and plume-like thermal flow in a spherical convection experiment performed under microgravity. Journal of Fluid Mechanics, 735:647–683, 2013. doi: 10.1017/jfm.2013.507

B. Futterer, F. Zaussinger, A.-C. Plesa, A. Krebs, C. Egbers, and D. Breuer. Sheet-like and plume-like thermal flow in a spherical convection experiment with high viscosity contrast. In EGU General Assembly Conference Abstracts, volume 15 of EGU General Assembly Conference Abstracts, pages EGU2013–4830, Apr. 2013

F. Zaussinger, C. Egbers, A. Krebs, F. Schwarzbach, and C. Kunze. Time-dependent convective flows with high viscosity contrasts under micro gravity conditions. In EGU General Assembly Conference Abstracts General Assembly Conference Abstracts, volume 17 of EGU General Assembly Conference Abstracts, page 5833, Apr. 2015. URL <https://meetingorganizer.copernicus.org/EGU2015/EGU2015-5833.pdf>

V. Travnikov, F. Zaussinger, P. Beltrame, and C. Egbers. Influence of the temperature-dependent viscosity on convective flow in the radial force field. Phys. Rev. E, 96:023108, Aug 2017. doi: 10.1103/PhysRevE.96.023108. URL <https://link.aps.org/doi/10.1103/PhysRevE.96.023108>

F. Zaussinger, C. Egbers, and A. Krebs. The GeoFlow experiments on the ISS: Thermal convection under micro-gravity conditions. In Joint Conference ISPS-7 and ELGRA-25 October, 2-6 2017, Juan-les-Pins, France, Abstract book, Joint Conference ISPS-7 and ELGRA-25 October, 2-6 2017, Juan-les-Pins, France, Abstract book, page S. 30, 2017. URL http://www.elgra.org/wp-content/uploads/2017/03/ISPS-7_ELGRA_25_2017_17A02-Abstract-book-final.pdf

7 AtmoFlow

7.1 Introduction

The proposed experiment AtmoFlow differs much from the previous GeoFlow setup. First, the inner and the outer boundaries will both be heated/cooled in such a way that atmospheric-like fluid flows can be investigated. Additionally, a differential rotating unit is foreseen, to simulate deep shells, as they occur in giant planets. Fig. 29 (left) depicts such a simplified atmosphere, where incoming radiation and rotation lead to global cell formation. These cells (Hadley cell, Ferrel cell or mid-latitude cell, polar cell) are well known from the Earth and co-responsible for global atmospheric dynamics. In contrast to Hart's experiment [39], AtmoFlow is designed as a (nearly) full sphere. The advantage of this design is apparent, when equatorial flows and global patterns are investigated. AtmoFlow will be the first experiment under microgravity conditions, which will be able to study simplified global fluid flows, planetary waves and complex patterns in the full spherical shell geometry under atmospheric-like boundary conditions.

The empirical study of planetary waves, global cell formation and fluid dynamical instabilities are in the focus of the experiment. The experiment results will provide benchmark data for a rich variety of numerical problems, which are still a challenge for scientific research in various fields.

7.2 Objectives and scientific program

The AtmoFlow experiment makes it possible to investigate flows, which are driven by internal heating, boundary temperature difference, rotation or complex boundary conditions. It will enable deep insights into EHD driven fluid flows, which can be used for validating simple convection models of planetary atmospheres. The extension of semi-empirical parameterizations of unresolved atmospheric processes, e.g. large-scale / small-scale coupling will be investigated, too. Furthermore, precise parametrization of cell formation will be tested with respect of e.g. Rhines scaling, [71, 40]. This includes the investigation of the heat transfer from the tropics to the stably stratified mid-latitudes, [78]. In addition, the findings of AtmoFlow are expected to be of benefit for validation and development of models that deal with climate change. Various initial temperature distributions will be tested to investigate connections between external forcing and climate variability. The main goal is the elucidation of basic aspects of convection in the rotating spherical shell. This allows the testing of linear stability analysis regarding base flows, convective onsets and bifurcation scenarios in rotating and non-rotating scenarios. Planned applications are presented subsequently:

Non-rotating case

The *non-rotating case* is mainly used to test physical models of electro-hydrodynamics. Especially, the role of mixed heating (internal heating and temperature difference across the gap) is not well understood in the spherical gap geometry, see e.g. [91]. Even though the non-rotating case has no direct geo- or astrophysical counterpart, it is of importance for planned technical applications. The construction of optimized heat exchangers, EHD-based pumps and nozzles will profit from this research. Furthermore, the enhancement of convective heat transfer in absence of gravity (e.g. on space stations or spacecrafts) will benefit from a deeper understanding of EHD driven fluid flows.

Rotating case

AtmoFlow captures only a small range of realistic geo- and astrophysical parameters. Here, two dimensionless numbers corresponding to rotation are introduced. The Taylor number $Ta = (2\Omega d^2/\nu)^2$ with Ω the rotation rate for solid body rotation and the Rossby number $Ro = (\Omega_1 - \Omega_2)/\Omega_2$ with $\Omega_{1,2}$ the rotation rates of the inner/outer shell, respectively. The size and weight of the payload limits the Rayleigh number to $L < 10^6$, the Taylor number to $Ta < 10^7$, the Ekman number to $10^{-2} < Ek < 10^{-3}$, the Prandtl number to $Pr = 8$ and the

Rossby number to $|\text{Ro}| < 4$. However, many rotating flows can be studied with this setup. In the following, typical applications, limitations and the parameter regimes for proposed research scenarios of rotating AtmoFlow experiments are presented:

- *Convection*, more precisely the convective onset, transitions to the turbulent regime and symmetry-breaking bifurcations ([56, 24]) are compared with linear stability analysis and numerical simulations in the super-critical range of $L/L_{\text{crit}} < 20$ and the entire given Taylor number regime. These experiments will be conducted either with internal heating and/or a temperature difference across the gap.
- *Torsional oscillations* and resulting radial equatorial jets ([93, 42]) can be investigated in the entire parameter range for $\text{Re} > 100$. Such experiments depend only on inner sphere dynamics and not on the thermal distribution.
- Several questions arise in the scope of *zonal wind systems* like those found on Jupiter or Saturn. AtmoFlow represents a deep-seated experiment with geometric properties and Ekman numbers comparable to early 3d-simulations by e.g. Christensen [12] and laboratory experiments e.g. Manneville and Olson [57]. The direction of the jets (super-rotation and retrograde equatorial flows) are found to correlate with the convective Rossby number $\text{Ro}_T = \sqrt{L/\text{Pr}} \text{Ek}$. According to definitions by Julien et al. [45] and [34], the AtmoFlow experiment ranges between $10^{-1} < \text{Ro}_T < 10$. The lower limits of Ro_T cover roughly flow regimes as found on planets of our solar system ([94]) e.g. $\text{Ro}_T = 0.5$ on Jupiter’s surface, [34]. Hence, the basic investigation of zonal winds and the role of Ro_T regarding super-rotation as found on Jupiter or Saturn [35] as well as retrograde equatorial jets known from Uranus and Neptune [15] can be conducted by AtmoFlow.

Differential rotating case

The basic *spherical Couette flow* consists of a rotating inner shell and a fixed outer shell. In the context of this setup the excitation of inertial modes [46, 73] will be studied for the Rossby number range of $-4 < \text{Ro} < 4$. Limitations are only given by high Ekman numbers, which are caused by the small outer radius. In geophysics, *differential rotation* plays an important role, when a solid planetary core rotates with a different rate than the surrounding atmosphere or mantle. It produces internal mixing, which proceeds on dynamical time-scales, [55]. For instance, the inner core of the Earth is assumed to super-rotate with 1° per year, [95]. Comparable situations are found in Mercury, Jupiter, Earth’s moon and Galilean moons. Hereby, the Richardson criterion ($\text{Ri} > 0.25$) parameterizes the condition whether the shear instability is dominant over e.g. buoyancy driven instabilities, or not. For the case of thermo-EHD this criterion is not tested and still an unsolved problem.

7.3 Geometry and thermal boundary conditions

The experimental cell, depicted in Fig. 29 (right), will rotate as a complete assembly and the inner sphere will be equipped with an additional drive unit to rotate relative to the experimental cell. The geometry and dimensions of the experiment cell are defined to fulfill the objectives stated in Sec. 7.2. The radius of the outer sphere R_2 is determined by the size and weight of the optical setup as well as the optical accessibility. This trade-off leads to a radius of outer sphere at $R_2 = 0.027$ m, a radius of inner sphere at $R_1 = 0.0189$ m, resulting in a radius ratio of $\eta = R_1/R_2 = 0.7$. The radius of the inner sphere is further chosen to reach a radius ratio in between thin and thick atmospheres.

The key feature of AtmoFlow is the thermal boundary condition. Realistic atmospheric boundary conditions are very complex, however, it is possible to break them down to follow three regions: a) a solar-heated equatorial region with absorption of re-radiated infrared radiation; b) heat sinks in the upper atmosphere of the poles and mid-latitudes, c.f. [10]; c) moderate temperature regions between the polar and the equatorial regions. Imposing these idealized boundary conditions results in a global circulation, which is convectively unstable in the tropics and stable in the mid-latitudes. Hence, the heat transfer from the tropics to the stably stratified mid-latitudes

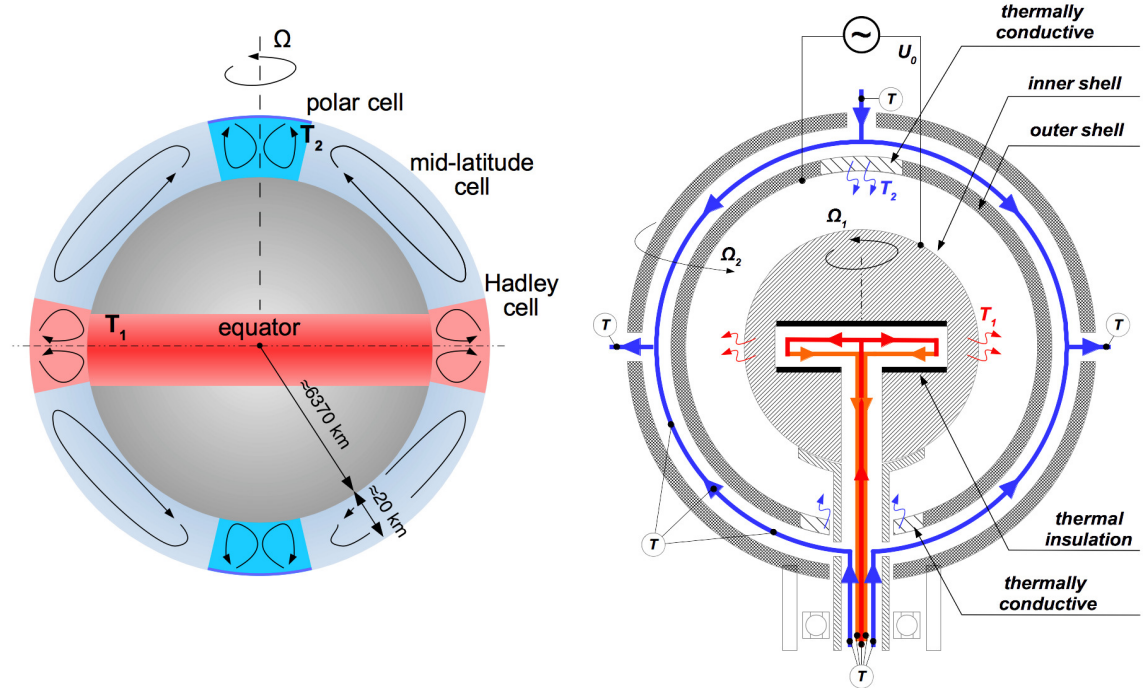


Figure 29: (left) simplified planetary atmosphere as found on the Earth. Not to scale. (right) vertical cut through the AtmoFlow experiment. Blue lines depict the cooling loop, red lines show the heating circuit. Inner and outer rotation is labeled by Ω_1 and Ω_2 , respectively. The maximum temperature is found at the equator T_1 , the minimum temperature at the poles T_2 .

and sub-tropics can be investigated with this setup. A baroclinic wave tank with the same specifications has been investigated by Scolan and Read [78]. They observed the interaction and coexistence of convective and baroclinic zones. Hence, this experiment can be used as validator to study equilibrium processes as they occur in planetary atmospheres. For AtmoFlow the thermal boundaries are imposed by heating plates and cooling loops, which results in Dirichlet type boundary conditions as depicted in Fig. 30. Convection is controlled by varying the temperature at the outer shell. Dielectric heating does not change the temperature at the boundaries as it acts only on the fluid in the spherical gap and not in the cooling loops. The temperatures at the boundaries are controlled by thermal sensors.

7.4 Numerical results

Accompanying numerical simulations are performed for the AtmoFlow experiment. They are used to reconstruct the velocity field, which is not accessible by measurement techniques used in AtmoFlow. The reconstruction is based on a comparison of experimental and numerical interferograms. Matching structures in both interferograms correlate with similar temperature and velocity fields. Based on this assumption, the three-dimensional fluid flow gets accessible. However, drift velocities of convective structures are used to support the comparison. Drift rates are calculated directly from interferograms by identifying markers and slowly moving convection cells. They have to be identical in the numerical simulations and in the experiment. In principle, the parameter range of AtmoFlow can be captured by direct numerical simulations. However, they cannot replace the experiment. This is based on the thermo-EHD model, which has still many open questions, [62]. It is e.g. unclear if the Boussinesq approximation is valid for dielectrophoretic driven convection, when temperature differences exceed 3 K. Additionally, dielectric heating has been identified as important term in the model, which is under active research. AtmoFlow shall be used as validator for physical models of EHD regarding convection and internal heating.

The governing equations are solved numerically with the finite volume method (FVM) using the open source

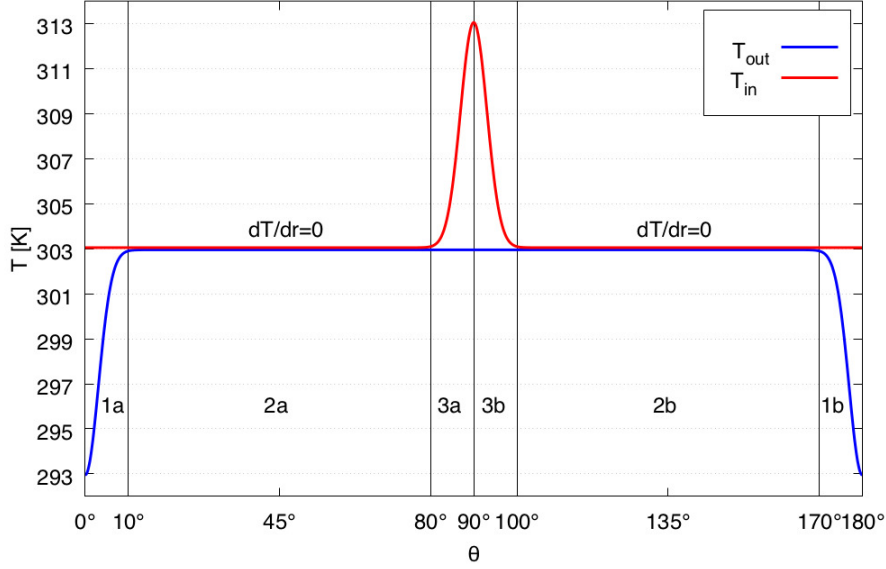


Figure 30: Simplified boundary conditions used for the numerical simulations of the AtmoFlow experiment for a maximum temperature difference of $\Delta T = 20$ K. T_{in} specifies the temperature at the inner shell, T_{out} at the outer shell.

software suite OpenFOAM, [96]. A cubed spherical grid with 4×10^6 cells is used for all simulations, where the radial resolution is 60 cells. The velocity boundary conditions are kept no-slip. The thermal boundaries are of Dirichlet type. The code solves the governing equations dimensionally in 3D with the PIMPLE algorithm. This algorithm is based on the SIMPLE approach for the solution of incompressible flows, but iterates the pressure loop several times to increase the precision of the solution. The time integration is performed with an implicit Crank-Nicolson method, the space derivatives are approximated in second order. Turbulent cases in the high Rayleigh number regime are modeled with the one-equation turbulence model 'dynamic-k'. The accuracy of the results is guaranteed by the velocity residual of $< 10^{-6}$.

In the following, three representative simulations with a temperature difference of 20 K between the equator and the poles are presented. The high voltage is set to $V_{rms} = 2800$ V in all cases. Additionally, all fluid properties are interpolated from the fluid's data sheet and temperature dependent. Here, the maximum electric gravity $\mathbf{g}_E = 1.2$ m/s² is found at the inner sphere and the minimum $\mathbf{g}_E = 0.2$ m/s² at the outer sphere. The corresponding Rayleigh number is $L = 1.9 \times 10^6$. Rotation is applied in the solid-body rotation case with a rate of $\Omega_1 = \Omega_2 = 0.8$ Hz. In case of differential rotation the inner shell rotates with $\Omega_1 = 0.88$ Hz and the outer shell with $\Omega_2 = 0.8$ Hz, respectively. This results in $Ta = 3.2 \times 10^6$ and $Ro = 0.1$. Hammer-Aitoff projections are calculated using the interpolation program TOMS661([72]). Hereby, the block-structured grid of OpenFOAM in Cartesian coordinates is interpolated onto a grid in spherical coordinates with the same amount of data points. For reasons of visibility the temperature and radial velocity are averaged along the radius. The artificial interferograms are calculated by superimposing two orthogonal interferograms, one in x-direction and one in the z-axis, respectively. The intensity I of the interferograms is calculated with fluid properties of the working fluid and specifications of the optical path which have been used for GeoFlow.

Non-rotating case

The non-rotation case is depicted in Figs. 31. Besides the equatorial up-welling region and the polar down-welling plumes, the overall temperature field is dominated by small, local plumes. These plumes are spread in a band-like structure along the latitudes. The Hammer-Aitoff projection Fig. 31 (a) and especially the thermal contour lines of the radially averaged temperature highlight this global cell formation. Interestingly, the numerical interferogram in Fig. 31 (b) shows these plumes as alined 'string of pearls' structure. A closer

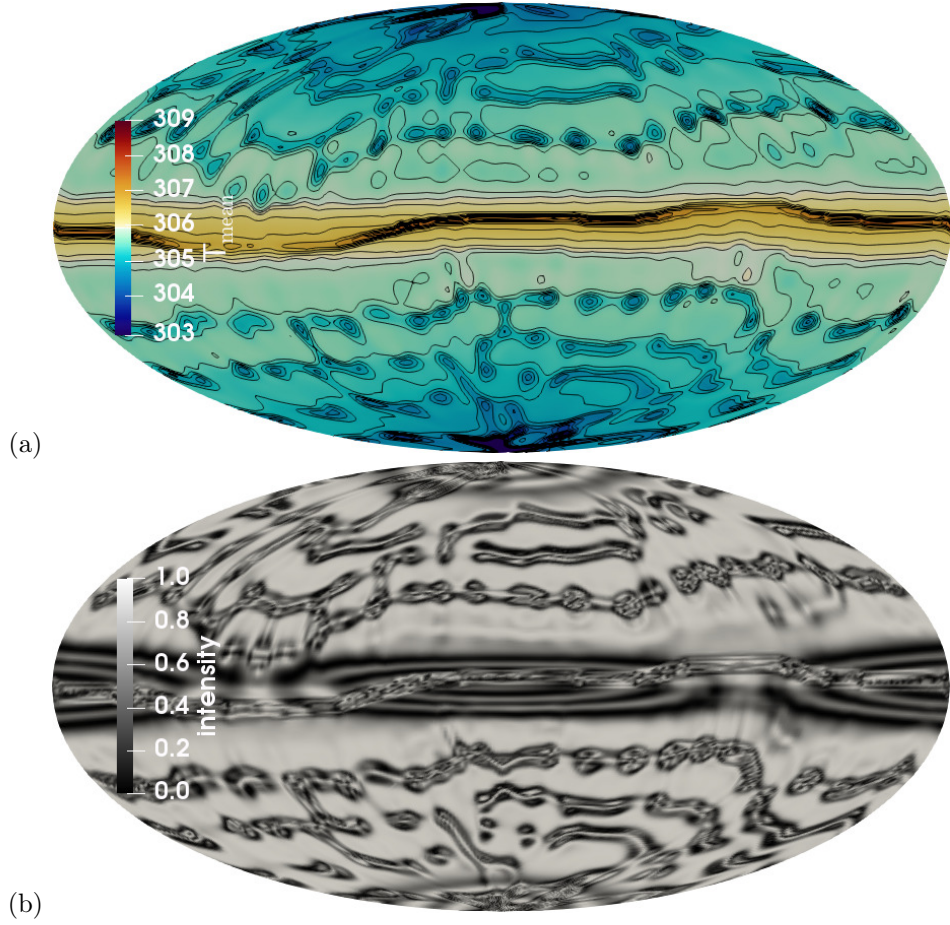


Figure 31: Numerical simulations of the non-rotation case at time stamp $t=5650$ sec (\sim three thermal time scales) for $L = 1.9 \times 10^6$: (a) radially averaged temperature field as Hammer-Aitoff projection, (b) superposition of two orthogonal artificial interferograms.

look on the velocity field (not depicted) shows many small vortices spread irregularly over both hemispheres. The only up-welling region is found around the equator. This results in a well mixed temperature field with low gradients.

Solid body rotation case

Fig. 32 depicts a representative solid body rotation case. This case reveals new fluid structures, which are based on rotational effects. The overall temperature distribution is dominated by broad up-welling and down-welling regions at the equator and the poles, respectively. However, in contrast to the non-rotating case only a few large vortices are visible. Local plumes are not found, except in the polar region. The equatorial region reveals a dominant planetary wave with mode $m=9$. This wave is visible in the velocity field, the Hammer-Aitoff projection and in the interferogram, too. Hence, this specific simulation can be used as benchmark test for the comparison between the numerical model and the experiment. The poles are characterized by cold fronts reaching deep into the mid-latitudes. These 'fingers' are not symmetrically arranged over both hemispheres, which emphasize the time-dependent and turbulent character of this fluid flow. The interferogram shown in Fig. 32 (b) reveals all mentioned flow structures. Concentric rings at the poles indicate the polar plumes and cold fronts are clearly visible as fringes, too. The equatorial wave can be identified clearly in distorted fringes.

Differential rotation case

Fig. 33 depicts the case when the inner shell rotates 40% faster than the outer shell. For inner shell rotation $\Omega_1 = 0.278 Hz$ and outer shell rotation $\Omega_2 = 0.2 Hz$ the Rossby number is $Ro = 0.72$. The temperature

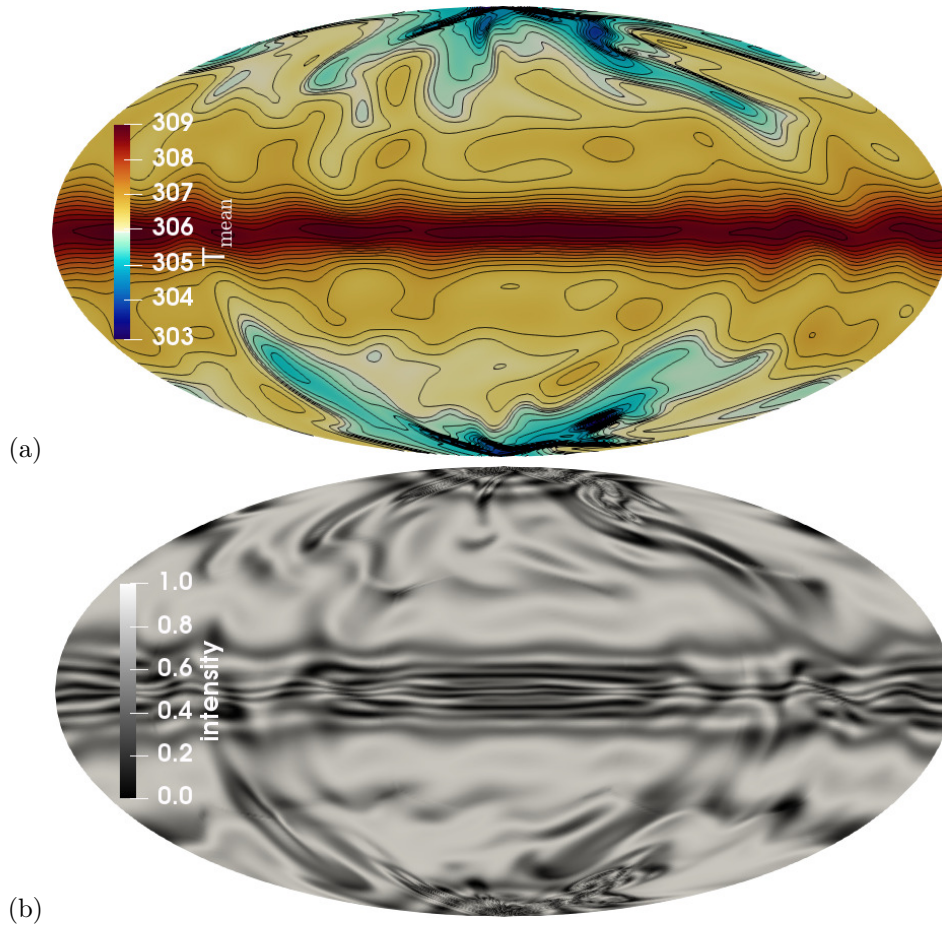


Figure 32: Numerical simulations of the solid body rotation case at time stamp $t=2180$ sec (\sim one thermal time scale) for $L = 1.9 \times 10^6$ and $Ta = 3.2 \times 10^6$: (a) radially averaged temperature field as Hammer-Aitoff projection, (b) superposition of two orthogonal artificial interferograms.

difference of $\Delta T = 0.2$ K and the low voltage if $V_{\text{rms}} = 2800$ V results in an electric Rayleigh number of $L = 19400$. Small temperature difference across the gap and low Taylor/Rossby numbers originate in band-like structures and zonal flows as known from gas giants. This specific structure is based on dielectric heating (see temperature legend in Fig. 33 (a)) which dominates the thermal distribution in the bulk. Strong convective flows, aligned with the rotation axis result from the internal heating process. Boundary driven convection is secondary and does not contribute much. The meridional velocity field shows two global thermal plumes in each hemisphere. Furthermore, the interferogram depicted in Fig. 33 (b) reveals these cells. One broad belt in the tropics and one narrow belt in the mid-latitudes.

Published and presented in:

P. Canfield, F. Zaussinger, C. Egbers, and P. Heintzmann. AtmoFlow - Simulating atmospheric flows on the International Space Station. Part I: Experiment and ISS-implementation concept. In 69th IAC conference proceedings, volume 18.A2.6.15-69. International Astronautical Federation, September 2018. URL <http://iafastro.directory/iac/archive/browse/IAC-18/A2/6/44307/>

F. Zaussinger, C. Egbers, P. Canfield, P. Haun, V. Travnikov, and A. Froitzheim. AtmoFlow - Experimental investigation of atmospheric flows under microgravity conditions. In EGU General Assembly Conference Abstracts, volume 20 of EGU General Assembly Conference Abstracts, page 6273, Feb. 2018. URL <https://meetingorganizer.copernicus.org/EGU2018/EGU2018-6273.pdf>

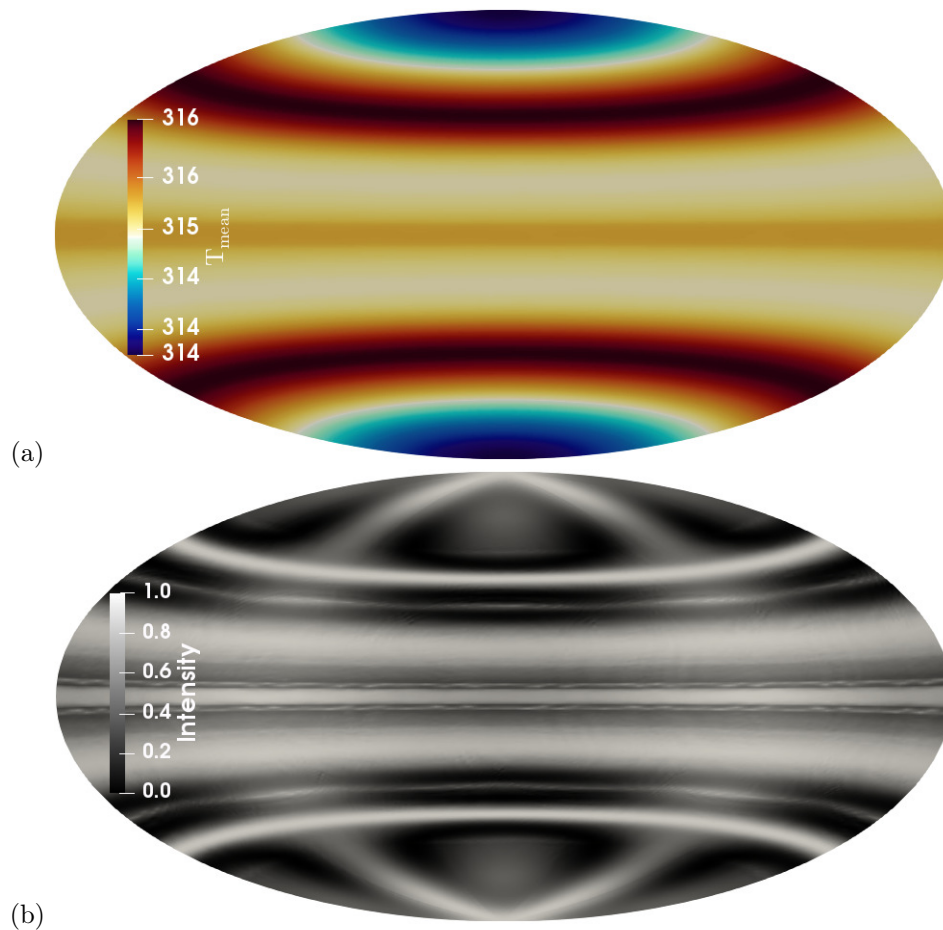


Figure 33: Numerical simulations of the differential rotation case at time stamp $t=420$ sec ($\sim 1/4$ thermal time scale) for $L = 1.9 \times 10^4$, $Ta = 3.8 \times 10^5$ and $Ro = 0.72$: (a) radially averaged temperature field as Hammer-Aitoff projection, (b) superposition of two orthogonal artificial interferograms.

C. Egbers, F. Zaussinger, P. Haun, P. Canfield, V. Travnikov, and A. Froitzheim. Convection in the spherical gap under micro-gravity conditions: From Earth's mantle to atmospheric flows. In 20th Int. Couette-Taylor Workshop. Aix Marseille universite, 2018. URL <https://ictw20.sciencesconf.org/data/pages/FinalProgramIV.pdf>

F. Zaussinger, C. Egbers, P. Canfield, P. Haun, V. Travnikov, A. Froitzheim, A. Meyer, and M. Meier. AtmoFlow - Investigation of atmospheric-like fluid flows under micro-gravity conditions. In EGU General Assembly Conference Abstracts, volume 21 of EGU General Assembly Conference Abstracts, page 8441, 2019. URL <https://meetingorganizer.copernicus.org/EGU2019/EGU2019-8441.pdf>

F. Zaussinger, P. Canfield, A. Froitzheim, V. Travnikov, P. Haun, M. Meier, A. Meyer, P. Heintzmann, T. Driebe, and C. Egbers. AtmoFlow - Investigation of atmospheric-like fluid flows under microgravity conditions. Microgravity Science and Technology, Jul 2019. doi: 10.1007/s12217-019-09717-7. URL <https://doi.org/10.1007/s12217-019-09717-7>

F. Zaussinger. AtmoFlow - Investigation of atmospheric-like fluid flows under micro-gravity conditions. In Book of Abstracts - ELGRA 2019, pages 55–56, 2019. URL <https://www.elgra2019.com/elgra2019bookofabstracts5/>

P. Szabo, F. Zaussinger, P. Haun, V. Travnikov, M. Meier, and C. Egbers. Complementary numerical and experimental study in the baroclinic annulus for the microgravity experiment AtmoFlow. In EGU General Assembly Conference Abstracts, EGU General Assembly Conference Abstracts, page 20956, 2020. URL <https://meetingorganizer.copernicus.org/EGU2020/EGU2020-20956.html>

8 Concluding remarks

The following concluding remarks are directly related to the research objectives presented in the introduction. However, detailed discussions and conclusions are found in the publications.

- *Modeling of EHD:* The validity of established models for EHD were critically evaluated in this research. In particular, the role of permittivity in the Gauss-equations was studied. Earlier models treated the permittivity as a constant factor in the Gauss equations and the well known r^{-5} dependency of the buoyancy term resulted. However, this approach inhibits thermo-electric feedback. This research reveals that thermo-electric feedback needs be taken into account to explain all studied aspects of EHD driven flows. Only in the case of pure boundary-driven convection at low Rayleigh numbers is it possible to use the stationary electric field. In particular, convection induced by dielectric heating needs non-constant permittivity for correct modeling of dielectrophoretic force.
- *Mixed heating:* This research brought many new findings in mixed heating convection. The extension of the governing equations by dielectric heating explained many patterns of most convective flows observed in the GeoFlow experiment. Global columnar cells, resulting from the Proudman-Taylor theorem, and all transitions from the conductive to the turbulent regime could be analyzed for the first time. In contrast to RB convection, the downdrafts and updrafts are not equally shaped due to non-linear electric gravity. Cold fluid is transported from the outer shell to the inner region in narrow channels at high velocity. The adverse transport results in broad regions of slow mass transport. This leads to differences in the heat transport between the inner and outer shell. Furthermore, the heat transport decreases at the inner shell with increasing voltage, which is explained by high dielectric losses. It is found that internal heating efficiently reduces convective heat transport. Hence, convective instability cannot be established throughout the bulk. This leads to separating flows, which are assumed in several EHD applications.
- *Rotation:* In contrast to other spherical shell experiments, the GeoFlow experiment provides a platform for investigating convection triggered by the dielectrophoretic effect with two heating sources; dielectric heating ($\lambda > 1$), caused by a fast alternating electric field and the temperature difference across the gap ($\lambda < 1$). Furthermore, it is the first study of rotating convection which includes both heating sources and a micro-gravity environment. Thus, GeoFlow was a unique experimental platform where various aspects of fluid dynamic could be studied. This led to the first observation of the existence of global columnar cells in a micro-gravity environment. Additionally, it was possible to apply rotating convection models to the EHD case. This means that EHD based experiments can indeed be used to study RB-like rotating convection.
- *Convection with viscosity contrast:* The original idea of GeoFlow II was the investigation of convective flows with a strong viscosity contrast which is assumed in the Earth's mantle. Therefore, the working fluid 1-Nonanol was used in the GeoFlow II experiment. This fluid provides a viscosity contrast of $\beta \approx 2$ for the given temperature difference of $\Delta T = 10 K$. Interestingly, the results of GeoFlow II differed in many aspects from GeoFlow I where M5 silicon oil was used. In particular, hysteresis effects were observed which could not be explained by the viscosity contrast alone. A deeper analysis of the working fluid yielded a high susceptibility to dielectric heating. This physical process acts as a volumetric heat source and changed the entire scientific focus of the experiment. With the knowledge of mixed convection, it was possible to explain most outcomes of the experiment. The GeoFlow II experiment is a much closer approximation to the Earth's mantle as initially assumed, where convection is likewise triggered by internal heating as well as the temperature difference across the boundaries.
- *Post-processing methods and numerics:* Several post-processing methods were presented. In particular, machine learning-based pattern recognition was shown to be a useful method to analyze fluid flows. The

reliable detection of convective patterns such as double-eye interferograms or sheet-like structures minimizes manual work. Furthermore, these methods provide a fast and lean implementation on any operating system. Therefore, it is planned to implement the presented pattern recognition algorithm directly on the ISS in the AtmoFlow experiment. In combination with higher statistical moments, the Geo/AtmoFlow software package provides a robust approach to analyze fluid flows without studying large 3D simulations. In particular, the skewness and kurtosis shed light on complex convective flows. Advanced visualization helps one to understand the fluid flow and make the complex interaction of convection, rotation and the electric field more transparent. Three numerical codes were developed during the Geo/Atmoflow research. These codes are designed for linear stability analysis, complex 3D simulations and high resolution EHD analysis in a rectangular geometry. All codes are validated with experimental data and provide a robust platform for future research.

- *Outlook:* AtmoFlow has been planned for long-term investigation of thermal convection in rotating spherical shells under the influence of a central force field with complex boundary conditions. This setup represents a simplified deep atmosphere as found in giant planets. The experiment consists of three main parts: a) two concentric spherical shells filled with the test liquid Novec 7200 and thermalized by atmospheric-like boundary conditions. b) a rotation tray with two perpendicular co-rotating visualization units, and c) a high voltage supply for the radial force field. The development of the AtmoFlow experiment benefits from the heritage of GeoFlow. However, it is more advanced in fluid flow visualization and in the parameter regime. The AtmoFlow experiment payload is currently in development for operation on the ISS. The launch is planned for 2024.

References

- [1] P. Allen and T. Karayiannis. Electrohydrodynamic enhancement of heat transfer and fluid flow. Heat Recovery Systems and CHP, 15(5):389 – 423, 1995. ISSN 0890-4332. doi: [https://doi.org/10.1016/0890-4332\(95\)90050-0](https://doi.org/10.1016/0890-4332(95)90050-0). URL <http://www.sciencedirect.com/science/article/pii/0890433295900500>.
- [2] S. F. Bart, L. S. Tavrow, M. Mehregany, and J. H. Lang. Microfabricated electrohydrodynamic pumps. Sensors and Actuators A: Physical, 21(1):193 – 197, 1990. ISSN 0924-4247. doi: [https://doi.org/10.1016/0924-4247\(90\)85037-5](https://doi.org/10.1016/0924-4247(90)85037-5). URL <http://www.sciencedirect.com/science/article/pii/0924424790850375>. Proceedings of the 5th International Conference on Solid-State Sensors and Actuators and Eurosensors III.
- [3] J. Bigun. Vision with Direction. Springer, 2006.
- [4] I. D. Borcia and U. Harlander. Inertial waves in a rotating annulus with inclined inner cylinder: comparing the spectrum of wave attractor frequency bands and the eigenspectrum in the limit of zero inclination. Theoretical and Computational Fluid Dynamics, 27(3):397–413, Jun 2013. ISSN 1432-2250. doi: 10.1007/s00162-012-0278-6. URL <https://doi.org/10.1007/s00162-012-0278-6>.
- [5] F. H. Busse. Thermal instabilities in rapidly rotating systems. Journal of Fluid Mechanics, 44(3):441–460, 1970. doi: 10.1017/S0022112070001921.
- [6] F. H. Busse and C. R. Carrigan. Laboratory simulation of thermal convection in rotating planets and stars. Science, 191(4222):81–83, 1976. ISSN 0036-8075. doi: 10.1126/science.191.4222.81. URL <http://science.sciencemag.org/content/191/4222/81>.
- [7] R. S. Busse F. H. Convection in rotating spherical fluid shells convection in rotating spherical fluid shells. 2009.
- [8] P. Canfield, F. Zaussinger, C. Egbers, and P. Heintzmann. AtmoFlow - Simulating atmospheric flows on the International Space Station. Part I: Experiment and ISS-implementation concept. In 69th IAC conference proceedings, volume 18.A2.6.15-69. International Astronautical Federation, September 2018. URL <http://iafastro.directory/iac/archive/browse/IAC-18/A2/6/44307/>.
- [9] A. Castellanos. Electrohydrodynamics, volume CISM courses and lectures-380. Springer-Verlag Wien GmbH, 1998.
- [10] S. C. Chan and S. Nigam. Residual diagnosis of diabatic heating from era-40 and ncep reanalyses: Intercomparisons with trmm. Journal of Climate, 22(2):414–428, 2009. doi: 10.1175/2008JCLI2417.1. URL <https://doi.org/10.1175/2008JCLI2417.1>.
- [11] B. Chandra and D. E. Smylie. A laboratory model of thermal convection under a central force field. Geophysical Fluid Dynamics, 3(1):211–224, 1972. doi: 10.1080/03091927208236081. URL <https://doi.org/10.1080/03091927208236081>.
- [12] U. R. Christensen. Zonal flow driven by deep convection in the major planets. Geophysical Research Letters, 28(13):2553–2556, 2019/04/30 2001. doi: 10.1029/2000GL012643. URL <https://doi.org/10.1029/2000GL012643>.
- [13] J. Curbelo, J. M. Lopez, A. M. Mancho, and F. Marques. Confined rotating convection with large prandtl number: Centrifugal effects on wall modes. Phys. Rev. E, 89:013019, Jan 2014. doi: 10.1103/PhysRevE.89.013019. URL <https://link.aps.org/doi/10.1103/PhysRevE.89.013019>.
- [14] D. D. Bercovivi. Three-dimensional thermal convection in a spherical shell. J. Fluid Mech., 206:75–104, 1989.

- [15] W. Dietrich, T. Gastine, and J. Wicht. Reversal and amplification of zonal flows by boundary enforced thermal wind. *Icarus*, 282:380 – 392, 2017. ISSN 0019-1035. doi: <https://doi.org/10.1016/j.icarus.2016.09.013>. URL <http://www.sciencedirect.com/science/article/pii/S0019103516305759>.
- [16] O. Dupont, T. Dewandre, J.-L. Dewandel, and D. Claessens. The optical diagnostics of the fluid science laboratory. In *Proc. of the 5th int. conference on space optics*, pages 463–469, 2004.
- [17] C. Egbers, W. Brasch, B. Sitte, J. Immohr, and J.-R. Schmidt. Estimates on diagnostic methods for investigations of thermal convection between spherical shells in space. *Measurement Science and Technology*, 10(10):866–877, sep 1999. doi: 10.1088/0957-0233/10/10/306.
- [18] C. Egbers, W. Beyer, A. Bonhage, R. Hollerbach, and P. Beltrame. The GeoFlow-experiment on ISS (part I): Experimental preparation and design of laboratory testing hardware. *Advances in Space Research*, 32(2):171 – 180, 2003. ISSN 0273-1177. doi: [http://dx.doi.org/10.1016/S0273-1177\(03\)90248-1](http://dx.doi.org/10.1016/S0273-1177(03)90248-1). URL <http://www.sciencedirect.com/science/article/pii/S0273117703902481>. Gravitational Effects in Physico-Chemical Processes.
- [19] C. Egbers, F. Zaussinger, P. Haun, P. Canfield, V. Travnikov, and A. Froitzheim. Convection in the spherical gap under micro-gravity conditions: From Earths mantle to atmospheric flows. In *20th Int. Couette-Taylor Workshop*. Aix Marseille universite, 2018. URL <https://ictw20.sciencesconf.org/data/pages/FinalProgramIV.pdf>.
- [20] A. O. El Moctar, N. Aubry, and J. Batton. Electro-hydrodynamic micro-fluidic mixer. *Lab Chip*, 3: 273–280, 2003. doi: 10.1039/B306868B. URL <http://dx.doi.org/10.1039/B306868B>.
- [21] S. P. Evgenidis, K. A. Zacharias, T. D. Karapantsios, and M. Kostoglou. Effect of liquid properties on heat transfer from miniature heaters at different gravity conditions. *Microgravity Science and Technology*, 23(2):123–128, Feb 2011. ISSN 1875-0494. doi: 10.1007/s12217-010-9206-9. URL <https://doi.org/10.1007/s12217-010-9206-9>.
- [22] F. Feudel, K. Bergemann, L. S. Tuckerman, C. Egbers, B. Futterer, M. Gellert, and R. Hollerbach. Convection patterns in a spherical fluid shell. *Physical Review E*, 83(4):046304, Apr 2011. ISSN 1550-2376. doi: 10.1103/physreve.83.046304. URL <http://dx.doi.org/10.1103/PhysRevE.83.046304>.
- [23] F. Feudel, N. Seehafer, L. S. Tuckerman, and M. Gellert. Multistability in rotating spherical shell convection. *Physical Review E*, 87(2), Feb 2013. ISSN 1550-2376. doi: 10.1103/physreve.87.023021. URL <http://dx.doi.org/10.1103/PhysRevE.87.023021>.
- [24] F. Feudel, L. Tuckerman, M. Gellert, and N. Seehafer. Bifurcations of rotating waves in rotating spherical shell convection. *Phys. Rev. E*, 92(053015), 2015.
- [25] M. T. Fogaing, H. N. Yoshikawa, O. Crumeyrolle, and I. Mutabazi. Heat transfer in the thermo-electrohydrodynamic convection under microgravity conditions. *The European Physical Journal E*, 37(4):1–6, Apr 2014. ISSN 1292-895X. doi: 10.1140/epje/i2014-14035-0. URL <http://dx.doi.org/10.1140/epje/i2014-14035-0>.
- [26] W.-G. Früh. Using magnetic fluids to simulate convection in a central force field in the laboratory. *Nonlinear Processes in Geophysics*, 12(6):877–889, 2005.
- [27] B. Futterer, **Zaussinger, F.**, C. Egbers, and N. Scurtu. Variation of viscosity contrast for convection experiments in spherical shells as part of geophysical flow simulation experiment GeoFlow II. In *EGU General Assembly Conference Abstracts*, volume 13 of *EGU General Assembly Conference Abstracts*, page 5562, 2011.

- [28] B. Futterer, A. Krebs, A.-C. Plesa, F. Zaussinger, R. Hollerbach, D. Breuer, and C. Egbers. Sheet-like and plume-like thermal flow in a spherical convection experiment performed under microgravity. Journal of Fluid Mechanics, 735:647–683, 2013. doi: 10.1017/jfm.2013.507.
- [29] B. Futterer, F. Zaussinger, A.-C. Plesa, A. Krebs, C. Egbers, and D. Breuer. Sheet-like and plume-like thermal flow in a spherical convection experiment with high viscosity contrast. In EGU General Assembly Conference Abstracts, volume 15 of EGU General Assembly Conference Abstracts, pages EGU2013–4830, Apr. 2013.
- [30] B. Futterer, N. Dahley, and C. Egbers. Thermal electro-hydrodynamic heat transfer augmentation in vertical annuli by the use of dielectrophoretic forces through a.c. electric field. International Journal of Heat and Mass Transfer, 93:144 – 154, 2016. ISSN 0017-9310. doi: <https://doi.org/10.1016/j.ijheatmasstransfer.2015.10.005>. URL <http://www.sciencedirect.com/science/article/pii/S0017931015010030>.
- [31] C. Gabriel, S. Gabriel, E. H. Grant, E. H. Grant, B. S. J. Halstead, and D. Michael P. Mingos. Dielectric parameters relevant to microwave dielectric heating. Chem. Soc. Rev., 27:213–224, 1998. doi: 10.1039/A827213Z. URL <http://dx.doi.org/10.1039/A827213Z>.
- [32] P. Galliker, J. Schneider, H. Eghlidi, S. Kress, V. Sandoghdar, and D. Poulikakos. Direct printing of nanostructures by electrostatic autofocussing of ink nanodroplets. Nature Communications, 3:890 EP –, 06 2012. URL <https://doi.org/10.1038/ncomms1891>.
- [33] P. R. C. Gascoyne and J. Vykoukal. Particle separation by dielectrophoresis. ELECTROPHORESIS, 23(13):1973–1983, 2002. doi: 10.1002/1522-2683(200207)23:13<1973::AID-ELPS1973>3.0.CO;2-1.
- [34] T. Gastine, J. Wicht, and J. Aurnou. Zonal flow regimes in rotating anelastic spherical shells: An application to giant planets. Icarus, 225(1):156 – 172, 2013. ISSN 0019-1035. doi: <https://doi.org/10.1016/j.icarus.2013.02.031>. URL <http://www.sciencedirect.com/science/article/pii/S001910351300119X>.
- [35] T. Gastine, R. K. Yadav, J. Morin, A. Reiners, and J. Wicht. From solar-like to antisolar differential rotation in cool stars. Monthly Notices of the Royal Astronomical Society: Letters, 438(1):L76–L80, 12 2013. ISSN 1745-3925. doi: 10.1093/mnrasl/slt162. URL <https://doi.org/10.1093/mnrasl/slt162>.
- [36] T. Gastine, J. Wicht, and J. M. Aurnou. Turbulent rayleigh–bénard convection in spherical shells. Journal of Fluid Mechanics, 778:721–764, Aug 2015. ISSN 1469-7645. doi: 10.1017/jfm.2015.401. URL <http://dx.doi.org/10.1017/jfm.2015.401>.
- [37] T. Gastine, J. Wicht, and J. Aubert. Scaling regimes in spherical shell rotating convection. Journal of Fluid Mechanics, 808:690–732, Nov 2016. ISSN 1469-7645. doi: 10.1017/jfm.2016.659. URL <http://dx.doi.org/10.1017/jfm.2016.659>.
- [38] J. C. H. Pohl, K. Pollock. Dielectrophoretic force: a comparison of theory and experiment. Physical Biological Sciences, 1979.
- [39] J. E. Hart, G. A. Glatzmaier, and J. Toomre. Space-laboratory and numerical simulations of thermal convection in a rotating hemispherical shell with radial gravity. Journal of Fluid Mechanics, 173:519–544, Dec 1986. doi: 10.1017/S0022112086001258. URL <https://www.cambridge.org/core/article/div-class-title-space-laboratory-and-numerical-simulations-of-thermal-convection-in-a-rotating-hemispherical-shell-with-radial-gravity-div/E5DC65212D6332D9720933F64AC208D4>.
- [40] M. Heimpel, J. Aurnou, and J. Wicht. Simulation of equatorial and high-latitude jets on jupiter in a deep convection model. Nature, 438(7065):193–196, 2005. doi: 10.1038/nature04208. URL <https://doi.org/10.1038/nature04208>.

- [41] R. Hollerbach. A spectral solution of the magneto-convection equations in spherical geometry. International Journal for Numerical Methods in Fluids, 32(7):773–797, 2000. ISSN 1097-0363. doi: 10.1002/(SICI)1097-0363(20000415)32:7<773::AID-FLD988>3.0.CO;2-P. URL [http://dx.doi.org/10.1002/\(SICI\)1097-0363\(20000415\)32:7<773::AID-FLD988>3.0.CO;2-P](http://dx.doi.org/10.1002/(SICI)1097-0363(20000415)32:7<773::AID-FLD988>3.0.CO;2-P).
- [42] R. Hollerbach, R. J. Wiener, I. S. Sullivan, R. J. Donnelly, and C. F. Barenghi. The flow around a torsionally oscillating sphere. Physics of Fluids, 14(12):4192–4205, 2002. doi: 10.1063/1.1518029. URL <https://doi.org/10.1063/1.1518029>.
- [43] J. Immohr. Sphärische Differentialinterferometrie für Raumfahrtanwendungen — Konvektionsströmungen im Kugelspalt unter dem Einfluss axialer und radialer Kraftwirkung. PhD thesis, Universität Bremen, 2005.
- [44] T. Jones. Electrohydrodynamically enhanced heat transfer in liquids—a review. volume 14 of Advances in Heat Transfer, pages 107 – 148. Elsevier, 1979. doi: [https://doi.org/10.1016/S0065-2717\(08\)70086-8](https://doi.org/10.1016/S0065-2717(08)70086-8). URL <http://www.sciencedirect.com/science/article/pii/S0065271708700868>.
- [45] K. Julien, A. M. Rubio, I. Grooms, and E. Knobloch. Statistical and physical balances in low rossby number rayleigh–bénard convection. Geophysical & Astrophysical Fluid Dynamics, 106(4-5):392–428, 08 2012. doi: 10.1080/03091929.2012.696109. URL <https://doi.org/10.1080/03091929.2012.696109>.
- [46] D. H. Kelley, S. A. Triana, D. S. Zimmerman, and D. P. Lathrop. Selection of inertial modes in spherical couette flow. Phys Rev E Stat Nonlin Soft Matter Phys, 81(2 Pt 2):026311, Feb 2010. ISSN 1550-2376 (Electronic); 1539-3755 (Linking). doi: 10.1103/PhysRevE.81.026311.
- [47] S. Khan, Y. H. Doh, A. Khan, A. Rahman, K. H. Choi, and D. S. Kim. Direct patterning and electro spray deposition through ehd for fabrication of printed thin film transistors. Current Applied Physics, 11(1, Supplement):S271 – S279, 2011. ISSN 1567-1739. doi: <https://doi.org/10.1016/j.cap.2010.11.044>. URL <http://www.sciencedirect.com/science/article/pii/S1567173910004062>. International Conference on Electronic Materials.
- [48] R. Kuhl, M. Roth, H. Binnenbruck, W. Dreier, R. Forke, and P. Preu. The role of sounding rocket microgravity experiments within the German Physical Sciences Programme. In B. Warmbein, editor, 17th ESA Symposium on European Rocket and Balloon Programmes and Related Research, volume 590 of ESA Special Publication, pages 503–508, Aug. 2005.
- [49] F. Kupka, M. Losch, F. Zaussinger, and T. Zweigle. Semi-convection in the ocean and in stars: A multi-scale analysis. Meteorologische Zeitschrift, 24(3):343–358, 2015. doi: 10.1127/metz/2015/0643.
- [50] F. Kupka, F. Zaussinger, and M. H. Montgomery. Mixing and overshooting in surface convection zones of DA white dwarfs: First results from ANTARES. Monthly Notices of the Royal Astronomical Society, 474(4):4660–4671, 2018. doi: 10.1093/mnras/stx3119.
- [51] S. Laohalertdecha, P. Naphon, and S. Wongwises. A review of electrohydrodynamic enhancement of heat transfer. Renewable and Sustainable Energy Reviews, 11:858–876, 06 2007. doi: 10.1016/j.rser.2005.07.002.
- [52] T. H. v. Larcher, B. Futterer, and C. Egbers. Geoflow: On the status of experimental preparation of spherical gap flow experiments with central force field on international space station (iss). Journal of Physics: Conference Series, 137:012025, Nov 2008. ISSN 1742-6596. doi: 10.1088/1742-6596/137/1/012025. URL <http://dx.doi.org/10.1088/1742-6596/137/1/012025>.
- [53] M. Liu, C. Egbers, A. Delgado, and H. Rath. Investigation of density driven large-scale ocean motion under microgravity. In H. J. Rath, editor, Microgravity Fluid Mechanics, pages 573–581, Berlin, Heidelberg, 1992. Springer Berlin Heidelberg. ISBN 978-3-642-50091-6.

- [54] M. A. Lotto, K. M. Johnson, C. W. Nie, and D. M. Klaus. The impact of reduced gravity on free convective heat transfer from a finite, flat, vertical plate. Microgravity Science and Technology, 29(5):371–379, Oct 2017. ISSN 1875-0494. doi: 10.1007/s12217-017-9555-8. URL <https://doi.org/10.1007/s12217-017-9555-8>.
- [55] A. Maeder. On the Richardson criterion for shear instabilities in rotating stars. Astronomy and Astrophysics, 299:84, July 1995.
- [56] C. K. Mamun and L. S. Tuckerman. Asymmetry and hopf bifurcation in spherical couette flow. Physics of Fluids, 7(1):80–91, 1995. doi: 10.1063/1.868730. URL <https://doi.org/10.1063/1.868730>.
- [57] J.-B. Manneville and P. Olson. Banded convection in rotating fluid spheres and the circulation of the Jovian atmosphere. Icarus, 122(2):242 – 250, 1996. ISSN 0019-1035. doi: <https://doi.org/10.1006/icar.1996.0123>. URL <http://www.sciencedirect.com/science/article/pii/S0019103596901232>.
- [58] M. Meier, M. Jongmanns, A. Meyer, T. Seelig, C. Egbers, and I. Mutabazi. Flow pattern and heat transfer in a cylindrical annulus under 1 g and low-g conditions: Experiments. Microgravity Science and Technology, 30(5):699–712, Oct 2018. ISSN 1875-0494. doi: 10.1007/s12217-018-9649-y. URL <https://doi.org/10.1007/s12217-018-9649-y>.
- [59] J. R. Melcher. Continuum electromechanics. Cambridge, Mass: MIT Press. MIT Press, 1981.
- [60] A. Meyer, M. Jongmanns, M. Meier, C. Egbers, and I. Mutabazi. Thermal convection in a cylindrical annulus under a combined effect of the radial and vertical gravity. Comptes Rendus Mécanique, 345(1):11 – 20, 2017. ISSN 1631-0721. doi: <https://doi.org/10.1016/j.crme.2016.10.003>. URL <http://www.sciencedirect.com/science/article/pii/S1631072116301000>. Basic and applied researches in microgravity – A tribute to Bernard Zappoli’s contribution.
- [61] A. Meyer, O. Crumeyrolle, I. Mutabazi, M. Meier, M. Jongmanns, M.-C. Renoult, T. Seelig, and C. Egbers. Flow patterns and heat transfer in a cylindrical annulus under 1g and low-g conditions: Theory and simulation. Microgravity Science and Technology, 30(5):653–662, Oct 2018. ISSN 1875-0494. doi: 10.1007/s12217-018-9636-3. URL <https://doi.org/10.1007/s12217-018-9636-3>.
- [62] I. Mutabazi, H. N. Yoshikawa, M. T. Fogaing, V. Travnikov, O. Crumeyrolle, B. Futterer, and C. Egbers. Thermo-electro-hydrodynamic convection under microgravity: a review. Fluid Dynamics Research, 48(6): 061413, 2016. URL <http://stacks.iop.org/1873-7005/48/i=6/a=061413>.
- [63] V. D. Nguyen and D. Byun. Mechanism of electrohydrodynamic printing based on ac voltage without a nozzle electrode. Applied Physics Letters, 94(17):173509, 2009. doi: 10.1063/1.3126957. URL <https://doi.org/10.1063/1.3126957>.
- [64] A. Nordlund, R. Stein, and M. Asplund. Solar surface convection. Living Rev. Solar Phys., 6(2), 2009.
- [65] M. Ogawa. Mantle convection: A review. Fluid Dynamics Research, 40(6):379, 2008.
- [66] D. R. Ohlsen and P. B. Rhines. Laboratory studies of equatorially trapped waves using ferrofluid. Journal of Fluid Mechanics, 338:35–58, 1997. doi: 10.1017/S0022112096004776.
- [67] J.-U. Park, M. Hardy, S. J. Kang, K. Barton, K. Adair, D. k. Mukhopadhyay, C. Y. Lee, M. S. Strano, A. G. Alleyne, J. G. Georgiadis, P. M. Ferreira, and J. A. Rogers. High-resolution electrohydrodynamic jet printing. Nature Materials, 6:782 EP –, 08 2007. URL <https://doi.org/10.1038/nmat1974>.
- [68] J. Paschkewitz and D. Pratt. The influence of fluid properties on electrohydrodynamic heat transfer enhancement in liquids under viscous and electrically dominated flow conditions. Experimental Thermal and Fluid Science, 21:187–197, 05 2000. doi: 10.1016/S0894-1777(00)00002-9.

- [69] H. Pohl. Dielectrophoresis. Cambridge University Press, 1978.
- [70] A. A. Ramadhan, N. Kapur, J. Summers, and H. Thompson. Numerical development of ehd cooling systems for laptop applications. Applied Thermal Engineering, 139:144 – 156, 2018. ISSN 1359-4311. doi: <https://doi.org/10.1016/j.applthermaleng.2018.04.119>. URL <http://www.sciencedirect.com/science/article/pii/S1359431117379383>.
- [71] P. L. Read, Y. H. Yamazaki, S. R. Lewis, P. D. Williams, K. Miki-Yamazaki, J. Sommeria, H. Didelle, and A. Fincham. Jupiter’s and saturn’s convectively driven banded jets in the laboratory. Geophysical Research Letters, 31(22), 2019/04/30 2004. doi: 10.1029/2004GL020106. URL <https://doi.org/10.1029/2004GL020106>.
- [72] R. J. Renka. Algorithm 660: Qshep2d: Quadratic shepard method for bivariate interpolation of scattered data. ACM Trans. Math. Softw., 14(2):149–150, June 1988. ISSN 0098-3500. doi: 10.1145/45054.356231. URL <http://doi.acm.org/10.1145/45054.356231>.
- [73] M. Rieutord, S. A. Triana, D. S. Zimmerman, and D. P. Lathrop. Excitation of inertial modes in an experimental spherical couette flow. Phys Rev E Stat Nonlin Soft Matter Phys, 86(2 Pt 2):026304, Aug 2012. ISSN 1550-2376 (Electronic); 1539-3755 (Linking). doi: 10.1103/PhysRevE.86.026304.
- [74] P. H. Roberts. Electrohydrodynamic Convection. The Quarterly Journal of Mechanics and Applied Mathematics, 22(2):211–220, 05 1969. ISSN 0033-5614. doi: 10.1093/qjmam/22.2.211. URL <https://doi.org/10.1093/qjmam/22.2.211>.
- [75] J. D. Scheel and J. Schumacher. Global and local statistics in turbulent convection at low prandtl numbers. Journal of Fluid Mechanics, 802:147–173, 2016. doi: 10.1017/jfm.2016.457.
- [76] G. Schubert and D. Bercovivi. Treatise on Geophysics, volume 7 Mantle Dynamics. Elsevier, 2009.
- [77] G. Schubert, D. Turcotte, and P. Olson. Mantle Convection in the Earth and Planets. Cambridge University Press, 2001. ISBN 9780521798365.
- [78] H. Socolan and P. L. Read. A rotating annulus driven by localized convective forcing: a new atmosphere-like experiment. Experiments in Fluids, 58(6), May 2017. ISSN 1432-1114. doi: 10.1007/s00348-017-2347-5. URL <http://dx.doi.org/10.1007/s00348-017-2347-5>.
- [79] T. Seelig, A. Meyer, P. Gerstner, M. Meier, M. Jongmanns, M. Baumann, V. Heuveline, and C. Egbers. Dielectrophoretic force-driven convection in annular geometry under earth’s gravity. International Journal of Heat and Mass Transfer, 139:386–398, 2019. doi: <https://doi.org/10.1016/j.ijheatmasstransfer.2019.04.068>. URL <http://www.sciencedirect.com/science/article/pii/S0017931018361854>.
- [80] B. Sitte. Thermische Konvektion in Zentralkraftfeldern. PhD thesis, Universität Bremen, 2004.
- [81] B. Sitte and H. Rath. Influence of the dielectrophoretic force on thermal convection. Experiments in Fluids, 34(1):24–27, 2003. doi: 10.1007/s00348-002-0524-6. URL <https://doi.org/10.1007/s00348-002-0524-6>.
- [82] B. L. Smorodin. The effect of an alternating electric field on the liquid dielectric convection in a horizontal capacitor. Technical Physics Letters, 27(12):1062–1064, Dec 2001. ISSN 1090-6533. doi: 10.1134/1.1432371. URL <https://doi.org/10.1134/1.1432371>.
- [83] H. Songoro. Electrohydrodynamic Modeling of Droplet Vibrations under the Influence of Electric Fields. PhD thesis, Technische Universität, Darmstadt, March 2015. URL <http://tuprints.ulb.tu-darmstadt.de/4471/>.

- [84] P. J. Stiles. Electro-thermal convection in dielectric liquids. Chemical Physics Letters, 179(3): 311 – 315, 1991. ISSN 0009-2614. URL <http://www.sciencedirect.com/science/article/pii/000926149187043B>.
- [85] P. J. Stiles, F. Lin, and P. J. Blennerhassett. Convective heat transfer through polarized dielectric liquids. Physics of Fluids A: Fluid Dynamics, 5(12):3273–3279, 1993.
- [86] P. Szabo, F. Zaussinger, P. Haun, V. Travnikov, M. Meier, and C. Egbers. Complementary numerical and experimental study in the baroclinic annulus for the microgravity experiment AtmoFlow. In EGU General Assembly Conference Abstracts, EGU General Assembly Conference Abstracts, page 20956, 2020. URL <https://meetingorganizer.copernicus.org/EGU2020/EGU2020-20956.html>.
- [87] V. Travnikov, C. Egbers, and R. Hollerbach. The Geoflow-experiment on ISS (Part II): Numerical simulation. Advances in Space Research, 32(2):181 – 189, 2003. ISSN 0273-1177. doi: [http://dx.doi.org/10.1016/S0273-1177\(03\)90249-3](http://dx.doi.org/10.1016/S0273-1177(03)90249-3). URL <http://www.sciencedirect.com/science/article/pii/S0273117703902493>. Gravitational Effects in Physico-Chemical Processes.
- [88] V. Travnikov, F. Zaussinger, P. Beltrame, and C. Egbers. Influence of the temperature-dependent viscosity on convective flow in the radial force field. Phys. Rev. E, 96:023108, Aug 2017. doi: 10.1103/PhysRevE.96.023108. URL <https://link.aps.org/doi/10.1103/PhysRevE.96.023108>.
- [89] V. Travnikov, F. Zaussinger, P. Haun, and C. Egbers. Influence of dielectrical heating on convective flow in a radial force field. Phys. Rev. E, 101:053106, May 2020. doi: 10.1103/PhysRevE.101.053106. URL <https://link.aps.org/doi/10.1103/PhysRevE.101.053106>.
- [90] R. J. Turnbull. Effect of dielectrophoretic forces on the Bénard instability. The Physics of Fluids, 12(9):1809–1815, 1969. doi: 10.1063/1.1692745. URL <https://aip.scitation.org/doi/abs/10.1063/1.1692745>.
- [91] K. Vilella and F. Deschamps. Temperature and heat flux scaling laws for isoviscous, infinite Prandtl number mixed heating convection. Geophysical Journal International, 214(1):265–281, 04 2018. ISSN 0956-540X. doi: 10.1093/gji/ggy138. URL <https://dx.doi.org/10.1093/gji/ggy138>.
- [92] M. Vincze, S. Borchert, U. Achatz, T. von Larcher, M. Baumann, C. Liersch, S. Remmler, T. Beck, K. D. Alexandrov, C. Egbers, J. Fröhlich, V. Heuveline, S. Hickel, and U. Harlander. Benchmarking in a rotating annulus: a comparative experimental and numerical study of baroclinic wave dynamics. Meteorologische Zeitschrift, 23(6):611–635, 01 2015. doi: 10.1127/metz/2014/0600. URL <http://dx.doi.org/10.1127/metz/2014/0600>.
- [93] S. V. Vorontsov, J. Christensen-Dalsgaard, J. Schou, V. N. Strakhov, and M. J. Thompson. Helioseismic measurement of solar torsional oscillations. Science, 296(5565):101–103, 2002. ISSN 0036-8075. doi: 10.1126/science.1069190. URL <https://science.sciencemag.org/content/296/5565/101>.
- [94] Y. Wang and P. Read. Diversity of planetary atmospheric circulations and climates in a simplified general circulation model. Proceedings IAU Symposium, 8(S293):297–302, 2012. doi: DOI:10.1017/S1743921313013033. URL <https://www.cambridge.org/core/article/diversity-of-planetary-atmospheric-circulations-and-climates-in-a-simplified-general-circulation-model/F06958904E99B92B8B9B208A3E630E0B>.
- [95] L. Waszek, J. Irving, and A. Deuss. Reconciling the hemispherical structure of earth’s inner core with its super-rotation. Nature Geoscience, 4:264 EP –, 02 2011. URL <https://doi.org/10.1038/ngeo1083>.
- [96] H. G. Weller, G. Tabor, H. Jasak, and C. Fureby. A tensorial approach to computational continuum mechanics using object-oriented techniques. Computers in Physics, 12:620–631, Nov. 1998. doi: 10.1063/1.168744.

- [97] H. N. Yoshikawa, O. Crumeyrolle, and I. Mutabazi. Dielectrophoretic force-driven thermal convection in annular geometry. *Physics of Fluids*, 25(2):024106, 2013. doi: 10.1063/1.4792833. URL <https://doi.org/10.1063/1.4792833>.
- [98] H. N. Yoshikawa, M. Tadie Fogaing, O. Crumeyrolle, and I. Mutabazi. Dielectrophoretic Rayleigh-Bénard convection under microgravity conditions. *Physical Review E*, 87(4), Apr 2013. ISSN 1550-2376. doi: 10.1103/physreve.87.043003. URL <http://dx.doi.org/10.1103/PhysRevE.87.043003>.
- [99] H. N. Yoshikawa, C. Kwang, I. Mutabazi, **F. Zaussinger**, P. Haun, and C. Egbers. Dielectric heating induced thermal convection in a parallel plane capacitor. *Manuscript submitted for publication*, 2019.
- [100] H. N. Yoshikawa, C. Kang, I. Mutabazi, F. Zaussinger, P. Haun, and C. Egbers. Thermoelectrohydrodynamic convection in parallel plate capacitors under dielectric heating conditions. *Phys. Rev. Fluids*, 5:113503, Nov 2020. doi: 10.1103/PhysRevFluids.5.113503. URL <https://link.aps.org/doi/10.1103/PhysRevFluids.5.113503>.
- [101] M. Zahn. Derivation of the Korteweg-Helmholtz electric and magnetic force densities including electrostriction and magnetostriction from the quasistatic Poynting's theorems. In *2006 IEEE Conference on Electrical Insulation and Dielectric Phenomena*, pages 186–189, 2006. ISBN 0084-9162. doi: 10.1109/CEIDP.2006.312092.
- [102] F. Zaussinger. GeoFlow I and GeoFlow II: A Review. In *Book of abstracts, School ISTROF 2019, Instabilities and Turbulence in Strato-Rotational Flows, Cottbus*. BTU Cottbus-Senftenberg, 2019.
- [103] F. Zaussinger. AtmoFlow - Investigation of atmospheric-like fluid flows under micro-gravity conditions. In *Book of Abstracts - ELGRA 2019*, pages 55–56, 2019. URL [https://www.elgra2019.com/elgra2019bookofabstracts5/!](https://www.elgra2019.com/elgra2019bookofabstracts5/)
- [104] F. Zaussinger. Influence of internal heating on convection in the rotating spherical gap. In *Book of Abstracts - ETC 2019*, 2019. URL <http://www.symposium.it/files/eventi/84/etc-2019-561.pdf>.
- [105] F. Zaussinger and F. Kupka. Layer formation in double-diffusive convection over resting and moving heated plates. *Theoretical and Computational Fluid Dynamics*, 33(3):383–409, 2019. doi: 10.1007/s00162-019-00499-7. URL <https://doi.org/10.1007/s00162-019-00499-7>.
- [106] F. Zaussinger and H. C. Spruit. Semiconvection: numerical simulations. *Astronomy and Astrophysics*, 554:A119, 2013. doi: 10.1051/0004-6361/201220573. URL <http://dx.doi.org/10.1051/0004-6361/201220573>.
- [107] F. Zaussinger, A.-C. Plesa, C. Egbers, and D. Breuer. Mantle Convection in a Spherical Shell: Comparison of Numerical Simulations with the GeoFlow Experiment on the ISS. In A. Abbasi and N. Giesen, editors, *EGU General Assembly Conference Abstracts*, volume 14 of *EGU General Assembly Conference Abstracts*, page 9939, Apr. 2012.
- [108] F. Zaussinger, C. Egbers, A. Krebs, F. Schwarzbach, and C. Kunze. Time-dependent convective flows with high viscosity contrasts under micro gravity conditions. In *EGU General Assembly Conference Abstracts General Assembly Conference Abstracts*, volume 17 of *EGU General Assembly Conference Abstracts*, page 5833, Apr. 2015. URL <https://meetingorganizer.copernicus.org/EGU2015/EGU2015-5833.pdf>.
- [109] F. Zaussinger, C. Egbers, and A. Krebs. The GeoFlow experiments on the ISS: Thermal convection under microgravity conditions. In *Joint Conference ISPS-7 and ELGRA-25 October, 2-6 2017, Juan-les-Pins, France, Abstract book*, Joint Conference ISPS-7 and ELGRA-25 October, 2-6 2017, Juan-les-Pins, France, Abstract book, page S.

- 30, 2017. URL http://www.elgra.org/wp-content/uploads/2017/03/ISPS-7_ELGRA_25_2017_17A02-Abstract-book-final.pdf.
- [110] F. Zaussinger, C. Egbers, A. Krebs, and V. Travnikov. New results of the spherical convection experiment Geoflow IIc. In *EGU General Assembly Conference Abstracts*, volume 19 of *EGU General Assembly Conference Abstracts*, page 7801, Apr. 2017. URL <https://meetingorganizer.copernicus.org/EGU2017/EGU2017-7801.pdf>.
- [111] F. Zaussinger, A. Krebs, V. Travnikov, and C. Egbers. Recognition and tracking of convective flow patterns using Wollaston shearing interferometry. *Advances in Space Research*, 60(6):1327 – 1344, 2017. ISSN 0273-1177. doi: <https://doi.org/10.1016/j.asr.2017.06.028>. URL <http://www.sciencedirect.com/science/article/pii/S0273117717304544>.
- [112] F. Zaussinger, C. Egbers, P. Canfield, P. Haun, V. Travnikov, and A. Froitzheim. AtmoFlow - Experimental investigation of atmospheric flows under microgravity conditions. In *EGU General Assembly Conference Abstracts*, volume 20 of *EGU General Assembly Conference Abstracts*, page 6273, Feb. 2018. URL <https://meetingorganizer.copernicus.org/EGU2018/EGU2018-6273.pdf>.
- [113] F. Zaussinger, P. Haun, I. Mutabazi, and C. Egbers. Dielectrically driven convection in spherical gap geometry. In *Scientific programm EFMC12*, volume 1 of *Scientific programm EFMC*, page 46, September 2018. http://info.tuwien.ac.at/efmc12/EFMC12_program_v3.2.pdf.
- [114] F. Zaussinger, P. Haun, M. Neben, T. Seelig, V. Travnikov, C. Egbers, H. Yoshikawa, and I. Mutabazi. Dielectrically driven convection in spherical gap geometry. *Phys. Rev. Fluids*, 3:093501, Sep 2018. doi: 10.1103/PhysRevFluids.3.093501. URL <https://link.aps.org/doi/10.1103/PhysRevFluids.3.093501>.
- [115] F. Zaussinger, P. Canfield, A. Froitzheim, V. Travnikov, P. Haun, M. Meier, A. Meyer, P. Heintzmann, T. Driebe, and C. Egbers. AtmoFlow - Investigation of atmospheric-like fluid flows under microgravity conditions. *Microgravity Science and Technology*, Jul 2019. doi: 10.1007/s12217-019-09717-7. URL <https://doi.org/10.1007/s12217-019-09717-7>.
- [116] F. Zaussinger, C. Egbers, P. Canfield, P. Haun, V. Travnikov, A. Froitzheim, A. Meyer, and M. Meier. AtmoFlow - Investigation of atmospheric-like fluid flows under micro-gravity conditions. In *EGU General Assembly Conference Abstracts*, volume 21 of *EGU General Assembly Conference Abstracts*, page 8441, 2019. URL <https://meetingorganizer.copernicus.org/EGU2019/EGU2019-8441.pdf>.
- [117] F. Zaussinger, P. Haun, P. Szabo, V. Travnikov, M. Al Kawwas, and C. Egbers. Rotating spherical gap convection in the GeoFlow International Space Station (ISS) experiment. *Phys. Rev. Fluids*, 5: 063502, Jun 2020. doi: 10.1103/PhysRevFluids.5.063502. URL <https://link.aps.org/doi/10.1103/PhysRevFluids.5.063502>.
- [118] K. Zhang. Spiralling columnar convection in rapidly rotating spherical fluid shells. *Journal of Fluid Mechanics*, 236:535–556, 1992. doi: 10.1017/S0022112092001526.

9 Publications as full-text

Open Access pathways permitted by the journal's policy are listed below. The publisher policies are checked by SherpaRomeo and at the publishers' homepages at 25. March 2021.

- Publisher: Springer, Journal: Microgravity Science and Technology, type: published version, pathway: Institutional Repository, embargo: none
- Publisher: Elsevier, Journal: Advances in Space Research, type: published version, pathway: Institutional Repository, embargo: none
- Publisher: APS, Journal: Physical Review E, type: published version, pathway: Institutional Repository, embargo: none
- Publisher: APS, Journal: Physical Review Fluids, type: published version, pathway: Institutional Repository, embargo: none

